



저작자표시-비영리-변경금지 2.0 대한민국

이용자는 아래의 조건을 따르는 경우에 한하여 자유롭게

- 이 저작물을 복제, 배포, 전송, 전시, 공연 및 방송할 수 있습니다.

다음과 같은 조건을 따라야 합니다:



저작자표시. 귀하는 원저작자를 표시하여야 합니다.



비영리. 귀하는 이 저작물을 영리 목적으로 이용할 수 없습니다.



변경금지. 귀하는 이 저작물을 개작, 변형 또는 가공할 수 없습니다.

- 귀하는, 이 저작물의 재이용이나 배포의 경우, 이 저작물에 적용된 이용허락조건을 명확하게 나타내어야 합니다.
- 저작권자로부터 별도의 허가를 받으면 이러한 조건들은 적용되지 않습니다.

저작권법에 따른 이용자의 권리는 위의 내용에 의하여 영향을 받지 않습니다.

이것은 [이용허락규약\(Legal Code\)](#)을 이해하기 쉽게 요약한 것입니다.

[Disclaimer](#)

공학박사학위논문

공진기 쌍을 이용한 극저 임피던스  
유효 매질 구현 및 탄성과 출력  
향상

Super Enhancement of Elastic Wave Emission Using  
Extremely Low Effective Impedance Medium  
Realized by Paired Resonators

2018 년 8 월

서울대학교 대학원

기계항공공학부

김 기 연

## **ABSTRACT**

# **Super Enhancement of Elastic Wave Emission Using Extremely Low Effective Impedance Medium Realized by Paired Resonators**

**Kim, Kiyeon**

**School of Mechanical Engineering**

**The Graduate School**

**Seoul National University**

This work is mainly dedicated about the development of passive and non-destructive super enhancement of elastic wave emission, and revealing the reason of enhancement by setting up a new effective medium theory. Ultrasonic transducers have been designed and improved to enhance its wave emission performance, but yet manipulation on the medium where the transducers are attached has not been considered. However, conventional non-destructive manipulation on the medium leads to higher impedance, which is not desirable for the super enhancement.

Inversely, digging out the material lowers the mechanical impedance but it is also not desirable in practice. Therefore, a method to lower the impedance without damaging the medium should be introduced.

In order to achieve the goal, we use a pair of resonators to be attached on the base medium. Since just the pair of resonators is not in a periodic arrangement, it requires a new tool to analyze the effective properties of the system. With this unique arrangement of resonators, the corresponding effective medium theory is newly established. Furthermore, since size of the paired resonator system is not in a subwavelength range, the existing methods for characterizing the effective medium cannot be applied directly.

With the newly derived analysis, the equivalent effective medium is found and the effective impedance of the medium surrounded by the resonators is found to be extremely lowered than that of nominal medium. As a usage of the lowered impedance, ultrasonic transducers are attached on the region where the impedance is lowered to enhance their wave emissions. However, the high contrast of impedance does not assure the high transmission of wave generated by the transducers. This work reveals the condition which the wave can be highly generated and fully

transmitted through the outer medium. As examples of the theory, super enhancements of three modes in plate, S0, SH0 and A0, are shown.

To investigate the extreme low impedance and the super enhancement, we show a detailed theoretical analysis, Numerical simulations using finite element method and experimental results.

**Keywords:** Elastic metamaterials, Low impedance, Emission enhancement, Transducer, Effective medium model

***Student Number:*** 2012-20647

# CONTENTS

ABSTRACT.....	i
CONTENTS.....	iv
LIST OF FIGURES.....	vii
LIST OF TABLES.....	xix
CHAPTER 1. INTRODUCTION.....	1
1.1 Research motivation.....	1
1.2 Research Objectives.....	4
1.3 Outline of Thesis.....	7
CHAPTER 2. THEORETICAL BACKGROUND.....	11
2.1 Fundamentals of waves in a plate.....	11
2.1.1 Lamb wave.....	12
2.1.2 Timoshenko beam theory.....	13
2.1.3 Shear-horizontal wave.....	15
2.2 Ultrasonic transducers.....	16
2.2.1 Principle of piezoceramic transducer.....	16
2.2.2 Principle of magnetostrictive patch transducer.....	17
2.2.3 Pin-force modeling of ultrasonic transducers.....	20
2.3 Effective medium theory.....	21
CHAPTER 3. PROPOSITION OF EQUIVALENT SYSTEM THEORY OF RESONATOR PAIRING.....	31
3.1 Resonator-paired waveguide system.....	32
3.2 Equivalent medium of the paired resonator system.....	35
3.3 Effective properties of the equivalent system.....	45

3.4	Frequency selection process.....	50
3.5	Summary .....	50
CHAPTER 4. DESIGN OF THE RESONATOR PAIRING FOR LAMB WAVE AND SHEAR-HORIZONTAL WAVE EMISSION ENHANCEMENT .....		56
4.1	Realization of the resonator pair for S0 Lamb wave.....	57
4.2	Realization of the resonator pair for SH0 wave .....	61
4.3	Realization of resonators for axisymmetric S0 Lamb wave and SH0 wave 64	
4.4	Summary .....	65
CHAPTER 5. RESONATOR PAIRING FOR ENHANCED SENSING.....		75
5.1	Resonator-paired waveguide system in receiving mode .....	75
5.2	Realization and experimental results for S0 and SH0 wave .....	78
5.3	Equivalent system of the paired resonator system in receiving mode ..	80
5.4	Summary .....	83
CHAPTER 6. ANALYSIS OF EMISSION IN BENDING WAVE SYSTEM .....		85
6.1	Analytic model.....	88
6.2	Experiments .....	99
6.3	Realization of a resonator for axisymmetric A0 Lamb wave.....	102
6.4	Summary .....	102
CHAPTER 7. CONCLUSIONS .....		114
Appendix A. Output enhancing of omnidirectional Lamb wave-MPT by slits in a patch 117		
A.1	Introduction.....	117
A.2	Patch slitting effect on eddy current circuit .....	122
A.3	Effects of the numbers of slits on the transducer performance .....	131
A.4	Detailed eddy current circuit and strain states .....	136

A.5 Summary .....	137
REFERENCES.....	153
ABSTRACT (KOREAN).....	165

# LIST OF FIGURES

Figure 1.1 Thin plates of uniform (top) and non-uniform (bottom) thicknesses carrying plane longitudinal waves. PZT patch transducers are installed to generate the S0 Lamb waves in the plates simulating the longitudinal waves in a beam. ....9

Figure 1.2 The amplification effects of the non-uniformity ( $\hat{t}$  : reduced thickness of the transducer installed zone and  $t_0$  : nominal thickness) on the magnitude of the generated displacement field. ....9

Figure 2.1 Superposition of P-wave and SV-wave in a plate, yielding Lamb waves. ....24

Figure 2.2 Dispersion curve of aluminum plate (thickness of 2 mm) calculated with DISPERSE [39]. ....24

Figure 2.3 Mode shapes of (a) S0 wave and (b) A0 wave in a 2 mm aluminum plate at frequency of 200 kHz calculated by DISPERSE[39]. The particle motion of S0 wave is dominantly in longitudinal direction, and the particle motion of A0 wave is in both out-of-plane and rotating direction. ....25

Figure 2.4 Kinematics of Timoshenko beam in an infinitesimal element.  $\varphi$  is the rotation angle and  $v$  is the displacement of the beam. ....26

Figure 2.5 Infinitesimal element of Timoshenko beam (length of $dx$ and cross-sectional area of $A$ ) showing force equilibrium. $V$ denotes shear force and $M$ denotes moment. ....	26
Figure 2.6 Mechanical longitudinal deformation of piezoelectric elements under external electric field. ....	27
Figure 2.7 Mechanical longitudinal deformation of magnetostrictive elements under static magnetic field. ....	27
Figure 2.8 Dynamic longitudinal deformation of magnetostrictive elements under static magnetic field with parallel dynamic magnetic field. ....	28
Figure 2.9 Dynamic shear deformation of magnetostrictive elements under static magnetic field with perpendicular dynamic magnetic field. ....	28
Figure 2.10 Configuration of magnetostrictive patch transducer (MPT) for shear-horizontal wave transduction. MPT is consisted of magnetostrictive patch, permanent magnets and coil. ....	29
Figure 2.11 Concentrated force modeling of wave generation principle of transducers. (a) Forces in parallel direction with propagating direction of S0 wave and (b) Forces in perpendicular direction with propagating direction of SH0 wave. ....	30
Figure 2.12 Transmitted ( $C$ ), reflected ( $B$ ) wave for incident wave ( $A$ ) from medium	

1 embedded with medium 2. Medium 1 has impedance of  $z_1$  and wavenumber of  $k_1$  and medium 2 has impedance of  $z_2$  and wavenumber of  $k_2$ . .....30

Figure 3.1 Analysis of bar model in which the displacements in various locations are specified. The generation mechanism of transducer is simplified as two concentrated forces at  $x = \pm L$  .....52

Figure 3.2 The magnitude of radiated strain field in a beam with and without the resonators. The mass and stiffness of the resonators are  $m = 58.9$  g and  $s = 38.5$  GN/m.....52

Figure 3.3 One-dimensional bar models describing the longitudinal motion in a plate. The model in the top illustration depicts a bar equipped with two point-resonators while the model in the bottom illustration is an equivalent bar model with a modified effective impedance to account for the effects of resonators on wave motion.....53

Figure 3.4 Effective impedance  $z$ , density  $\rho$  and stiffness  $E$  in a beam with and without the resonators. The mass and stiffness of the resonators are  $m = 58.9$  g and  $s = 38.5$  GN/m. ....53

Figure 3.5 Transmission coefficient in the bar configuration shown in the inset of illustration. ....54

Figure 3.6 The effects of the resonance frequency  $f_R$  on the magnitude of radiated strain  $|S|$ . .....54

Figure 3.7 The effects of the distance  $W$  between the two resonators on the magnitude of radiated strain  $|S|$ . .....55

Figure 3.8 Plot of frequency characteristics of (a) a transducer without resonators (b) and the transducer with resonators tuned to Fabry-Perot frequency to  $f_T$ . .....55

Figure 4.1 Sketch of thin plate with two resonators installed at  $x = \pm W$ . Each resonator at  $x = W$  or  $x = -W$  consists of two symmetrically configured C-shaped beams to ensure the generation of pure thickness-symmetric longitudinal waves without generating thickness-antisymmetric bending waves. ....66

Figure 4.2 (a) Frontal view of lowest eigenmode of C-Shaped resonator and (b) deformed shape of pillars of C-shaped resonator under applied force  $f_x$  along  $x$  axis. ....67

Figure 4.3 Setup for longitudinal wave experiments in thin plate. Three PZT patches were used to ensure the generation of a plane longitudinal wave mode in the plate. ....67

Figure 4.4 A comparison of the experimental and theoretical/numerical results for the radiated longitudinal strain field $ \mathcal{S} $ .	68
Figure 4.5 Illustration of simulations of S0 wave transduction using T-shaped resonator.	68
Figure 4.6 Dimension and eigenmode analysis of T-shaped resonator for S0 wave.	69
Figure 4.7 A comparison of the theoretical and numerical results for the radiated shear strain field $ \mathcal{S} $ , using T-shaped resonators for S0 wave.	69
Figure 4.8 Sketch of thin plate with two C-shaped resonators installed at $x = \pm W$ for SH0 wave transduction.	70
Figure 4.9 (a) Trimetric view of lowest eigenmode of C-Shaped resonator and (b) deformed shape of a pillar of C-shaped resonator under applied force $f_z$ along $z$ axis.	70
Figure 4.10 Sketch of thin plate with two T-shaped resonators installed at $x = \pm W$ for SH0 wave transduction.	71
Figure 4.11 (a) Trimetric view of lowest eigenmode of T-Shaped resonator and (b) deformed shape of a pillar of T-shaped resonator under applied force $f_z$ along $z$ axis.	71

Figure 4.12 Setup for SH0 wave experiments in thin plate. A MPT was used to generate of a plane SH0 wave mode in the plate.....72

Figure 4.13 A comparison of the experimental and theoretical/numerical results for the radiated shear strain field  $|S|$ .....72

Figure 4.14 Illustrations of applications of resonators for (a) axisymmetric S0 wave and (b) axisymmetric SH0 wave. ....73

Figure 4.15 Illustrations of numerical simulations of wave transduction with resonators of (a) axisymmetric S0 wave and (b) axisymmetric SH0 wave. ....73

Figure 4.16 Plots of emitted (a) axisymmetric S0 wave and (b) axisymmetric SH0 wave with and without resonators. ....74

Figure 5.1 Schematic of wave status in receiving mode. Sensor measurement in (a) nominal case and (b) resonator case with an incident wave  $I$ . (c) Equivalent system using effective medium of sensing in resonator case as shown in (b). ....84

Figure 5.2 A comparison of the experimental and theoretical/numerical results for the measured (a) longitudinal strain of S0 wave and (b) shear strain of SH0 wave. ....84

Figure 6.1 The nominal MPT with  $w_{\text{MPT}} = 10 \text{ mm}$ ,  $b_{\text{MPT}} = 100 \text{ mm}$ ,  $t_{\text{MPT}} = 0.15$

mm.....	105
Figure 6.2 Actuation mechanism of the nominal MPT. The considered actuation wave mode in the plate is the A0 Lamb wave mode. ....	105
Figure 6.3 (a) The proposed MPT with an add-on type U-shaped resonator, a nickel patch was used as the magnetostrictive patch and (b) actuation mechanism of the proposed MPT.....	106
Figure 6.4 (a) A simplified transduction model of a magnetostrictive patch transducer. (b) The frequency characteristics of transducer efficiency of both detailed transduction model and the simplified transduction models. ....	106
Figure 6.5 (a) A drawing of the proposed U-shaped resonator, (b) resonator on a plate with simplified transduction model.....	107
Figure 6.6 (c) Generalized spring-mass modeling of the U-shaped transducer on a beam and (d) relations between the generalized spring of a resonator, forces and displacements.....	107
Figure 6.7 (a) The cross-section of the U-shaped resonator case 1 and (b) the first 3 eigenmodes of the U-shaped resonator case 1. (c) A description of the motion of the inertia part in the resonator. ....	108
Figure 6.8 A description of force and moment interactions between a U-shaped resonator and a Timoshenko beam, and overall wave solutions in the	

beam. ....	108
Figure 6.9 A detailed description of the kinematics between the U-shaped resonator and the underlying beam. ....	109
Figure 6.10 Transducer outputs ( $ \varepsilon_x $ on the plate surface of section B) (a) without resonators, (b) with resonator case 1, (c) with resonator case 2, and (d) with resonator case 3 solved by Timoshenko beam analysis and FEM analysis. ....	109
Figure 6.11 Experimental setup to measure the elastic waves generated from the transmitters with and without resonators. ....	110
Figure 6.12 The frequency characteristics of the transducers and time signals in peak frequencies with resonator case 1 from the experiments and simulation results. ....	110
Figure 6.13 The frequency characteristics of the transducers and time signals in peak frequencies with resonator case 2 from the experiments and simulation results. ....	111
Figure 6.14 The frequency characteristics of the transducers and time signals in peak frequencies with resonator case 3 from the experiments and simulation results. ....	111
Figure 6.15 Illustration of application of resonators for axisymmetric A0 wave. .	112

Figure 6.16 Illustration of numerical simulations of wave transduction with resonator for axisymmetric A0 wave. .... 112

Figure 6.17 Plots of emitted axisymmetric A0 wave with and without resonators. .... 113

Figure A 1 (a) A configuration, (b) top view and side view of the OLMPT (omnidirectional magnetostrictive patch transducer) considered in this study.....141

Figure A 2 (a) Field direction ( $\mathbf{H}_i$ : magnetic field,  $\mathbf{J}_i$ : induced current), (b) induced current density and (c) magnetic field distributions of an OL-MPT with a slit-less nickel patch installed on an aluminum plate. The induced circumferential current and radial magnetic field are measured along the  $z$ -direction on the mid-point of the coil (i.e., at  $r = (r_o + r_i)/2$ )..... 141

Figure A 3 Schematic description of the finite element model of the MPT, an aluminum plate and surrounding air for wave transduction simulation. .... 142

Figure A 4 (a) Field direction ( $\mathbf{H}_i$ : magnetic field,  $\mathbf{J}_i$ : induced current), (b) induced current density and (c) magnetic field distributions of a Lamb wave MPT with a slit nickel patch installed on an aluminum plate. The induced circumferential current and radial magnetic field are measured along the  $z$ -direction on the mid-point of the coil (i.e., at  $r = (r_o + r_i)/2$ )..... 142

Figure A 5 Radial magnetic flux density plot in (a) a circular slit-less nickel patch and (b) a single-slit patch on their top and bottom surfaces..... 143

Figure A 6 (a) Field direction ( $\mathbf{H}_i$ : magnetic field,  $\mathbf{J}_i$ : induced current), (b) induced current density and (c) magnetic field distributions of a Lamb wave MPT with a slit nickel patch installed on a glass plate. The induced circumferential current and radial magnetic field are measured along the  $z$ -direction on the mid-point of the coil (i.e., at  $r = (r_o + r_i)/2$ )..... 143

Figure A 7 (a) Induced current density and (b) magnetic field distributions of MPTs with slit-less and single-slit patches installed on aluminum and glass plates. .... 144

Figure A 8 Contour plots of the radial displacement (for a selected time) in the mid plane of the plates. The plots are obtained for MPT transmitters with (a) a slit-less patch, (b) and a single-slit patch on an aluminum plate and (c) single-slit patch on a glass plate. .... 144

Figure A 9 Radiation patterns of the S0 modes in plates for MPTs equipped with different patch configurations installed on aluminum and glass plates. .... 145

Figure A 10 Photos of the various patches considered for the experiments. .... 145

Figure A 11 Experimental setup to measure the elastic waves radiated on the aluminum and glass plates..... 146

Figure A 12 (a) Input Gabor pulse signal centered at 270 kHz, (b) measured signals on an aluminum plate, and (c) measured signals on a glass plate. .... 147

Figure A 13 Radial magnetic flux density plots of multiply slit patches..... 148

Figure A 14 The radial magnetic fields ( $H_r$ ) integrated along the  $z$ -direction on the mid-point of the coil (i.e., at  $r = (r_o + r_i)/2$ ) inside the magnetostrictive patch along the circumferential angle. The fields are normalized with respect to the field in the slit-less patch. .... 148

Figure A 15 Radiation patterns of the S0 mode and experimentally measured signals by the receivers (R1–R7). The results are for (a) 4-slit, (b) 8-slit and (c) 12-slit patches installed on an aluminum plate. .... 149

Figure A 16 Radiation patterns of the S0 mode and signals that were experimentally measured by the receivers (R1–R7). The results are for (a) 4-slit, (b) 8-slit and (c) 12-slit patches installed on a glass plate..... 150

Figure A 17 Ratio of the minimum to maximum peak-to-peak values obtained from the radiation pattern signals (a) for on an aluminum plate and (b) for on a glass plate. .... 151

Figure A 18 Signal output increase ratio for a varying number of slits in the circular magnetostrictive patch of OL-MPT. ( $V_{R1}^n$  : peak-to-peak values of the signal measured by R1 for the n-slit patch-equipped MPT transmitter,

$V_{R1}^0$  : peak-to-peak value of the signal measured by R1 for the slit-less patch-equipped MPT transmitter.)..... 151

Figure A 19 Contour plots of the radial component ( $J_{2r}$ ) of the current density on the bottom surface of (a) 1-slit patch and (b) 4-slit patch. The red line indicates the actual current circuit developed on the bottom surface.. 152

Figure A20 (a) Circumferential component of the magnetic field plot of the bottom surface of 4-slit patch ( $H_{2\theta}$ ), and (b) the shear strain due to the circumferential component of magnetic field ( $H_{2\theta}$ ). The equivalent normal stress state with respect to 45°-rotated directions is also shown. .... 152

## LIST OF TABLES

<b>Table 6.1</b> Material properties of an aluminum plate and a resonator.....	104
<b>Table 6.2</b> Stiffness matrix, mass coefficients and eigenfrequencies of the U-shaped resonators. ....	104
<b>Table A 1</b> Material properties of a nickel patch and test plates. ....	140

# CHAPTER 1.

## INTRODUCTION

### 1.1 Research motivation

Impedance is one of the key parameters in wave propagation, transmission and reflection in a media. As counterparts of permeability  $\mu$  and permittivity  $\epsilon$  in electromagnetics, density  $\rho$  and modulus  $E$  have been manipulated for extreme wave phenomena using metamaterials [1-6], since they govern the phase velocity ( $\sqrt{E/\rho}$ ) and impedance ( $\sqrt{\rho E}$ ) of the media carrying the elastic waves. For example, effective impedance can be tuned to perfectly match with outer media, and the phase velocity can be adjusted to realize wave tunneling and other phenomena [7-16]. While zero index metamaterials, where  $\rho/E$  is almost zero, this thesis is more concerned with another extraordinary case called zero impedance, where  $\rho E$  becomes zero.

Because of the definition of the characteristic impedance, the amount of force to drive the unit velocity of a particle, weaker impedance of a test specimen allows to generate a higher output with the same force input. Therefore, it is easily expected that the wave emission will be extremely enhanced on the zero impedance medium if the same transducer is used. With an insight of this extremely low impedance can be extremely useful with wave emission enhancing, the extremely low impedance concept is needed to be combined with conventional ultrasonic transducers. For decades, ultrasonic transducers have been widely studied to improve their performances [17-24]. However, no attempts have been tried to manipulate properties of the media on which the transducers are installed, nevertheless the strong impact of the mechanical properties of the base media on the wave emissions.

Reducing the impedance of a waveguide can be easily achieved by machining the waveguide, as shown in Fig. 1.1. The figure shows two thin plates, which are waveguides carrying plane longitudinal waves propagating in  $x$  direction. The radiated field outside of point P is plotted in Fig. 1.2 when the plates are excited by a longitudinal wave source, such as PZT patch transducers. The frequency was assumed to be one of the Fabry–Pérot resonance frequencies so that the wave excited by the transducers can be fully transmitted. Fig. 1.2 shows that the radiated wave

field can grow as highly as possible when the thickness of the plate approaches zero, where  $t_0$  and  $\hat{t}$  respectively represent the thickness of the nominal and machined parts of the plate. As mechanical impedance depends proportionally on the cross-sectional area, the reduced plate thickness corresponds to the lowered mechanical impedance.

However, as an application of lowered impedance, super enhancing of wave emission will be potentially used on waveguides such as the (curved) plates of an oil tank and pipelines in a nuclear power facility, in which a transducer is installed for health monitoring [19, 25-27]. These applications demand that the hosting medium should stay healthy, i.e., the structure should not be damaged or machined as shown in Fig. 1.1. For this reason, a nondestructive method to reduce the mechanical impedance should be investigated. In order not to damage the structure, some components should be attached onto the medium, which will intuitively increase the mechanical impedance.

As already shown in Fig. 1.1 and Fig. 1.2, the zero impedance system is involved with Fabry–Pérot resonance, which does not satisfy the sub-wavelength limit. Furthermore, the system is not in periodic arrangement, the system cannot be analyzed with conventional effective medium analyses [6, 28-32]. Therefore, a new

analysis to interpret the original system into an equivalent system should be introduced.

Motivated by the issues, this thesis is dedicated to develop a method to lower the effective impedance of a medium without damaging the hosting structure. Also, the method to analyze the effective impedance is introduced in this thesis.

## **1.2 Research Objectives**

The main objectives of the research are in two steps. One is to develop a method to lower the impedance of a waveguide nondestructively and derive an equivalent system of effective impedance. The other main objective is to show the super enhancements of transducers using the lowered impedance, and show that it is the consequence of the near-zero impedance in the wave actuated zone. As a means to verify the realization of extremely low effective impedance, we made the effective impedance of the wave-excited region of a waveguide nearly zero, or more practically lower than its nominal impedance, and showed that the emitted wave became super enhanced. The detailed objectives are listed below.

Objective 1: Proposition of equivalent system theory of resonator pairing

This thesis shows that a pair of resonators installed on a plate can reduce the effective impedance of the region surrounded by the resonators. The conventional effective medium theory assumes that unit cells are in periodic arrangement and the size of the cell is much smaller than the wavelength. Keeping in mind that the pair of resonators is proposed to be surround the region where the transducers are to be installed, the system is not in subwavelength regime. At the actuation frequency of a transducer, the size of the transducer is larger than half-wavelength [17, 22, 33]. Moreover, because that two resonators are not arranged periodically, conventional effective analysis cannot be applied to retrieve its effective properties. Therefore, developing a new analysis to characterize the effective impedance using equivalent system is one of the objectives of the thesis.

Objective 2: Designs of the resonator pairing for Lamb wave and shear-horizontal wave emission enhancement

As one of the applications and the evidence of the lowered impedance, enhanced wave emission from ultrasonic transducers between the resonators will be shown. More specifically, the Lamb wave and shear-horizontal wave in a plate generated by piezoceramic transducer (PZT) and magnetostrictive patch transducer (MPT), respectively, are enhanced. Moreover, the resonators are designed and realized for its corresponding wave motions to function as point resonators.

### Objective 3: Resonator pairing for super enhanced sensing

The lowered impedance can be also useful for the transducer in receiving mode, due to the reciprocal principle. The wave field inside the low impedance medium is amplified, therefore the sensor measures the amplified signal. When the same resonators are used, that the equivalent system has the same reduced impedance will be proved.

### Objective 4: Analysis of emission enhancement in bending wave system

Bending wave in a plate is represented by Timoshenko beam theory [34]. Particle motion in the bending wave is predominantly in the vertical direction, so a new resonator accompanying the vertical direction should be designed. Combined with Timoshenko beam theory, that the wave output from an MPT can be increased with the designed resonator will be shown in the thesis. The detailed kinematics and dynamics will be derived.

### **1.3 Outline of Thesis**

In Chapter 2, the theoretical backgrounds in conventional effective medium analysis and fundamentals of ultrasonic transducers will be presented. Also, the general overview in Lamb, shear-horizontal, and Timoshenko beam waves will be given. The actuation and sensing mechanism of ultrasonic transducers, including piezoceramic (PZT) and magnetostrictive patch transducer (MPT) will be reviewed. The retrieval method and characterization of effective medium will be reviewed.

In Chapter 3, equivalent system theory of waveguide with a pair of resonators will be proposed. In this chapter, wave emission with the wave sources surrounded by the resonators will be analyzed. Then the system using effective impedance which is equivalent to the original paired resonator system will be introduced. Consequently, that the effective impedance can be lowered even to nearly zero using the pair of resonators will be shown. The theoretical reason of the enhancement will be explained in this chapter.

In Chapter 4, as the application for the lowered impedance, the wave emission enhancement will be introduced. The designs of the resonator pairing for Lamb wave and shear-horizontal wave emission enhancement will be introduced. For Lamb

wave, a set of PZTs is used and a set of MPTs is used for shear-horizontal wave. The numerical and experimental results will be shown.

In Chapter 5, the same resonators used for enhanced sensing will be introduced. For the same incident wave, the paired resonators make the effective impedance extremely lowered. The theoretical analysis of the wave status and equivalent system will be studied. For Lamb wave and shear-horizontal wave case, the experimental results for super sensing will be shown.

In Chapter 6, emission enhancement for bending wave will be analyzed. Since bending wave in a plate is analyzed with Timoshenko beam theory, the emission enhancement should be analyzed differently. A resonator is designed to be moved vertically to correspond with the particle motion of the bending wave. The motion of the resonator is combined with Timoshenko beam theory, yielding an analysis of wave emission enhancement of bending wave.

In Chapter 7, the overall concluding remarks for the thesis will be presented.

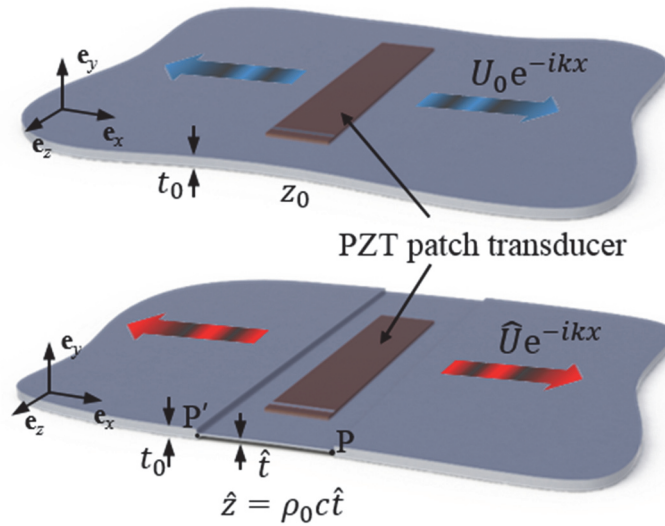


Figure 1.1 Thin plates of uniform (top) and non-uniform (bottom) thicknesses carrying plane longitudinal waves. PZT patch transducers are installed to generate the S0 Lamb waves in the plates simulating the longitudinal waves in a beam.

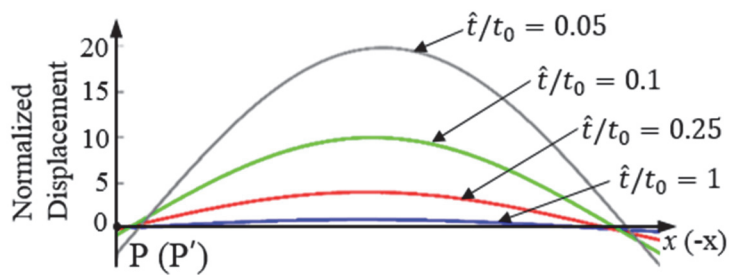


Figure 1.2 The amplification effects of the non-uniformity ( $\hat{t}$  : reduced thickness of

the transducer installed zone and  $t_0$  : nominal thickness) on the magnitude of the generated displacement field.

# **CHAPTER 2.**

## **THEORETICAL BACKGROUND**

In this chapter, the theoretical backgrounds of this thesis, the waves in isotropic plate generated by transducers and the effective parameter analysis is overviewed. Since the thesis mainly based on the elastic waves, the general wave description of Lamb, shear-horizontal and Timoshenko beam wave is needed to be given in section 2.1. Then, the wave fundamentals and actuation mechanisms of ultrasonic transducers is reviewed in section 2.2. Finally, the effective medium theory is given in section 2.3.

### **2.1 Fundamentals of waves in a plate**

In a plate, there exist 3 kinds of guided waves: Symmetric Lamb wave, antisymmetric Lamb wave and shear-horizontal wave. Fundamentally, the guided waves are consequences of longitudinal wave (P wave) and shear wave (SV-wave)

and SH-wave) guided by the top and bottom surfaces of the plate as plotted in Fig 2.1. Thus the guided waves experience different phenomena than those of the waves in an infinite medium, called dispersion [35, 36]. This phenomena is further studied by Achenbach [37] and Graff [38].

### **2.1.1 Lamb wave**

Consider an infinitely long plate in  $x$  and  $z$  direction, having thickness  $t$  in  $y$  direction as shown in Fig. 2.1. On  $x$ - $y$  plane of the plate, when P-wave is incident on one of the surface, both P-wave and SV-wave is reflected out from the surface. Also, same phenomena appear when SV-wave is incident. Therefore, both P-wave and SV-wave should be coupled to form a standing wave inside the plate. As a consequence, symmetric Lamb wave (S-mode) or antisymmetric Lamb wave (A-mode) is formed. The dispersion curves of some of the modes obtained by DISPERSE [39] are depicted in Fig. 2.2.

The lowest modes of each wave, S0 and A0 modes have the simplest mode shapes. The mode shape of S0 wave is predominantly uniform in  $x$ -direction as shown in Fig. 2.3. For the low frequency range, where the non-dispersive wave can be assumed, S0 mode can be assumed as a longitudinal wave in a beam. On the other hand, the mode shape of A0 wave is more complex than that of S0 wave. The particle motion

is mostly in  $y$ -direction, however some component of the motion is in  $x$ -direction as a rotation component. Therefore, it may not be assumed as a simple SV-wave and it is one of the bending waves in a plate. Instead, A0 mode can be analyzed using Timoshenko beam theory.

### 2.1.2 Timoshenko beam theory

To model bending wave or flexural wave in a beam or plate, Euler-Bernoulli beam theory [40] had been studied. However, Euler-Bernoulli beam theory was found to be good match only at low frequency, and discrepancies occurred at high frequency range. This is because of lack of the degree of freedom, the rotary motion of the beam could not be explained well. To overcome the limit of Euler-Bernoulli beam theory, Timoshenko beam theory have been studied.

Considering a beam illustrated in Fig. 2.4, the kinematics of the beam is expressed as:

$$u_x(x, y, t) = -y\psi(x, t), \quad (2.1a)$$

$$\varepsilon_{xx} = -y \frac{\partial \psi}{\partial x} = -yK, \text{ where } K \equiv \frac{\partial \psi}{\partial x}. \quad (2.1b)$$

$u$  is the particle displacement in  $x$ -direction, and  $\psi$  is the angle of rotation of the beam. As we define  $\gamma = \partial v / \partial x - \psi$ , where  $v$  is the vertical displacement of the mid plane of the beam,  $\gamma$  implies the shear deformation in the beam.

Considering the dynamics of infinitesimal element as shown in Fig. 2.5, the equations of motion are expressed as below:

$$\frac{\partial V}{\partial x} = \rho A \frac{\partial^2 v}{\partial t^2}, \quad (2.2a)$$

$$\frac{\partial M}{\partial x} + V = \rho I \frac{\partial^2 \psi}{\partial t^2}, \quad (2.2b)$$

where  $V$  is shear force,  $A$  is cross-sectional area,  $M$  is moment and  $I$  is moment of inertia. The moment  $M$  and shear force  $V$  can be expressed as below with the constitutive relation.

$$M = EIK, \quad (2.3a)$$

$$V = GA\gamma, \quad (2.3b)$$

where  $E$  is Young's modulus and  $G$  is shear modulus.

Combining all equations, following relations are derived:

$$GA \left( \frac{\partial^2 V}{\partial x^2} - \frac{\partial \psi}{\partial x} \right) = \rho A \frac{\partial^2 v}{\partial t^2}, \quad (2.4a)$$

$$EI \frac{\partial^2 \psi}{\partial x^2} + GA \left( \frac{\partial v}{\partial x} - \psi \right) = \rho I \frac{\partial^2 \psi}{\partial t^2}. \quad (2.4b)$$

We assume that the variables are in harmonic state, i.e.,  $v = \bar{v}e^{-i(kx-\omega t)}$  and  $\psi = \bar{\psi}e^{-i(kx-\omega t)}$ , where  $k$  is wavenumber and  $\omega$  is angular frequency. Then the relations between the wavenumber and frequency can be derived as:

$$k_1 = \left[ \frac{1}{2} \left( \frac{\rho}{G} + \frac{\rho}{E} \right) \omega^2 + \sqrt{\frac{\rho A}{EI} \omega^2 + \frac{1}{4} \left( \frac{\rho}{G} - \frac{\rho}{E} \right)^2 \omega^4} \right]^{1/2}, \quad (2.4a)$$

$$k_2 = \left[ \frac{1}{2} \left( \frac{\rho}{G} + \frac{\rho}{E} \right) \omega^2 - \sqrt{\frac{\rho A}{EI} \omega^2 + \frac{1}{4} \left( \frac{\rho}{G} - \frac{\rho}{E} \right)^2 \omega^4} \right]^{1/2}. \quad (2.4b)$$

### 2.1.3 Shear-horizontal wave

When SH wave is incident to a surface of a plate, only SH wave is reflected and not coupled with other waves. Therefore, the guided wave is formed with their particle motion in purely  $z$ -direction in a plate. However, by the reflections between the both surfaces of the plate, a standing wave is formed in  $y$ -direction. Regarding to the mode shape of the standing wave in  $y$ -direction, the order of shear-horizontal wave is

described. However, the lowest mode of shear-horizontal wave, SH0 mode has a uniform mode shape, meaning that the incident SH wave is originally in  $x$ -direction. Therefore, the dispersion characteristics of SH0 mode is the same with SH wave in an infinite media.

## **2.2 Ultrasonic transducers**

To generate the guided waves described in previous sections, many ultrasonic transducers have been developed [17-21]. They include piezoceramic transducers (PZT) and magnetostrictive patch transducers (MPT), which are mainly used in this thesis.

### **2.2.1 Principle of piezoceramic transducer**

PZT is a transducer that uses piezoelectric phenomenon in a dielectric material. Piezoelectricity is first discovered by Curie [41]. Piezoelectricity is coupling effect between electricity and mechanical deformation that the material is electrically charged when the material is objected to a mechanical load. As reciprocal effect, inverse piezoelectricity is a phenomenon that the material is elongated or contracted when electric field is applied through the material.

When an electric field is applied through the material, the electric field affects the dipoles in the medium yielding a shape change (Fig. 2.6). Therefore, the electric field makes mechanical deformation in the material. This phenomenon is effective in generating normal strain in a mechanical body.

Using this phenomenon, many piezoelectric transducers are developed [42, 43]. Using a thin piezoceramic patch, it is efficient to generate guided waves in a plate [43, 44]. The electric signal is applied on both electrodes of the patch and the patch is deformed to generate the guided waves in the underlying waveguide.

### **2.2.2 Principle of magnetostrictive patch transducer**

MPT is a transducer that uses magnetic phenomenon of a ferromagnetic material called magnetostriction, first discovered by Joule [45]. Magnetostriction is a coupling effect between magnetic field and mechanical deformation in a ferromagnetic material. The material is elongated under an external magnetic field. On the other hand, there have been observed that the reciprocal phenomenon, which the magnetic flux is changed in the material under a tensile or compressive elastic load, called Villari effect [45]. Especially, if a static magnetic field is given and the external dynamic magnetic field is applied perpendicularly with the static magnetic

field, the material experiences a shear deformation. This effect is called Widemann effect [46] and the reciprocal effect is called Matteucci effect [45, 46].

Magnetostrictive material is composed of numerous small grains which the magnetic orientations are randomly aligned as shown in Fig 2.7. When the external magnetic field is applied, the magnetic field inside the grain tends to align with the external field. Therefore, the grains are rotated to align with the external field and as a result the medium can be elongated in the direction of the external field as shown in Fig. 2.7. However, the external field in both positive and negative  $x$  direction elongates the medium. If a strong static magnetic field is applied first, then the mechanical response is in the same direction with the dynamic magnetic field. In other words, magnetostrictive material is stretched when the dynamic field is in same direction with the static field and the material is contracted when the dynamic field is in opposite direction with the static field as shown in Fig. 2.8.

Magnetostrictive effect can be also applied to make a shear deformation. When the static magnetic field is strong enough so that the grains are aligned in the direction of the static field, dynamic magnetic field applied perpendicular to the static magnetic field rotates the grain direction (Fig. 2.9). The rotation means shear deformation.

When the dynamic magnetic field is small enough compared to the static magnetic field, the deformation of the material can be assumed to be linear to the dynamic magnetic field. This relation can be written as below:

$$\mathbf{S}_D = \mathbf{C}\mathbf{T}_D + \mathbf{d}^T\mathbf{H}_D, \quad (2.5a)$$

$$\mathbf{B}_D = \mathbf{d}\mathbf{T}_D + \boldsymbol{\mu}\mathbf{H}_D, \quad (2.5b)$$

where  $\mathbf{S}_D = [S_{xx} \ S_{yy} \ S_{zz} \ S_{yz} \ S_{xz} \ S_{xy}]^T$  is engineering strain and  $\mathbf{H}_D = [H_{Dx} \ H_{Dy} \ H_{Dz}]^T$  is the dynamic magnetic field.  $\mathbf{C}$  is the compliance matrix of the material and  $\mathbf{T}_D = [T_{xx} \ T_{yy} \ T_{zz} \ T_{yz} \ T_{xz} \ T_{xy}]^T$  is the stress tensor.  $\boldsymbol{\mu}$  is the permeability of the material and  $\mathbf{B}_D = [B_{Dx} \ B_{Dy} \ B_{Dz}]^T$  is the magnetic flux density.  $\mathbf{d}$  denotes the coupling coefficient of magnetostriction.

As we assume  $x$  direction is the direction of the static magnetic field and thin magnetostrictive patch is on  $x$ - $y$  plane, the coupling coefficient  $\mathbf{d}$  can be written as below:

$$\mathbf{d} = \begin{bmatrix} d_{11} & d_{12} & d_{12} & 0 & 0 & 0 \\ 0 & 0 & 0 & 0 & d_{35} & 0 \\ 0 & 0 & 0 & d_{35} & 0 & 0 \end{bmatrix}. \quad (2.6)$$

The components of  $\mathbf{d}$  are functions of the magnitude of the static magnetic field. The form in equation (2.6) shows that the dynamic magnetic field parallel to the static magnetic field makes normal strain, and the dynamic field perpendicular to the static field generates shear strain in the magnetostrictive patch.

Using magnetostrictive mechanism, many magnetostrictive transducers are developed [47-50] to generate bulk mechanical waves. However, using a thin magnetostrictive patch, they are effective to generate guided waves in a plate [17, 22, 23, 51]. MPT consists of a magnetostrictive patch, permanent magnets and a coil as shown in Fig. 2.10. The permanent magnets are set to make the static magnetic field and the coil carrying electric signal makes the dynamic magnetic field.

### **2.2.3 Pin-force modeling of ultrasonic transducers**

The wave generation mechanism of ultrasonic transducers can be simply modeled as concentrated forces applied in the waveguide [33, 52]. The consequent displacement of the patch in PZT or MPT is the source of the wave generation. Therefore, it is reasonable to assume a reaction force between the edge of the transducer and the underlying plate. Then the plate is subjected to the concentrated forces at the location

where the edges of transducer. The pair of concentrated forces are in opposite sign as illustrated in Fig. 2.11. For S0 wave source, such as PZT, the force direction is parallel to the wave propagating direction as shown in Fig. 2.11(a). For SH0 wave source, such as MPT, the force direction is perpendicular to the wave propagating direction as shown in Fig. 2.11(b).

The fundamental source concentrated force of a PZT (or MPT) is the electric force (magnetic force) inside the piezoelectric (magnetostrictive) material. The electric or magnetic force only depends on the material parameter and input electric signal. Therefore, the force is one of the characteristics of the transducer and does depend on the structure on which the transducer is attached.

### **2.3 Effective medium theory**

For subwavelength dimensional heterogeneous material, it can be seen as a new homogeneous effective medium by observing its wave phenomena [6]. Many metamaterials are composed of subwavelength dimensional unit cells. They are analyzed as homogeneous medium having the same constitutive relation but different material parameters with the natural materials, which equivalently act as the original metamaterials.

In electromagnetics, to find such effective material parameters, many methods, including S-parameter retrieval methods [6] are suggested. They have been useful methods to define the effective parameters accurately. By observing the scattered field. The method is successfully applied to acoustic metamaterial [28]. However, the methods have been applied to elastic metamaterials with some modifications due to the complex constitutive relations of elasticity [53].

For infinite plane wave or one-dimensional beam wave, the retrieval method can be simplified as Fig. 2.12. For the homogeneous medium, a wave is incident from the medium 1 having impedance  $z_1$  and wavenumber  $k_1$ , to medium 2 having impedance  $z_2$  and wavenumber  $k_2$ . After traveling in medium 2 for its medium length  $\delta$ , the wave is transmitted to medium 1 again. The incident wave is denoted as  $A$ , reflected wave is denoted as  $B$  and the transmitted wave is denoted as  $C$ . Then the transmittance  $C/A$  and reflectance  $B/A$  can be expressed as below:

$$\frac{B}{A} = \frac{z_2^2 - z_1^2}{z_1^2 + z_2^2 + 2iz_1z_2 \cot k_2\delta / 2}, \quad (2.7a)$$

$$\frac{C}{A} = \frac{1 + \frac{B}{A}}{\cos(ik_2\delta/2) - i\frac{z_2}{z_1}\sin(ik_2\delta/2)}. \quad (2.7b)$$

By rearranging equation (2.7),  $z_2/z_1$  and  $k_2$  can be expressed with respect to the transmittance and reflectance as below:

$$\cos k_2\delta = \frac{A}{2C} \left[ 1 - \left( \frac{B}{A} \right)^2 + \left( \frac{C}{A} \right)^2 \right], \quad (2.7a)$$

$$\frac{z_2}{z_1} = \sqrt{\frac{(1 + B/A)^2 - (C/A)^2}{(1 - B/A)^2 - (C/A)^2}}. \quad (2.7b)$$

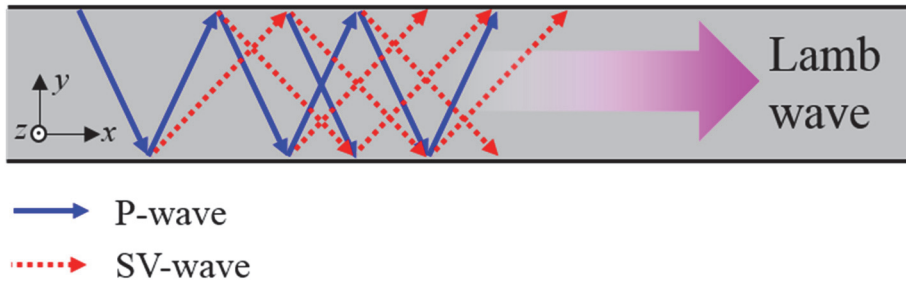


Figure 2.1 Superposition of P-wave and SV-wave in a plate, yielding Lamb waves.

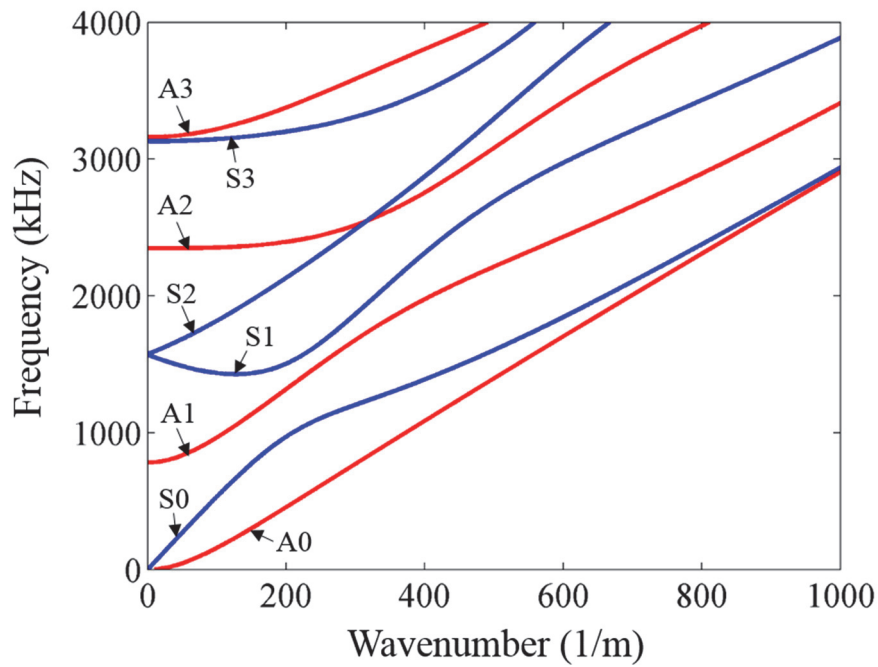
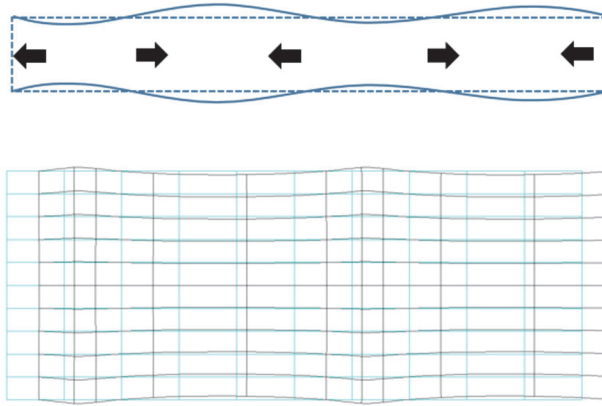


Figure 2.2 Dispersion curve of aluminum plate (thickness of 2 mm) calculated with DISPERSE [39].

(a) S0 wave



(b) A0 wave

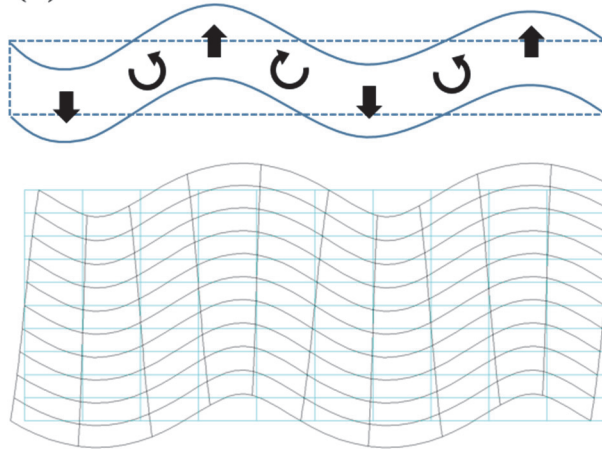


Figure 2.3 Mode shapes of (a) S0 wave and (b) A0 wave in a 2 mm aluminum plate at frequency of 200 kHz calculated by DISPERSE[39]. The particle motion of S0 wave is dominantly in longitudinal direction, and the particle motion of A0 wave is in both out-of-plane and rotating direction.

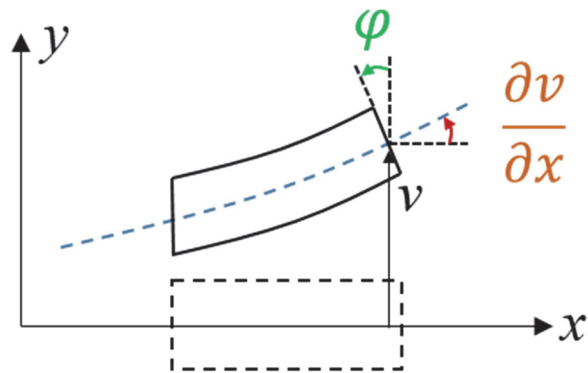


Figure 2.4 Kinematics of Timoshenko beam in an infinitesimal element.  $\varphi$  is the rotation angle and  $v$  is the displacement of the beam.

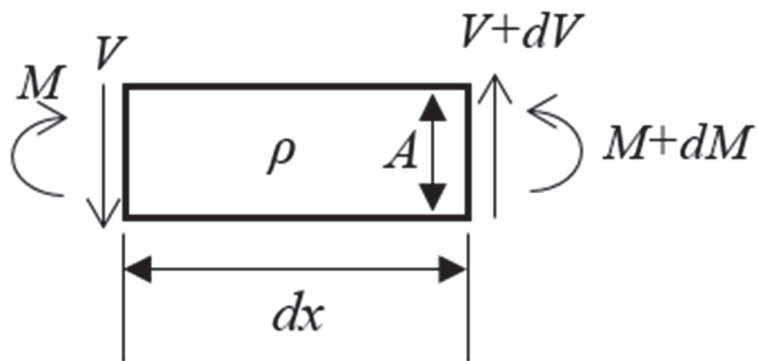


Figure 2.5 Infinitesimal element of Timoshenko beam (length of  $dx$  and cross-sectional area of  $A$ ) showing force equilibrium.  $V$  denotes shear force and  $M$  denotes moment.

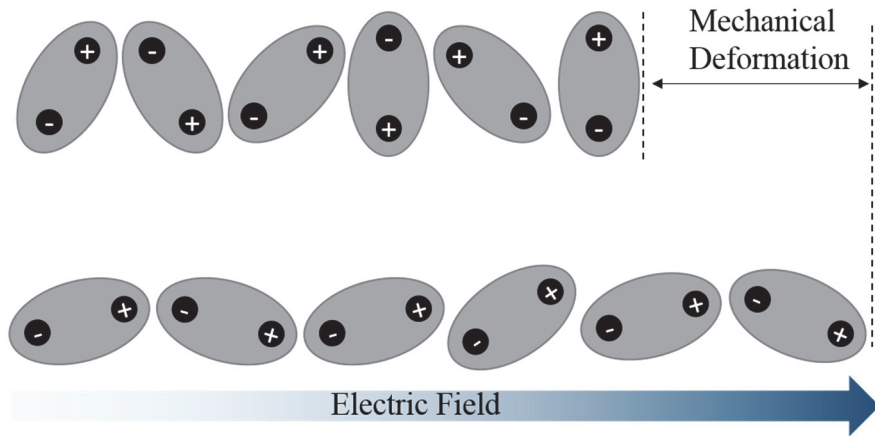


Figure 2.6 Mechanical longitudinal deformation of piezoelectric elements under external electric field.

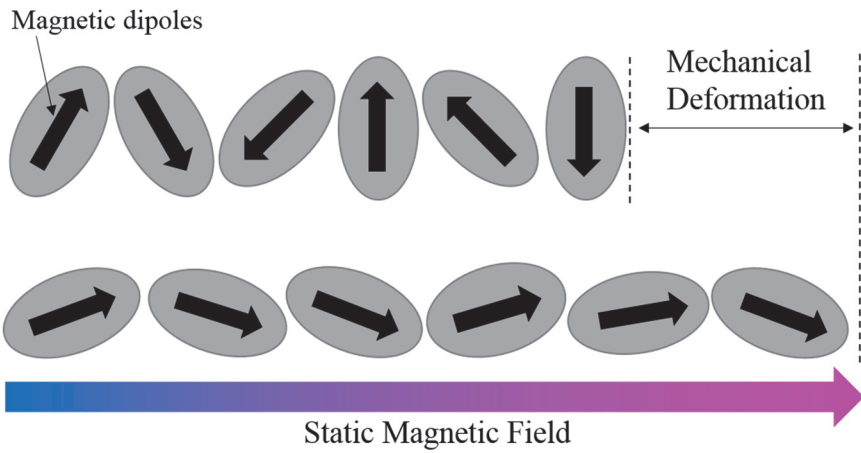


Figure 2.7 Mechanical longitudinal deformation of magnetostrictive elements under static magnetic field.

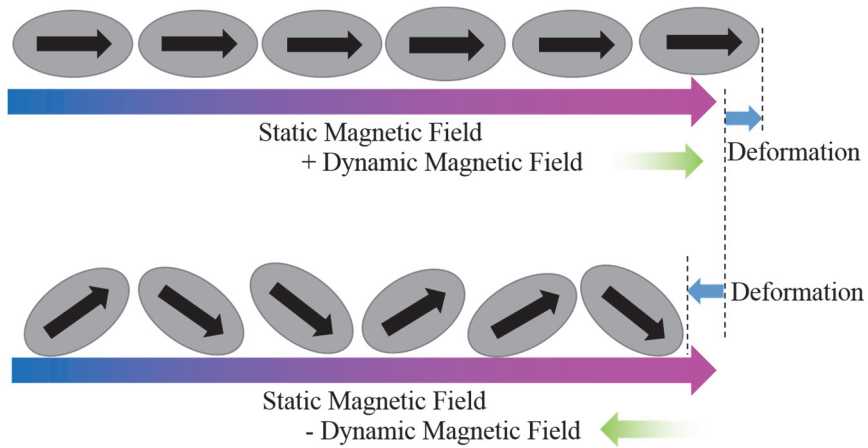


Figure 2.8 Dynamic longitudinal deformation of magnetostrictive elements under static magnetic field with parallel dynamic magnetic field.

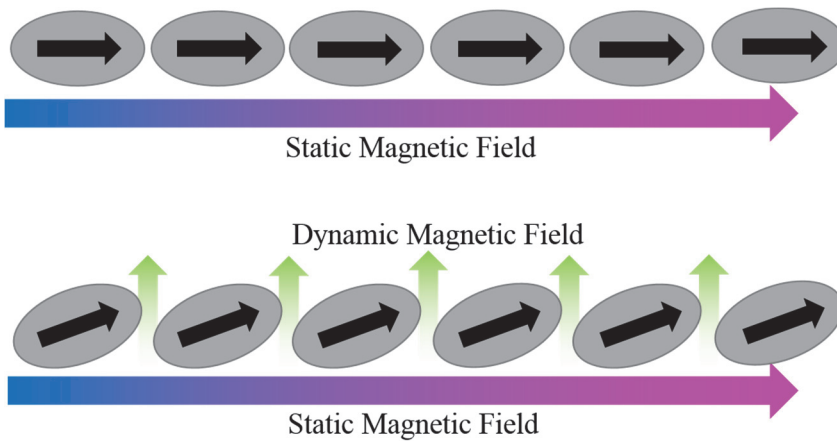


Figure 2.9 Dynamic shear deformation of magnetostrictive elements under static magnetic field with perpendicular dynamic magnetic field.

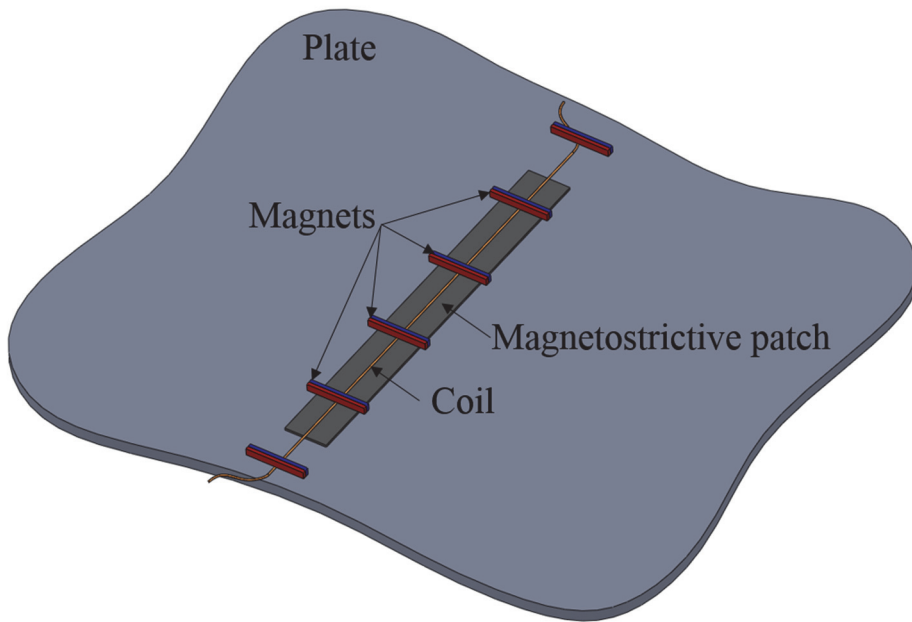


Figure 2.10 Configuration of magnetostrictive patch transducer (MPT) for shear-horizontal wave transduction. MPT is consisted of magnetostrictive patch, permanent magnets and coil.

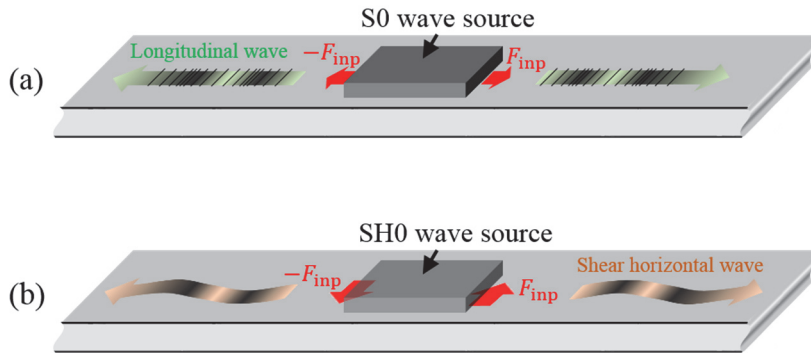


Figure 2.11 Concentrated force modeling of wave generation principle of transducers.

(a) Forces in parallel direction with propagating direction of S0 wave and

(b) Forces in perpendicular direction with propagating direction of SH0

wave.

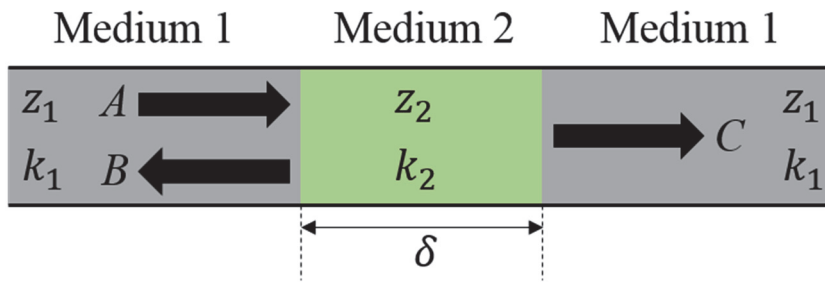


Figure 2.12 Transmitted ( $C$ ), reflected ( $B$ ) wave for incident wave ( $A$ ) from medium

1 embedded with medium 2. Medium 1 has impedance of  $z_1$  and

wavenumber of  $k_1$  and medium 2 has impedance of  $z_2$  and

wavenumber of  $k_2$ .

# **CHAPTER 3.**

## **PROPOSITION OF EQUIVALENT SYSTEM THEORY OF RESONATOR PAIRING**

In this chapter, we show that if a domain of a waveguide is surrounded by a pair of resonators, the effective impedance of the region can be reduced to nearly zero. It is conventionally known that a single resonator applied in a structure can eliminate the vibrations of a harmonically excited system as a dynamic absorber [54]. Also it is widely known that a set of periodically arranged resonators frequently used to make metamaterials can yield an extreme density or stiffness value [55-58]. Here, we show that a pair of resonators can affect the effective impedance of the region surrounded by them, using equivalent system. Through this investigation, it is shown that if a pair of resonators is used, the effective density and stiffness of the region that they

surround vary identically as functions of the frequency. Thereby, only the effective impedance can attain an extremely low value, while the effective phase velocity remains unchanged. The detailed analysis in a one-dimensional beam will be given below.

### 3.1 Resonator-paired waveguide system

To analyze the wave motion in the original one-dimensional model with two resonators, we only consider the longitudinal motion and thus use the field variables shown in Fig. 3.1. The resonator consists of mass  $m$  and stiffness  $s$ , and it is attached onto the bar at  $Q$  (and  $Q'$ ). The longitudinal displacement of mass  $m$  is defined as  $u_R$ . The displacement field in the bar will be denoted by  $u$ , and its value at point  $Q$  is denoted by  $u_Q$ . Considering the symmetric nature of the actuation force with respect to  $x = 0$  in the uniform bar, the resulting displacement fields must also be symmetric. Depending on the values of  $x \geq 0$ ,  $u$  is expressed using different formulas such as  $u = u_1 e^{-ikx} - u_1 e^{ikx}$  ( $0 \leq x \leq L^-$ ),  $u = u_2 e^{-ikx} + u_3 e^{ikx}$  ( $L^+ \leq x \leq W^-$ ), and  $U e^{-ikx}$  ( $W^+ \leq x$ ). Here, the frequency dependence  $e^{i\omega t}$  is also omitted, and  $k$  denotes the wavenumber. Considering the field symmetry, the displacement in the bar can be written as:

$$u = \begin{cases} -Ue^{ikx} & (x \leq -W) \\ -u_2e^{ikx} - u_3e^{-ikx} & (-W \leq x \leq -L) \\ u_1e^{-ikx} - u_1e^{ikx} & (-L \leq x \leq L) \\ u_2e^{-ikx} + u_3e^{ikx} & (L \leq x \leq W) \\ Ue^{-ikx} & (W \leq x) \end{cases} . \quad (3.1)$$

The continuity and equilibrium conditions at  $x = L$  (and  $x = -L$ ) yield:

$$u_1e^{-ikL} - u_1e^{ikL} = u_2e^{-ikL} + u_3e^{ikL}, \quad (3.2)$$

$$-iz_0\omega(u_1e^{-ikL} + u_1e^{ikL}) = F_{\text{inp}} - iz_0\omega(u_2e^{-ikL} - u_3e^{ikL}). \quad (3.3)$$

Note that the internal force considered in the force equilibrium in equation (3.3) is calculated as  $EA_0 \partial u / \partial x$ , where the stiffness  $E$  denotes Young's modulus of elasticity, and  $A_0 = b_0 t_0$  ( $b_0$ : width), which is the cross-sectional area of the bar. If  $\rho$  is defined as the volume density, the characteristic impedance  $z_0$  is given by  $A_0 \sqrt{\rho E}$ .

The continuity and equilibrium conditions at Q yield:

$$u_2e^{-ikW} + u_3e^{ikW} = Ue^{-ikW} \equiv u_Q, \quad (3.4)$$

$$-iz_0\omega(u_2e^{-ikW} - u_3e^{ikW}) = s(u_R - u_Q) - iz_0\omega Ue^{-ikW}. \quad (3.5)$$

On the other hand, the equation of motion for resonator mass  $m$  is given by:

$$-m\omega^2 u_R + s(u_R - u_Q) = 0. \quad (3.6)$$

The expression for  $U$  can be obtained by solving equations (3.2–3.6):

$$U = \frac{2F_{\text{inp}}}{iz_0\omega} \frac{\sin kL}{\alpha(1 - e^{-2ikW}) - 2i}, \quad (3.7)$$

with

$$\alpha = \frac{1}{z_0} \frac{m\omega s}{s - m\omega^2} = \frac{1}{z_0} \frac{\omega s}{\omega_R^2 - \omega^2}. \quad (3.8)$$

where  $\omega_R = 2\pi f_R = \sqrt{s/m}$  is the resonance frequency of the resonator. If no resonator is installed (i.e.,  $m = 0$  or  $s = 0$ ), the resulting displacement will be denoted as  $U_0$ :

$$U_0 = \frac{F_{\text{inp}}}{z_0\omega} \sin kL. \quad (3.9a)$$

The strain that is defined as  $S = \partial u / \partial x = -ikU$  ( $S_0 = -ikU_0$ ) is more convenient to use because the PZT transducer generates and measures the strain [59]:

$$S = -k \frac{2F_{\text{inp}}}{z_0\omega} \frac{\sin kL}{\alpha(1 - e^{-2ikW}) - 2i} = -\frac{2F_{\text{inp}}}{EA_0} \frac{\sin kL}{\alpha(1 - e^{-2ikW}) - 2i}, \quad (3.9b)$$

and

$$S_0 = -i \frac{kF_{\text{inp}}}{z_0 \omega} \sin kL = -i \frac{F_{\text{inp}}}{EA_0} \sin kL . \quad (3.9c)$$

The strain magnitude  $|S_0|$  will reach its maximum value  $|S_0^{f_T}| = |F_{\text{inp}}| / EA_0$  at the frequency of  $f_T = c / 4L$ , which corresponds to  $kL = \pi / 2$ . Here,  $|F_{\text{inp}}|$  is assumed to be frequency-independent.

The magnitude of transducer output with and without the resonators are depicted in Fig. 3.2. The mass and stiffness of the resonators are  $m = 58.9$  g and  $s = 38.5$  GN/m, yielding the resonant frequency  $f_R = 128.7$  kHz. The plate was assumed as 2 mm thickness aluminum plate. Using the resonators, the transducer output has been influenced. The important feature is that the output is increased compared to that without the resonators at the frequency at which the maximum output of transducer without the resonators occurs.

### 3.2 Equivalent medium of the paired resonator system

The wave behavior observed in the original model shown at the top of Fig. 3.3 can also be analyzed using the equivalent model shown at the bottom of Fig. 3.3. In the equivalent model, we must estimate the new effective impedance  $z$  of the region confined between  $x = -W'$  and  $x = W'$ . The displacement field  $\tilde{u}$  in the

equivalent model shown in Fig. 3.3 may be expressed as

$$\tilde{u} = \begin{cases} -\tilde{U}e^{ikx} & (x \leq -W') \\ -\tilde{u}_2e^{ikx} - \tilde{u}_3e^{-ikx} & (-W' \leq x \leq -L) \\ \tilde{u}_1e^{-ikx} - \tilde{u}_1e^{ikx} & (-L \leq x \leq L) \\ \tilde{u}_2e^{-ikx} + \tilde{u}_3e^{ikx} & (L \leq x \leq W') \\ \tilde{U}e^{-ikx} & (W' \leq x) \end{cases} . \quad (3.10)$$

The field variables  $\tilde{u}_i$  ( $i=1,2,3$ ) and  $\tilde{U}$  are related to each other by the continuity and equilibrium conditions at  $x=L$  and  $x=W'$  as

$$\tilde{u}_1e^{-ikL} - \tilde{u}_1e^{ikL} = \tilde{u}_2e^{-ikL} + \tilde{u}_3e^{ikL} , \quad (3.11)$$

$$-iz\omega(\tilde{u}_1e^{-ikL} + \tilde{u}_1e^{ikL}) = \tilde{F}_{\text{inp}} - iz\omega(\tilde{u}_2e^{-ikL} - \tilde{u}_3e^{ikL}) , \quad (3.12)$$

$$\tilde{u}_2e^{-ikW'} + \tilde{u}_3e^{ikW'} = \tilde{U}e^{-ikW'} , \quad (3.13)$$

$$-iz\omega(\tilde{u}_2e^{-ikW'} - \tilde{u}_3e^{ikW'}) = -iz_0\omega\tilde{U}e^{-ikW'} . \quad (3.14)$$

Our approach to evaluate  $z$  and  $W'$  is to make the wave field in the equivalent system equal to that in the original system with two point-resonators. Accordingly, we require that the following conditions be fulfilled:

$$\tilde{U} = U , (\text{for } x \geq W') , \quad (3.15)$$

$$\frac{\tilde{u}_1}{u_1} = \frac{\tilde{u}_2}{u_2} = \frac{\tilde{u}_3}{u_3} = g(\omega), \quad (3.16)$$

$$\frac{\tilde{F}_{\text{inp}}}{F_{\text{inp}}} = h(\omega), \quad (3.17)$$

where  $g(\omega)$  and  $h(\omega)$  are unknown functions of  $\omega$  to be determined for the exact equivalence. The wave number  $k$  must be the same in the two systems to ensure the same wave behavior. Based on the analysis given in following section, it can be shown that waves in the equivalent system behave in the same way as those in the original system if the following relations hold:

$$\frac{z}{z_0} = \frac{1 - |r|}{1 + |r|}, \quad (3.18a)$$

$$W' = W + \frac{1}{2k}(\beta + 2n\pi), \quad (n: \text{integer}), \quad (3.18b)$$

$$\frac{z}{z_0} = \frac{1 + |r|}{1 - |r|}, \quad (3.19a)$$

$$W' = W + \frac{1}{2k}(-\beta + 2n\pi), \quad (n: \text{integer}), \quad (3.19b)$$

$$g(\omega) = \sqrt{\frac{z_0}{z}} e^{i(\beta + p\pi/2)}, \quad (p = \text{sign}(\omega - \omega_R)), \quad (3.20a)$$

$$h(\omega) = \sqrt{\frac{z}{z_0}} e^{i(\beta + p\pi/2)}, \quad (p = \text{sign}(\omega - \omega_R)). \quad (3.20b)$$

where  $r$  and  $\beta$  are defined as

$$r = \frac{\omega s}{2iz_0(\omega_R^2 - \omega^2) - \omega s}, \quad (3.21a)$$

$$\beta = \arg(r). \quad (3.21b)$$

Now the derivation of the effective parameters  $z$  and  $W'$ , and the functions  $g(\omega)$  and  $h(\omega)$  will be derived here. For this derivation, it is convenient to write  $g(\omega)$  and  $h(\omega)$  as

$$\frac{\tilde{u}_1}{u_1} = \frac{\tilde{u}_2}{u_2} = \frac{\tilde{u}_3}{u_3} \equiv g(\omega) = |g(\omega)| e^{i\theta}, \quad (3.22)$$

$$\frac{\tilde{F}_{\text{inp}}}{F_{\text{inp}}} = h(\omega) = |h(\omega)| e^{i\gamma}. \quad (3.23)$$

If equations (3.22–3.23) are substituted into equation (3.11), equation (3.11) identically reduces to equation (3.2). In the case of equation (3.12), it can be written in terms of  $u_1$ ,  $u_2$ , and  $F_{\text{inp}}$  as

$$-iz\omega \frac{g(\omega)}{h(\omega)} (u_1 e^{-ikL} + u_1 e^{ikL}) = F_{\text{inp}} - iz\omega \frac{g(\omega)}{h(\omega)} (u_2 e^{-ikL} - u_3 e^{ikL}), \quad (3.24)$$

which reduces to equation (3.3) if the following relation holds

$$\frac{g(\omega)}{h(\omega)} = \frac{z_0}{z}. \quad (3.25)$$

By the power flow equivalence of the two systems, the following relation must hold:

$$P_{\text{in}} \Big|_{\text{original}} = P_{\text{in}} \Big|_{\text{equiv}}, \quad (3.26)$$

where

$$\begin{aligned} P_{\text{in}} \Big|_{\text{original}} &= \frac{1}{2} \text{Re} \left\{ F_{\text{original}} v_{\text{original}}^* \right\}_{x=L} \\ &= \frac{1}{2} \text{Re} \left\{ F_{\text{inp}} \left[ i\omega(u_1 e^{-ikL} - u_1 e^{ikL}) \right]^* \right\} \\ &= \frac{1}{2} \text{Re} \left\{ F_{\text{inp}} 2\omega \sin kx |u_1| e^{-i\eta} \right\} = F_{\text{inp}} \omega \sin kx |u_1| \cos \eta \end{aligned} \quad (3.27)$$

and

$$\begin{aligned} P_{\text{in}} \Big|_{\text{equiv}} &= P_{\text{in}} \Big|_{\text{equiv}} = \frac{1}{2} \text{Re} \left\{ F_{\text{equiv}} v_{\text{equiv}}^* \right\}_{x=L} \\ &= \frac{1}{2} \text{Re} \left\{ F_{\text{inp}} h(\omega) \left[ i\omega g(\omega) (u_1 e^{-ikL} - u_1 e^{ikL}) \right]^* \right\} \\ &= F_{\text{inp}} \omega \sin kx |u_1| \cos(\eta + \theta - \gamma) |h(\omega)| |g(\omega)| \end{aligned} \quad (3.28)$$

In equations (3.26–3.28),  $F_{\text{original}} = F_{\text{inp}} e^{i\omega t}$ ,  $F_{\text{equiv}} = \tilde{F}_{\text{inp}} e^{i\omega t}$ , and  $v$  is the particle velocity. The symbol  $*$  denotes the complex conjugate, and  $u_1 = |u_1| e^{i\eta}$ . From equations (3.26–3.28), one can find

$$|h(\omega)| |g(\omega)| = 1, \quad (3.29)$$

$$\theta = \gamma. \quad (3.30)$$

By using equations (3.25, 3.29, 3.30),  $g(\omega)$  and  $h(\omega)$  can be found as

$$g(\omega) = \sqrt{\frac{z_0}{z}} e^{i\theta}, \quad (3.31)$$

$$h(\omega) = \sqrt{\frac{z}{z_0}} e^{i\theta}, \quad (3.32)$$

but  $z$  and  $\theta$  are yet to be determined.

To determine  $z$  and  $\theta$ , we eliminate  $\tilde{U}$  by using equations (3.13, 3.14) and obtain

$$\frac{\tilde{u}_3 e^{ikW'}}{\tilde{u}_2 e^{-ikW'}} = \frac{z - z_0}{z + z_0}. \quad (3.33)$$

Equation (3.33) can be reduced to equation (3.34) by using equation (3.16),

$$\frac{u_3 e^{ikW'}}{u_2 e^{-ikW'}} = \frac{z - z_0}{z + z_0} \quad (3.34)$$

From equation (3.6), it is possible to derive the following relation:

$$s(u_R - u_Q) = \frac{ms\omega^2}{s - m\omega^2} u_Q = \frac{s\omega^2}{\omega_R^2 - \omega^2} u_Q. \quad (3.35)$$

Combining equations (3.4), (3.5), and (3.35) yields

$$\begin{aligned} -iz_0\omega(u_2 e^{-ikW} - u_3 e^{ikW}) &= \left( \frac{s\omega^2}{\omega_R^2 - \omega^2} - iz_0\omega \right) u_Q \\ &= \left( \frac{s\omega^2}{\omega_R^2 - \omega^2} - iz_0\omega \right) (u_2 e^{-ikW} + u_3 e^{ikW}) \end{aligned} \quad (3.36)$$

By rearranging equation (3.36), the following result can be obtained:

$$\frac{u_3 e^{ikW}}{u_2 e^{-ikW}} = \frac{s\omega}{2iz_0(\omega_R^2 - \omega^2) - s\omega} \equiv r = |r| e^{i\beta}. \quad (3.37)$$

From equations (3.34) and (3.37),

$$\frac{z}{z_0} = \frac{1 + r e^{2ik(W'-W)}}{1 - r e^{2ik(W'-W)}} = \frac{1 + |r| e^{i[\beta + 2k(W'-W)]}}{1 - |r| e^{i[\beta + 2k(W'-W)]}}. \quad (3.38)$$

To show that  $z$  is real-valued, we use the fact that the power flow consideration must

be valid for the original at  $x = W$  and for the equivalent systems at  $x = W'$ , which are expressed as

$$z_0 |u_2|^2 = z_0 |u_3|^2 + z_0 |U|^2 \quad \text{for the original system,} \quad (3.39)$$

$$\operatorname{Re}(z) |\tilde{u}_2|^2 = \operatorname{Re}(z) |\tilde{u}_3|^2 + z_0 |\tilde{U}|^2 \quad \text{for the equivalent system.} \quad (3.40)$$

Substituting equations (3.15–3.16) and equation (3.31) into (3.40) yields

$$\frac{\operatorname{Re}(z)}{|z|} |u_2|^2 = \frac{\operatorname{Re}(z)}{|z|} |u_3|^2 + |U|^2. \quad (3.41)$$

Comparing equations (3.39) and (3.41) ensures that  $z$  should be real-valued. Therefore,  $z$  can be real when  $\beta + 2k(W' - W) = 2n\pi$  or  $(2n+1)\pi$ , where  $n$  is an integer.

We first consider the case where  $\beta + 2k(W' - W) = 2n\pi$  ( $n$ : integer), i.e.,

$$W' = W + \frac{1}{2k}(2n\pi - \beta). \quad (3.42)$$

In this case,  $z$  is given by

$$\frac{z}{z_0} = \frac{1+|r|}{1-|r|} > 1. \quad (3.43)$$

When  $\beta + 2k(W' - W) = (2n+1)\pi$ , i.e.,

$$W' = W + \frac{1}{2k} [(2n+1)\pi - \beta], \quad (3.44)$$

and  $z$  is given by

$$\frac{z}{z_0} = \frac{1-|r|}{1+|r|} < 1. \quad (3.45)$$

In our study, the result in equation (3.43) will be used because we are interested in  $z < z_0$ .

In the following part, we will derive equations (3.20a, b). For this derivation, we first note the following relation, which can be obtained from equations (3.13–3.16) and equation (3.45),

$$\frac{\tilde{U}}{\tilde{u}_2} = \frac{U}{gu_2} = \frac{2z}{z_0 + z} = 1 - |r|. \quad (3.46)$$

Using equation (3.4) and equation (3.37), it is possible to obtain

$$\frac{U}{u_2} = 1 + \frac{u_3}{u_2} e^{2ikW} = 1 + r. \quad (3.47)$$

Then,  $g(\omega)$  can be explicitly written only in terms of  $r$  as

$$g(\omega) = \frac{1+r}{1-|r|} = \frac{1+|r|(\cos \beta + i \sin \beta)}{1-|r|} \equiv |g(\omega)| e^{i\theta}. \quad (3.48)$$

where  $r$  is expressed as  $r = |r| \cos \beta + i |r| \sin \beta$ . If equation (3.37) and equation (3.47) are substituted into equation (3.39), the following relation can be derived:

$$1 = |r|^2 + |1+r|^2, \quad (3.49)$$

The substitution of  $r = |r| \cos \beta + i |r| \sin \beta$  into equation (3.49) yields the expression to determine  $\beta$ :

$$\cos \beta = -|r|, \quad (3.50)$$

Taking the absolute value of both sides of equation (3.48) and using equation (3.49),  $|g(\omega)|$  is found to be

$$|g(\omega)| = \frac{|1+r|}{1-|r|} = \frac{\sqrt{1-|r|^2}}{1-|r|} = \sqrt{\frac{1+|r|}{1-|r|}} = \sqrt{\frac{z_0}{z}}. \quad (3.51)$$

The phase of  $g(\omega)$  can be found from equations (3.48) and (3.50) as

$$\tan \theta = \frac{|r| \sin \beta}{1+|r| \cos \beta} = \frac{-\cos \beta \sin \beta}{1-\cos^2 \beta} = -\frac{1}{\tan \beta},$$

$$\tan \theta = -\frac{1}{\tan \beta}. \quad (3.52)$$

Referring to the definition of  $r$  given in equation (3.37), the range of  $\beta$  varies depending on  $\omega$  as

$$\pi < \beta < 3\pi/2 \quad \text{when } \omega < \omega_R, \quad (3.53)$$

$$\pi/2 < \beta < \pi \quad \text{when } \omega > \omega_R.$$

Therefore,  $\theta$  is determined as

$$\theta = \begin{cases} \beta - \pi/2, & (\omega < \omega_R) \\ \beta + \pi/2, & (\omega > \omega_R) \end{cases}. \quad (3.54)$$

More compactly,  $\theta = \beta + p\pi/2$  with  $p = \text{sign}(\omega - \omega_R)$ , as given in equation (3.20).

### 3.3 Effective properties of the equivalent system

Equations (3.18–3.19) show that  $z$  and  $W'$  vary as functions of  $\omega$ ,  $m$ , and  $\beta$ , while Equation (3.18a) yields an effective impedance  $z$  that is smaller than  $z_0$ , equation (3.19a) yields a value of  $z$  that is larger than  $z_0$ . Because we are interested in the case where  $z < z_0$  given in equation (3.18a), the effective length  $W'$  should

be estimated from equation (3.18b). Equation (3.18) shows that the solution for  $W'$  is not unique, but it is possible to select a value close to  $W$  for convenience. It should be noted that if  $W' = W$ , the magnitude and phase of  $\tilde{U}$  cannot be the same as those of  $U$ . (Moreover, it can also be shown that the solution in equation (3.19) also magnifies the radiated  $U$  field, but we use equation (3.18) here because our work is motivated by the realization of a near-zero or lowered effective impedance.)

Using the above analysis, it is possible to derive the explicit formula for  $U$  (for  $x > W'$ ) as

$$\begin{aligned}
 U = \tilde{U} &= \frac{\tilde{F}_{\text{inp}} \sin kL}{z_0 \omega} \frac{z_0 e^{ikW'}}{iz_0 \sin kW' + z \cos kW'} \\
 &= U_0 \frac{\sqrt{zz_0} e^{i(kW' + \beta + p\pi/2)}}{iz_0 \sin kW' + z \cos kW'}, \quad (p = \text{sign}(\omega - \omega_R)).
 \end{aligned} \tag{3.55}$$

where  $U_0$  is the nominal displacement defined in equation (3.9). From equation (3.55), the following can be derived:

$$S = \tilde{S} = S_0 \frac{\sqrt{zz_0} e^{i(kW' + \beta + p\pi/2)}}{iz_0 \sin kW' + z \cos kW'}, \quad (p = \text{sign}(\omega - \omega_R)). \tag{3.56}$$

Because the near-zero impedance can increase the radiated field, as demonstrated in

Fig. 1.1 and Fig. 1.2, we aim to also increase  $|S|$  in equation (3.56). Therefore, it is possible to consider the case where both  $|S_0|$  and  $\sqrt{zz_0} / \sqrt{z_0^2 \sin^2 kW' + z^2 \cos^2 kW'}$  are maximized. (Because we can experimentally measure  $|S|$ , an analysis of  $|S|$  is needed to estimate  $z$ .) If  $f = f_T$  is selected,  $|S_0|$  will be the largest, which is denoted by  $|S_0^{f_T}|$ . Therefore, the expression for the normalized magnitude  $|S / S_0^{f_T}|$  becomes

$$\left| \frac{S(\omega)}{S_0^{f_T}} \right| = \frac{\sqrt{zz_0}}{\sqrt{z_0^2 \sin^2 kW' + z^2 \cos^2 kW'}} \left| \frac{S_0(\omega)}{S_0^{f_T}} \right|. \quad (3.57)$$

Equation (3.57) reveals that  $|S|$  can be amplified by a factor of  $\sqrt{z_0/z}$  compared to nominal amplitude  $|S_0|$  as long as  $\sin kW' = 0$  is satisfied. Because  $k = \omega / c$  ( $c$ : phase velocity) and  $W' = W'(\omega, m, \beta, W)$ ,  $|S / S_0^{f_T}|$  can always be amplified at some frequencies. Furthermore, the frequency satisfying  $\sin kW' = 0$  can be adjusted to match  $f_T$ . This means that it is always possible to select a value of  $W$  that maximizes  $|S / S_0^{f_T}|$  at  $f = f_T$ , yielding the maximally amplified radiated wave field. The maximally enhanced radiated wave field is possible because  $z$  becomes smaller than  $z_0$ .

Figure 3.2 show the behaviors of  $|S/S_0^{f_T}|$  and Fig. 3.4  $z/z_0$  as functions of the excitation frequency  $f$ . Note that because  $\rho$  and  $E$  behave identically as functions of the frequency, the phase velocity remains unchanged. Figure 3.2 shows the behavior of the rapidly growing  $|S|$  as  $f$  approaches  $f_{FP}^*$ , another Fabry–Pérot resonance near  $f = f_R$  for which the theoretical value of the impedance  $z$  becomes zero. If  $f_{FP}^*$  were matched to be  $f_R$ ,  $|S/S_0^{f_T}|$  would theoretically be infinite, and its bandwidth would approach zero. The figure also shows that at  $f = f_T$  where the nominal output strain  $|S_0|$  is maximized,  $|S|$  increases by a factor of 1.9 compared with the nominal value of  $|S_0^{f_T}|$ . This amplification at  $f = f_T$  is due to the two facts that  $z < z_0$  at  $f = f_T$  and  $f_T$  is tuned to be one of the Fabry–Pérot resonances of the effective medium confined within the width of  $2W'$ . In fact, there is a set of Fabry–Pérot resonances satisfying  $\sin kW' = 0$ . These Fabry–Pérot resonance frequencies can be more easily identified by examining the transmission coefficient  $|T| = |C/A|$  shown at Fig. 3.5. Here,  $A$ ,  $B$ , and  $C$  respectively denote the magnitudes of the incident, reflected, and transmitted waves through a slab of width  $2W'$  and impedance  $z$  that is inserted inside a homogeneous medium of impedance  $z_0$ . Equation (3.20) also indicates that  $|S/S_0| = \sqrt{z_0/z} > 1$  for

$\sin kW' = 0$  and  $|S/S_0| = \sqrt{z/z_0} < 1$  for  $\cos kW' = 0$ . Accordingly,  $|S/S_0^{f_T}|$  at  $f = f_T$  can be amplified because  $f = f_T$  satisfies  $\sin kW' = 0$ .

The effects of  $f_R$  on  $|S/S_0^{f_T}|$  near  $f = f_T = 72.6$  kHz are investigated in Fig. 3.6. As  $f_R$  approaches  $f_T$ ,  $|S|$  increases rapidly because  $z_r = z/z_0$  becomes smaller (and the Q value becomes larger). Therefore, by tuning the value of  $z$  using an appropriate value for  $f_R$ , a tradeoff can be always made between the amplitude and bandwidth in  $|S/S_0^{f_T}|$  at target frequency  $f_T$ . The effect of the distance ( $2W$ ) between the two resonators on  $|S|$  is shown in Fig. 3.7, where  $f_R$  is assumed to be fixed. Because only  $W$  is varied, the effective impedance  $z$  does not vary. However, the Fabry–Pérot resonance frequencies in a medium of impedance  $z$  in the region confined between  $2W'$  are varied because  $W'$  varies with  $W$ , as shown in equation (3.18). Therefore, the peak frequency of the locally maximized  $|S|$  is significantly affected by  $W$ . We argue that the phenomenon in Fig. 3.7 cannot be observed if only a single resonator is installed because it only functions as a dynamic absorber [54]. The wave interference occurring between the paired resonators is unique in that it can lower the effective impedance  $z$  of the region surrounded by the resonators, even making it nearly zero.

### 3.4 Frequency selection process

The target frequency is selected to be the optimal frequency of a transducer. It is more meaningful to improve the transducer output at the optimal frequency. As shown in Fig. 3.8(a), optimal frequency of the transducer characteristics is denoted as  $f_T$ . The improvement occurs at the Fabry-Perot frequency, as shown in Eq. (3.57). Therefore,  $W'$  should be tuned to make  $f_T$  to be tuned as the Fabry-Perot frequency satisfying  $\sin kW' = 0$ . As derived in Eq. (3.44),  $W'$  can be tuned with  $W$  with known resonator properties. Figure 3.8(b) shows the frequency characteristics of the transducer with resonators. The Fabry-Perot frequency is tuned to  $f_T$ .

### 3.5 Summary

In this chapter, it is found that the effective impedance  $z$  of a region bounded by a pair of point resonators can become near-zero, or more practically, lower than the nominal impedance  $z_0$ . When the paired-resonator mechanism is used, the effective density and stiffness behave identically as functions of the frequency. Therefore, only the effective impedance can be affected, while the effective phase velocity or refractive index remains unchanged. If the frequency of a lowered effective

impedance is selected to match the Fabry–Pérot resonance frequency of the equivalent system of effective impedance  $z$ , the wave emission by external excitation inside the region bounded by the resonators can be super-enhanced. This super-enhancement can be a critically useful application of the near-zero effective impedance because attaching paired-resonators is an efficient non-destructive method to increase the transduction efficiency of any transducer for both actuation and sensing. Because this method does not require the alteration of a test waveguide or an additional active element, it is not limited to the ultrasonic transducers considered as an example in this study but can open a new way to boost the efficiency of various transducers.

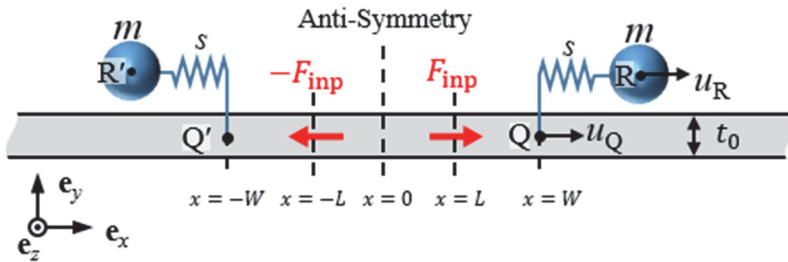


Figure 3.1 Analysis of bar model in which the displacements in various locations are specified. The generation mechanism of transducer is simplified as two concentrated forces at  $x = \pm L$ .

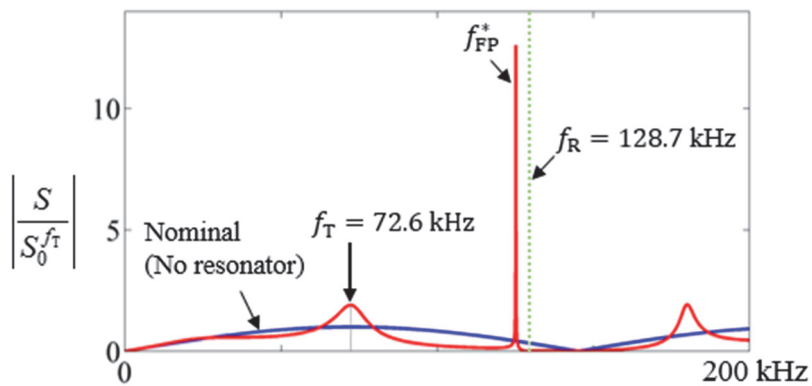


Figure 3.2 The magnitude of radiated strain field in a beam with and without the resonators. The mass and stiffness of the resonators are  $m = 58.9$  g and  $s = 38.5$  GN/m.

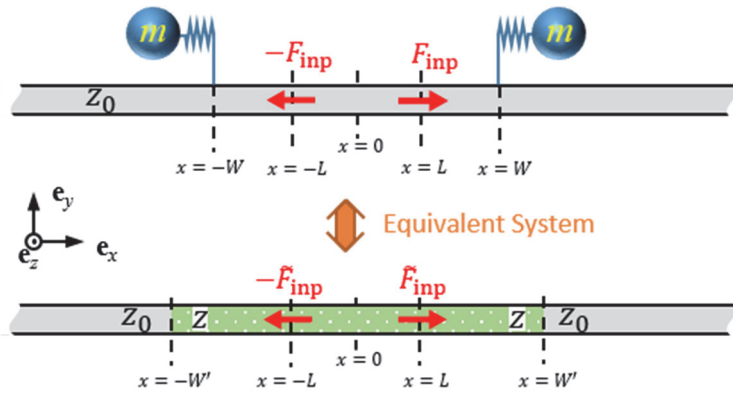


Figure 3.3 One-dimensional bar models describing the longitudinal motion in a plate.

The model in the top illustration depicts a bar equipped with two point-resonators while the model in the bottom illustration is an equivalent bar model with a modified effective impedance to account for the effects of resonators on wave motion.

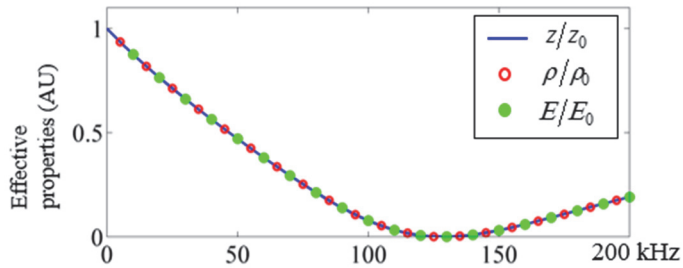


Figure 3.4 Effective impedance  $z$ , density  $\rho$  and stiffness  $E$  in a beam with and without the resonators. The mass and stiffness of the resonators are  $m = 58.9$  g and  $s = 38.5$  GN/m.

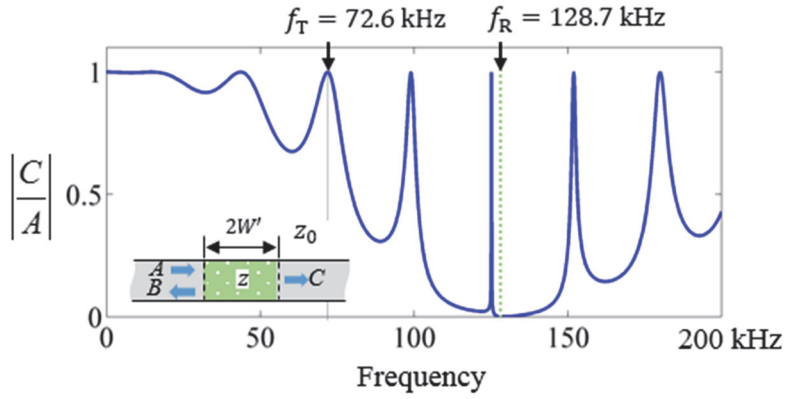


Figure 3.5 Transmission coefficient in the bar configuration shown in the inset of illustration.

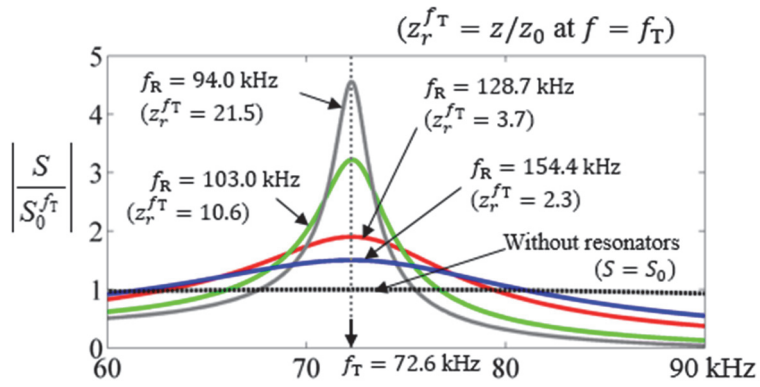


Figure 3.6 The effects of the resonance frequency  $f_R$  on the magnitude of radiated strain  $|S|$ .

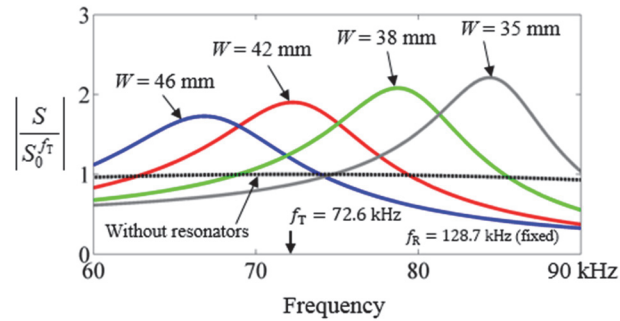


Figure 3.7 The effects of the distance  $W$  between the two resonators on the magnitude of radiated strain  $|S|$ .

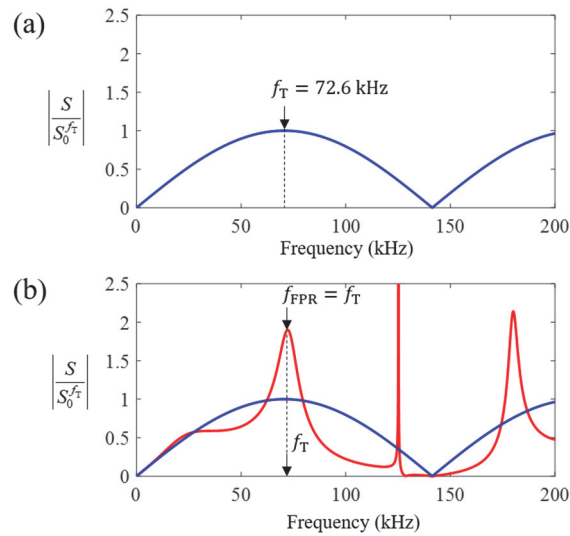


Figure 3.8 Plot of frequency characteristics of (a) a transducer without resonators (b) and the transducer with resonators tuned to Fabry-Pérot frequency to  $f_T$ .

# **CHAPTER 4.**

## **DESIGN OF THE RESONATOR PAIRING FOR LAMB WAVE AND SHEAR-HORIZONTAL WAVE EMISSION ENHANCEMENT**

In this chapter, the realization and experiments for the theory described in chapter 3 will be discussed. In one-dimensional beam, depending on its direction of particle motion, longitudinal wave, shear-horizontal wave and shear-vertical wave can be considered. As the counterparts in waves in a plate, the lowest modes of symmetric Lamb wave and shear-horizontal wave can be considered for the realization. The realized models are copied with S0 wave and SH0 wave in a plate, since S0 Lamb wave at low frequency range (non-dispersive region) can be assumed as the longitudinal wave in a one-dimensional beam and SH0 wave is identical to shear horizontal wave in one-dimensional beam. However, as the counterpart of shear-

vertical wave in the beam, bending wave in a plate will be discussed in chapter 5 because of the complex physical behavior of the wave.

#### 4.1 Realization of the resonator pair for S0 Lamb wave

To examine the frequency behavior of  $|S/S_0^{f_T}|$  in the previous chapter, we used two C-channel box beams made of aluminum, where  $t_R = 1.5$  mm,  $w_R = 6$  mm, and  $h_R = 3$  mm, as shown in Fig. 4.1 (Young's modulus  $E = 66$  GPa, Poisson's ratio  $\nu = 0.33$ , and density  $\rho = 2700$  kg/m<sup>3</sup>). The C-channel beam is the realized version of a point resonator. They were  $2W = 84$  mm away from each other and installed on a 2 mm thick aluminum plate. In a finite element analysis, the mass and stiffness of the resonator were estimated to be  $m = 58.9$  g and  $s = 38.5$  GN/m, yielding  $f_R = 128.7$  kHz. The nominal impedance and phase velocity in the aluminum plate for plane longitudinal wave motion were  $z_0 = 28242$  kg/s and  $c = 5230$  m/s, respectively. A PZT patch with a size of  $L = 18$  mm was used, for which the peak frequency  $f_T = c/4L$  was 72.6 kHz.

In the experiments, we used the lowest symmetric Lamb wave (S0 wave) in a plate because it has a good correspondence to the longitudinal wave propagating in a bar, which can be modeled as a one-dimensional waveguide [60]. Thus, we assumed that

the particle displacement in the plate and the motions of the resonators were all along the  $x$  direction. The resonators were bonded onto the plate using epoxy resin (3M DP100). The cross-sectional geometry of the C-shaped resonators in Fig. 4.1 was the same as that used in Fig. 4.2 ( $t_R = 1.5$  mm,  $w_R = 6$  mm,  $h_R = 3$  mm). They were designed in this way to exhibit dominant vibrations along the  $x$  direction. Indeed, they functioned as mass-spring systems in the frequency range of interest.

To estimate the equivalent stiffness  $s$  and mass  $m$  of the resonator, we used its resonance frequency and static stiffness, as determined using a detailed continuum finite element model. The lowest eigenfrequency  $f_R$  was found to be 128.7 kHz in a numerical simulation [61], and the corresponding eigenmode shown in Fig. 4.2(a) confirmed that the dominant motion of the resonators at the resonance frequency was in the  $x$  direction. The analysis of the eigenmode shape suggested that the pillar part of the resonator worked as a spring, while its upper part worked as a mass in a mass-spring system. Therefore, it was possible to apply  $f_x / 4$  to each of the four pillars of the resonator to evaluate  $s$ , as illustrated in Fig. 4.2(b). The application of force  $f_x / 4$  to each pillar was equivalent to the application of  $f_x$  to the entire resonator. By calculating  $u_R$ , the horizontal displacement of the pillar at its top point R, using a numerical simulation [61], we estimated  $s = 38$  GN/m from the formula  $s = f_x / u_R$ . Then, the mass was calculated to be  $m = 58.9$  g from  $m = s / (2\pi f_R)^2$ .

Referring to Fig. 4.3, three 30 mm × 70 mm × 0.5 mm PZT patches were installed on a 2 mm-thick aluminum plate. We used three patches to ensure plane longitudinal waves. Sine pulses of 12 periods generated by a function generator (Agilent 33250A) were input to the PZT transducer for wave generation. The center frequencies were varied from 65 kHz to 80 kHz in increments of 1 kHz. Another set of PZT patches was installed 1 m away from the transmitters for sensing. The signals from the sensor were amplified through a pre-amplifier (SR 560) and recorded using a digital oscilloscope (LeCroy Waverunner 104MXI). The measurements were performed using a pitch-catch mode. The measured peak-to-peak voltage value  $V_0$  was proportional to the strain  $S_0$  measured by the PZT patch in the plate without the resonators installed. Thus,  $V_0 = |C_1||S_0|^2$  or  $|S_0| = \sqrt{V_0/|C_1|}$ , where  $C_1$  was a calibration constant. If we write  $|S_0^{\max}| = \max(|S_0|)$ , the normalized value can be determined to be  $|S_0/S_0^{\max}| = \sqrt{V_0/\max(V_0)}$ . The frequency of the maximum  $|S_0|$  was found to be 74 kHz in our experiment. However, around the target frequency  $f = f_T = 72.6$  kHz,  $|S_0/S_0^{\max}|$  reached a value of more than 0.99, or nearly the maximum value. Therefore, the discrepancy was found to be within the acceptable tolerance. If the measured peak-to-peak voltage in the plate with the installed resonators is denoted by  $V$ , it can also be expressed as  $V = |C_1||S_0||S|$ ,

where  $S$  is the corresponding strain. Therefore, it is possible to obtain a relation such that  $|S / S_0^{\max}| = |V / (\sqrt{V_0} \max(\sqrt{V_0}))|$ . The results are plotted in Fig. 4.4 in 1 kHz intervals.

For T-shaped resonators for S0 wave, as illustrated in Fig. 4.5, is investigated for super enhancement. However, the resonator experiences rotational motion, as shown in Fig. 4.5. Fig. 4.6 shows the eigenmode of the resonator, and the resonator is in rotational motion. The rotational motion has both horizontal and vertical motion. Based on horizontal motion, the spring and mass constants are estimated as  $s = 19.0$  GN/m,  $m = 31.4$  g. With the constants, the expected wave output is estimated with theory and compared with numerical simulation (FEM). The results are plotted in Fig. 4.7, and the expected wave output characteristics from theory and simulation do not match with each other. It is because of the resonator motion cannot be represented as horizontal resonator as in the theory. Therefore, C-shaped resonator is more compatible with the theory using horizontal resonators.

## 4.2 Realization of the resonator pair for SH0 wave

The theory in Chapter 3 is derived with assumption of longitudinal wave. However, it can be also directly applicable with shear-horizontal wave. With changes in the orientation of particle direction into shear-horizontal direction, the equations and the relations in Chapter 3 remain unchanged. Therefore, the theory for the low impedance and wave enhancing can be used for shear-horizontal wave.

For the realization for SH0 wave in a plate, we used two C-shaped beams made of aluminum, as shown in Fig. 4.8. They are 43 mm away from each other and installed on a 2 mm thick aluminum plate. In a finite element analysis, the mass and stiffness of the resonator were estimated to be  $m = 31.4$  g and  $s = 19.0$  GN/m, yielding  $f_R = 124.0$  kHz. The nominal impedance and phase velocity in the aluminum plate for plane longitudinal wave motion were  $z_0 = 16902$  kg/s and  $c = 3130$  m/s, respectively. A MPT patch with a size of  $L = 9.2$  mm was used, for which the peak frequency  $f_T = c/4L$  was 85.0 kHz.

The particle displacement and resonator displacement are both in  $y$ -direction. The resonator is designed as ‘C’ shape to clearly demonstrate the role of spring and mass. An eigenmode analysis of the resonator is performed as shown in Fig. 4.9(a). The

deformation plot of a cross section of the eigenmode at eigenfrequency ( $f_R$ ) of 124.0 kHz is shown in Fig. 4.9(a). The bottom surfaces of the resonator were kept fixed and the pillar parts of the resonator act as the spring and the top part of the resonator acts as the mass. Thus we measured the spring coefficient by exerting the force on the top surfaces of the pillar parts of the resonator and observing the corresponding displacement as shown in Fig. 4.9(b). The spring coefficient  $s$  is derived by equation (4.1). Similar with the S0 case, the mass coefficient is determined as in equation (4.2).

$$s = \frac{f_z}{u_R} \quad (4.1)$$

$$m = \frac{s}{(2\pi f_R)^2} \quad (4.2)$$

For more point-wised resonator, we used two T-shaped beams made of aluminum, as shown in Fig. 4.10. Since the contact size between the resonator and the plate is more narrow, this can be considered as more point-wised resonator. This can be useful in shorter wavelength in a plate. Therefore, we used T-shaped resonator for realization and experiment. They were  $2W = 42$  mm away from each other and installed on a 2 mm thick aluminum plate. An eigenmode analysis of the resonator is performed as shown in Fig. 4.11(a). The deformation plot of a cross section of the

eigenmode at eigenfrequency ( $f_R$ ) of 124.0 kHz is shown in Fig. 4.11(a). The bottom surface of the resonator was kept fixed and the pillar part of the resonator acts as the spring and the top part of the resonator acts as the mass. Thus we measured the spring coefficient by exerting the force on the top surfaces of the pillar part of the resonator and observing the corresponding displacement as shown in Fig. 4.11(b). In a finite element analysis, the mass and stiffness of the resonator were estimated to be  $m = 31.4$  g and  $s = 19.0$  GN/m, yielding  $f_R = 124.0$  kHz.

Referring to Fig. 4.12,  $9.2 \text{ mm} \times 150 \text{ mm} \times 0.15 \text{ mm}$  magnetostrictive patch was installed on a 2 mm-thick aluminum plate. Sine pulses of 12 periods generated by a function generator (Agilent 33250A) were amplified (T&C Power Conversion AG1017L), then input to the MPT for wave generation. Another set of MPT patch was installed 1 m away from the transmitters for sensing. The signals from the sensor were amplified through a pre-amplifier (SR 560) and recorded using a digital oscilloscope (LeCroy Waverunner 104MXI). The measurements were performed using a pitch-catch mode. The measured peak-to-peak voltage value  $V_0$  was proportional to the strain rate  $-i\omega S_0$  measured by the MPT patch in the plate without the resonators installed. Thus,  $V_0 = \omega |C_1| |S_0|^2$  or  $|S_0| = \sqrt{V_0 / (\omega |C_1|)}$ , where  $C_1$  was a calibration constant. If we write  $|S_0^{\max}| = \max(|S_0|)$ , the

normalized value can be determined to be  $|S_0 / S_0^{\max}| = \omega^{\max} \sqrt{V_0} / [\omega \max(\sqrt{V_0})]$ .

The frequency of the maximum  $|S_0|$  was found to be 90 kHz in the experiment. If the measured peak-to-peak voltage in the plate with the installed resonators is denoted by  $V$ , it can also be expressed as  $V = \omega |C_1| |S_0| |S|$ , where  $S$  is the corresponding strain. Therefore, it is possible to obtain a relation such that

$|S / S_0^{\max}| = |\omega^{\max} V / (\omega \sqrt{V_0} \max(\sqrt{V_0}))|$ . The results are plotted in Fig. 4.13.

### 4.3 Realization of resonators for axisymmetric S0 Lamb wave and SH0 wave

The idea of wave resonance between a pair of resonators can be also adapted to axisymmetric waves. By revolving the cross-section of resonators respect to the axis, new resonators for axisymmetric waves are proposed, as shown in Fig. 4.14. In Fig. 4.14(a), a resonator geometry for S0 wave is shown, and that for SH0 wave is shown in Fig. 4.14(b). The geometry of cross-section of the resonators are same with that in section 4.1 and 4.2.

Simulations to demonstrate enhancement of the wave emission were performed, as shown in Fig. 4.15. The emitted S0 wave with and without resonator is plotted in Fig. 4.16(a), and emitted SH0 wave with and without resonator is plotted in Fig. 4.16(b).

As shown in Fig. 4.16, the resonators have the emission enhancing effect in axisymmetric  $S_0$  and  $SH_0$  waves. This implies that this idea also applicable with omnidirectional transducers.

#### **4.4 Summary**

In this chapter, it is found that the reduced effective impedance can be used for super enhancing of emission of transducers. Due to the similarity of  $S_0$  wave and  $SH_0$  wave in a plate with the waves in a one-dimensional beam, the plate waves are considered for the realization. To cope with the particle motion direction of the waves, the resonators are designed differently for each wave. The realized resonators enable the impedance to be reduced, yielding the transducer output to be enhanced at the Fabry–Pérot resonance frequency. From the experimental result, the effective impedance was retrieved, and that the value of effective impedance is successfully reduced is confirmed. It is shown that the transducer output enhancement can be used for various waves, including  $S_0$  and  $SH_0$  wave. Also it is shown that transducer output of both PZT and MPT can be enhanced, meaning that the transducer type is not relevant. Potentially output of any transducer can be enhanced with the theory.

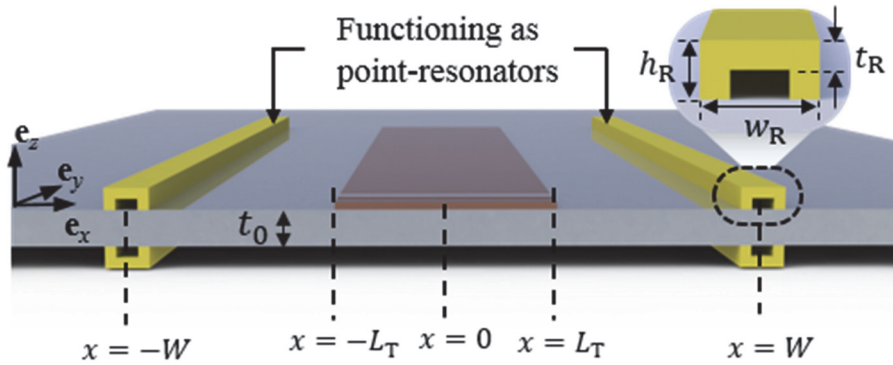


Figure 4.1 Sketch of thin plate with two resonators installed at  $x = \pm W$ . Each resonator at  $x = W$  or  $x = -W$  consists of two symmetrically configured C-shaped beams to ensure the generation of pure thickness-symmetric longitudinal waves without generating thickness-antisymmetric bending waves.

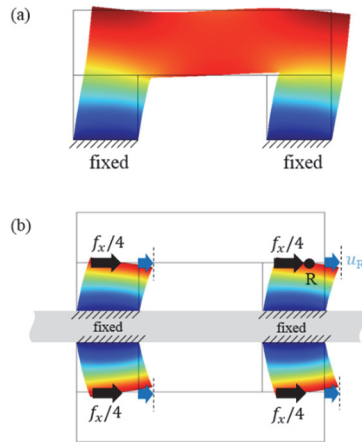


Figure 4.2 (a) Frontal view of lowest eigenmode of C-Shaped resonator and (b) deformed shape of pillars of C-shaped resonator under applied force  $f_x$  along  $x$  axis.

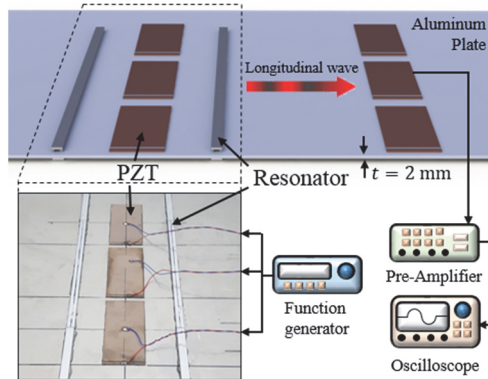


Figure 4.3 Setup for longitudinal wave experiments in thin plate. Three PZT patches were used to ensure the generation of a plane longitudinal wave mode in the plate.

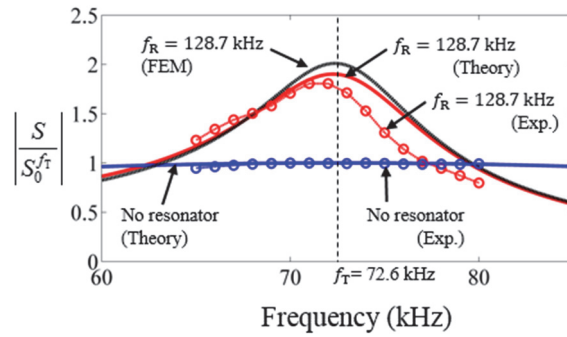


Figure 4.4 A comparison of the experimental and theoretical/numerical results for the radiated longitudinal strain field  $|S|$ .



Figure 4.5 Illustration of simulations of S0 wave transduction using T-shaped resonator.

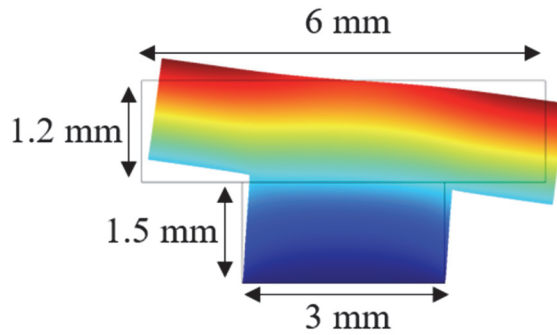


Figure 4.6 Dimension and eigenmode analysis of T-shaped resonator for S0 wave.

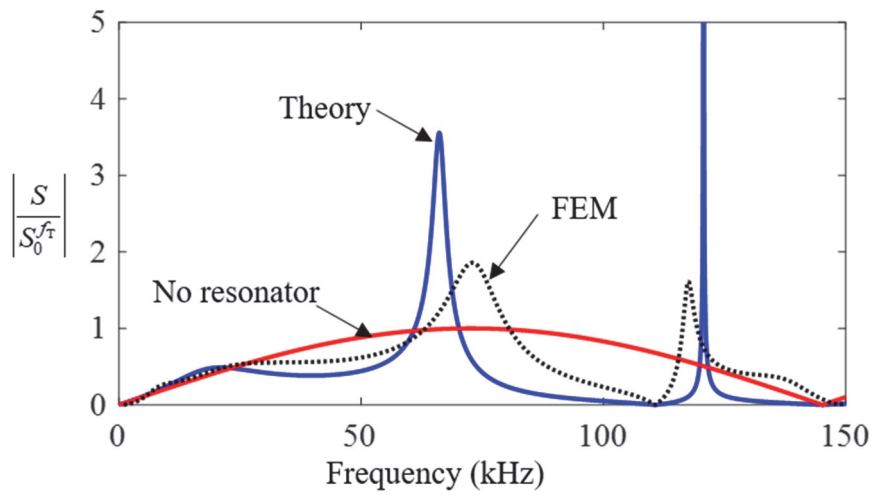


Figure 4.7 A comparison of the theoretical and numerical results for the radiated shear strain field  $|S|$ , using T-shaped resonators for S0 wave.

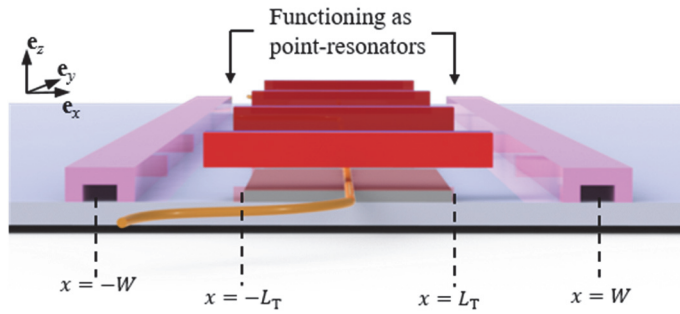


Figure 4.8 Sketch of thin plate with two C-shaped resonators installed at  $x = \pm W$  for SH0 wave transduction.

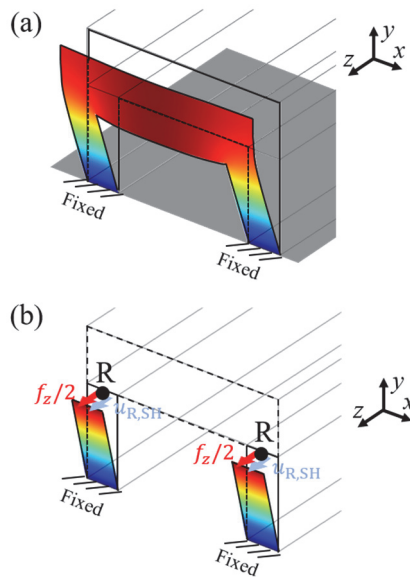


Figure 4.9 (a) Trimetric view of lowest eigenmode of C-Shaped resonator and (b) deformed shape of a pillar of C-shaped resonator under applied force  $f_z$  along  $z$  axis.

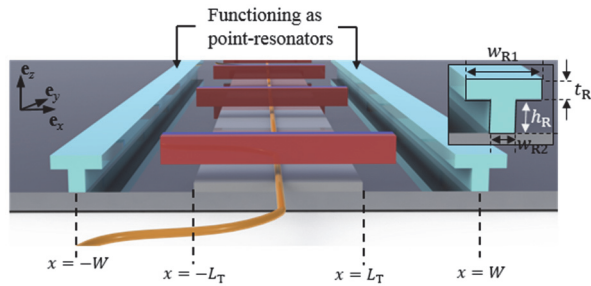


Figure 4.10 Sketch of thin plate with two T-shaped resonators installed at  $x = \pm W$  for SH0 wave transduction.

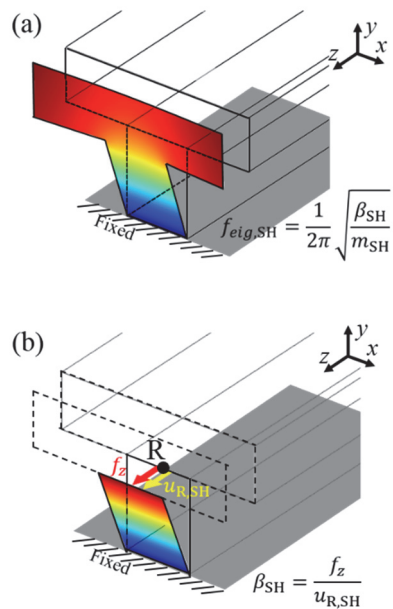


Figure 4.11 (a) Trimetric view of lowest eigenmode of T-Shaped resonator and (b) deformed shape of a pillar of T-shaped resonator under applied force  $f_z$  along  $z$  axis.

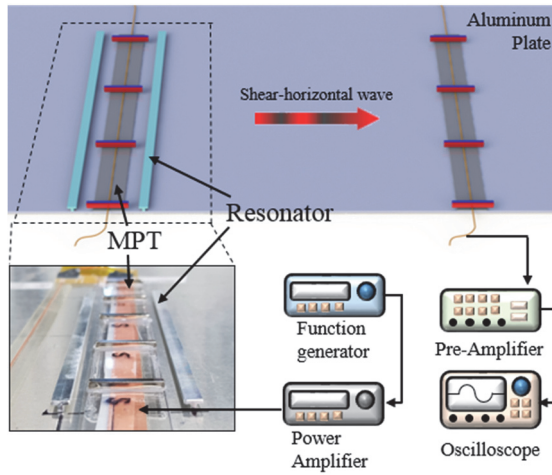


Figure 4.12 Setup for SH0 wave experiments in thin plate. A MPT was used to generate of a plane SH0 wave mode in the plate.

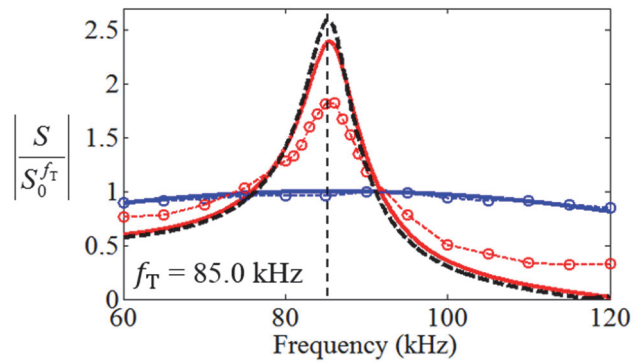


Figure 4.13 A comparison of the experimental and theoretical/numerical results for the radiated shear strain field  $|S|$ .

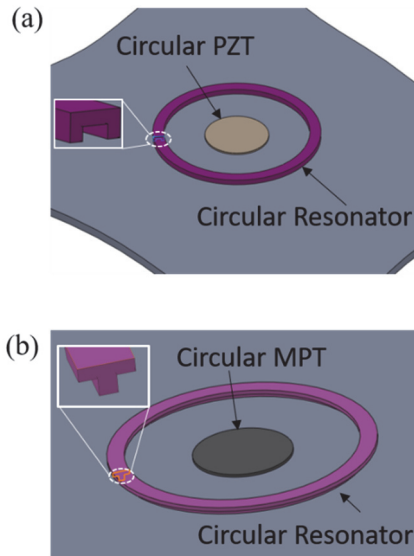


Figure 4.14 Illustrations of applications of resonators for (a) axisymmetric  $S_0$  wave and (b) axisymmetric  $SH_0$  wave.

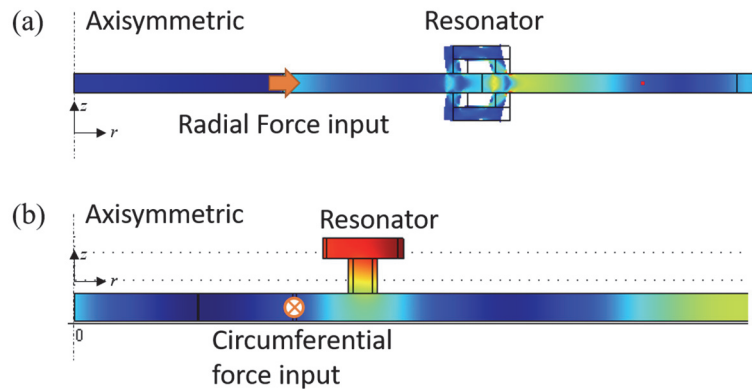


Figure 4.15 Illustrations of numerical simulations of wave transduction with resonators of (a) axisymmetric  $S_0$  wave and (b) axisymmetric  $SH_0$  wave.

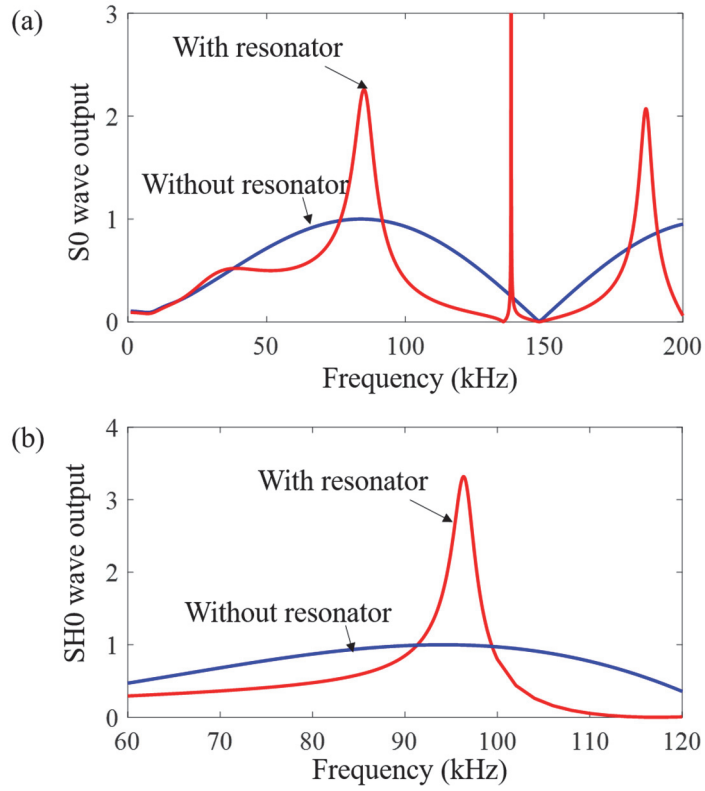


Figure 4.16 Plots of emitted (a) axisymmetric S0 wave and (b) axisymmetric SH0 wave with and without resonators.

# CHAPTER 5.

## RESONATOR PAIRING FOR ENHANCED SENSING

### 5.1 Resonator-paired waveguide system in receiving mode

In this section we show the spring-mass resonators have the same influence on the transduction efficiency on receiving mode. When the resonators are absent, the displacement field is  $u = Ie^{-ikx}$ . Since the transducers we use (PZT and MPT) measure the strain field of the test specimen, we may define the value that the sensor measure as the displacement difference at the edges of the transducer divided by the width of the transducer, as shown in Fig. 5.1(a) and equation (5.1).

$$M_0 = \frac{u_{x=L} - u_{x=-L}}{2L} = \frac{-i \sin kL}{L} I. \quad (5.1)$$

The maximum of  $M_0$  also occurs at frequency of  $f_T = c/4L$ , which is the same frequency with that of the transmitting mode

When the resonators are attached at  $x = \pm W$ , the incident wave  $I$  is scattered at where the resonators are located as shown in Fig. 5.1(b), thus we assume the displacement field as in equation (5.2).

$$u = \begin{cases} Ie^{-ikx} + Re^{ikx} & (x \leq -W) \\ u_4 e^{-ikx} + u_5 e^{ikx} & (-W \leq x \leq W) \\ Te^{-ikx} & (W \leq x) \end{cases} \quad (5.2)$$

The points  $Q$  and  $Q'$  are the point in the bar where the resonators are attached ( $x = W$  and  $x = -W$ , respectively), and continuity and force equilibrium at  $Q$  and  $Q'$  are expressed in equations (5.3-5.6). The displacement at  $Q$  and  $Q'$  are denoted by  $u_Q$  and  $u_{Q'}$ , respectively. The displacements of the resonator masses on  $x = \pm W$  are denoted by  $u_R$  and  $u_{R'}$ , respectively.

$$Ie^{ikW} + Re^{-ikW} = u_4 e^{ikW} + u_5 e^{-ikW} \triangleq u_{Q'}, \quad (5.3)$$

$$-iz_0 \omega (Ie^{ikW} - Re^{-ikW}) = s(u_{R'} - u_{Q'}) - iz_0 \omega (u_4 e^{ikW} - u_5 e^{-ikW}), \quad (5.4)$$

$$u_4 e^{-ikW} + u_5 e^{ikW} = Te^{-ikW} \triangleq u_Q, \quad (5.5)$$

$$-iz_0\omega(u_4e^{-ikW} - u_5e^{ikW}) = s(u_R - u_Q) - iz_0\omega T e^{-ikW}. \quad (5.6)$$

The equation of motion for the resonator masses are given by equations (5.7-5.8).

$$-m\omega^2 u_R + s(u_R - u_Q) = 0, \quad (5.7)$$

$$-m\omega^2 u_{R'} + s(u_{R'} - u_{Q'}) = 0. \quad (5.8)$$

Solving equations (5.3-5.8), it is able to find the displacement fields as expressed in Eqs. (5.9-5.12) with the definition of  $\alpha$  described in Eq. (5.13).

$$u_4 = \frac{4 + 2i\alpha}{(2 + i\alpha)^2 + \alpha^2 e^{-4ikW}} I, \quad (5.9)$$

$$u_5 = \frac{-2i\alpha e^{-2ikW}}{(2 + i\alpha)^2 + \alpha^2 e^{-4ikW}} I, \quad (5.10)$$

$$R = \frac{2i\alpha(\alpha \sin 2kW - 2 \cos 2kW)}{(2 + i\alpha)^2 + \alpha^2 e^{-4ikW}} I, \quad (5.11)$$

$$T = \frac{4}{(2 + i\alpha)^2 + \alpha^2 e^{-4ikW}} I, \quad (5.12)$$

$$\alpha = \frac{1}{z_0} \frac{m\omega s}{s - m\omega^2} = \frac{1}{z_0} \frac{\omega s}{\omega_R^2 - \omega^2}. \quad (5.13)$$

As the sensor measures the displacement difference,  $M = (u_{x=L} - u_{x=-L})/2L$ , the sensor measurement is expressed in equation (5.14).

$$M = \frac{(u_4 e^{-ikL} + u_5 e^{ikL}) - (u_4 e^{ikL} + u_5 e^{-ikL})}{2L} = -\frac{2 \sin kL}{L} \frac{1}{\alpha(1 - e^{-2ikW}) - \hat{z}} \quad (5.14)$$

If we normalize  $M$  with the nominal sensor measurement,  $M_0^{f_T}$ , the solution  $M/M_0^{f_T}$  is expressed in Eq. (5.15) and it is exactly identical with that of transmitter output strain,  $S/S_0^{f_T}$ , which confirms the reciprocity of the transducer system.

$$\frac{M}{M_0^{f_T}} = \frac{-2i \sin kL}{\alpha(1 - e^{-2ikW}) - 2i} = \frac{S}{S_0^{f_T}}. \quad (5.16)$$

## 5.2 Realization and experimental results for S0 and SH0 wave

We also performed experiments for receiving modes with the C-channel resonators for PZTs receiving S0 wave and T-shaped beams for MPTs receiving SH0 wave. The same resonators used for transmitting mode were used. The experimental setup for the sensor is the same with that with the transmitting mode. Before attaching the resonators, signals  $V_0$  were received with the sensors without the resonators to determine the nominal characteristic of the PZTs,  $M_0$ . The peak to peak value of the raw signal  $V_0^{\text{PTP}}$  is affected by both sensor and transmitter characteristics. In this case, the transmitter characteristic  $C_2 M_0$  is reciprocal with the sensor

characteristic, where  $C_2$  is a constant. Then,  $V_0^{\text{PTP}}$  can be expressed as equation (5.32), and the relation between the maximum value of  $M_0$  and the peak to peak value of the signal is expressed in equation (5.33).

$$V_0^{\text{PTP}} = |C_2 M_0^2|, \quad (5.32)$$

$$|M_0^{\text{max}}| = \frac{\max(\sqrt{V_0^{\text{PTP}}})}{\sqrt{|C_2|}}. \quad (5.33)$$

Then the resonators are bonded with epoxy resin near the sensor and the signals from the sensor with the resonator were measured. With the same transducer output  $C_2 M_0$ , the sensor measures the signal  $V$  with the characteristic of the sensor with the resonators  $M$ , and the relation among them are expressed as:

$$V^{\text{PTP}} = |C_2 M_0| |M|. \quad (5.34)$$

Combining equations (5.32-5.33) into equation (5.34),  $|M/M_0^{\text{max}}|$  can be determined as:

$$\left| \frac{M}{M_0^{\text{max}}} \right| = \frac{1}{\max(\sqrt{V_0^{\text{PTP}}})} \frac{V^{\text{PTP}}}{\sqrt{V_0^{\text{PTP}}}}. \quad (5.35)$$

The magnitude of the sensor measurement  $\left| M/M_0^{f_T} \right|$  with the realized model are plotted in Fig. 5.2(a) for S0 wave case and Fig. 5.2(b) for SH0 wave case.

### 5.3 Equivalent system of the paired resonator system in receiving mode

The wave system in Fig. 5.1(b) can be also explained as the same effective medium system (Fig. 5.1(c)) with impedance  $z$  and length  $2W'$  as readily described in Chapter 3, with the wave solutions as in Eq. (5.17).

$$\tilde{u} = \begin{cases} \tilde{I}e^{-ikx} + \tilde{R}e^{ikx} & (x \leq -W') \\ \tilde{u}_4e^{-ikx} + \tilde{u}_5e^{ikx} & (-W' \leq x \leq W') \\ \tilde{T}e^{-ikx} & (W' \leq x) \end{cases}. \quad (5.17)$$

We used the same variable scaling  $g(\omega)$  as in Chapter 3 as expressed in equation (5.18-5.19). Together, the reflection  $\tilde{R}$  and transmission  $\tilde{T}$  of the effective medium are set to be the same with those in the original system with the resonators ( $R$  and  $T$ ), as expressed in equations (5.20-5.21).

$$\frac{\tilde{u}_4}{u_4} = \frac{\tilde{u}_5}{u_5} = g(\omega), \quad (5.18)$$

$$g(\omega) = \sqrt{\frac{z_0}{z}} e^{i(\beta + p\pi/2)}, \quad (p = \text{sign}(\omega - \omega_R)), \quad (5.19)$$

$$\tilde{R} = R, \quad (5.20)$$

$$\tilde{T} = T. \quad (5.21)$$

In the equivalent homogenized model, the continuity and force equilibrium condition at  $x = -W'$  and  $x = W'$  have to be satisfied, as expressed in equations (5.22-5.25).

$$\tilde{I}e^{ikW'} + \tilde{R}e^{-ikW'} = \tilde{u}_4e^{ikW'} + \tilde{u}_5e^{-ikW'}, \quad (5.22)$$

$$-iz_0\omega(\tilde{I}e^{ikW'} - \tilde{R}e^{-ikW'}) = -iz_0\omega(\tilde{u}_4e^{ikW'} - \tilde{u}_5e^{-ikW'}), \quad (5.23)$$

$$\tilde{u}_4e^{-ikW'} + \tilde{u}_5e^{ikW'} = \tilde{T}e^{-ikW'}, \quad (5.24)$$

$$-iz_0\omega(\tilde{u}_4e^{-ikW'} - \tilde{u}_5e^{ikW'}) = -iz_0\omega\tilde{T}e^{-ikW'}. \quad (5.25)$$

The only needed condition to satisfy equations (5.22-5.25) is a phase compensation to the incident wave, as expressed in equation (5.26).

$$\frac{\tilde{I}}{I} = -e^{-4ik(W'-W)}. \quad (5.26)$$

With the variables in the effective medium,  $\tilde{u}_4$  and  $\tilde{u}_5$ , in equation (5.18) the relation between sensor measurement in the effective medium and that in the original system is expressed in equation (5.27).

$$\tilde{M} = \frac{(\tilde{u}_4 e^{-ikL} + \tilde{u}_5 e^{ikL}) - (\tilde{u}_4 e^{ikL} + \tilde{u}_5 e^{-ikL})}{2L} = g(\omega)M . \quad (5.27)$$

Solving the equations (5.22-5.25) with the terms of effective impedance  $z$  and the medium length  $2W'$ , the displacement fields and sensor measurement are described with respect to the effective properties as shown in equations (5.28-5.30).

$$\tilde{u}_4 = \frac{2z_0(z_0 + z)e^{-2ikW'}}{-(z - z_0)^2 e^{-2ikW'} + (z + z_0)^2 e^{2ikW'}} \tilde{I} , \quad (5.28)$$

$$\tilde{u}_5 = \frac{2z_0(z - z_0)}{-(z - z_0)^2 e^{-2ikW'} + (z + z_0)^2 e^{2ikW'}} \tilde{I} , \quad (5.29)$$

$$\tilde{M} = \frac{-i \sin kL}{L} \frac{z_0 e^{ikW'}}{z \cos kW' + iz_0 \sin kW'} \tilde{I} . \quad (5.30)$$

The equations (5.28-5.29) show that the waves inside the effective medium are amplified due to the reduced impedance at Fabry-Perot resonance conditions, both  $\sin kW' = 0$  and  $\cos kW' = 0$ . At  $\sin kW' = 0$ ,  $\tilde{u}_4$  becomes  $(z_0 + z)/(2z)$  and  $\tilde{u}_5$  becomes  $(z_0 - z)/(2z)$ , which both are increased with reduced impedance. At one of the Fabry-Perot resonances,  $\sin kW' = 0$ , the waves inside the center medium form antisymmetric modes while they form symmetric modes at the other Fabry-Perot resonances,  $\cos kW' = 0$ . However, because that our transducer is more susceptible to the waves which their mode shapes are

antisymmetric to the origin,  $|\tilde{M}|$  is increased only at  $\sin kW' = 0$ .

Using equations (5.27) and (5.30), the sensor measurement  $|M/M_0^{f_T}|$  can be expressed explicitly with terms of effective impedance, as in equation (5.31).

$$\left| \frac{M}{M_0^{f_T}} \right| = \frac{\sqrt{zz_0} \sin kL}{\sqrt{z^2 \cos^2 kW' + z_0^2 \sin^2 kW'}}. \quad (5.31)$$

The measurement is increased by  $\sqrt{z_0/z}$  at the Fabry-Perot resonance,  $\sin kW' = 0$ . The enhancing phenomenon is the same with the transmitting mode.

#### 5.4 Summary

In this chapter, it is shown that the near-zero impedance concept is useful to increase the sensitivity of transducers. Using theoretical analysis, the sensitivity in receiving mode is shown to be reciprocal to the results in transmitting mode. The resonator pair effectively reduces the impedance of the medium surrounded by them, yielding the confinement of wave inside the cavity. Therefore, the wave in the medium surrounded by the resonators is amplified, resulting in the increase of received signals. It is verified with realized resonators and experimental results for S0 and SH0 waves.

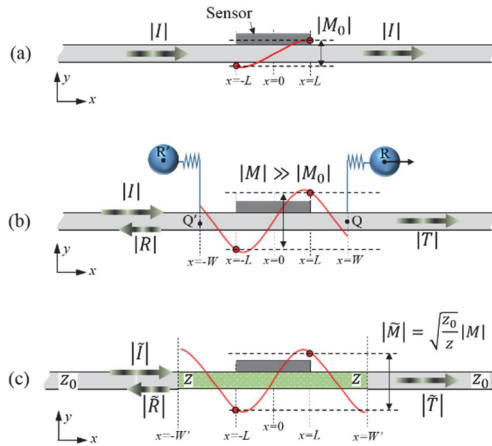


Figure 5.1 Schematic of wave status in receiving mode. Sensor measurement in (a) nominal case and (b) resonator case with an incident wave  $I$ . (c) Equivalent system using effective medium of sensing in resonator case as shown in (b).

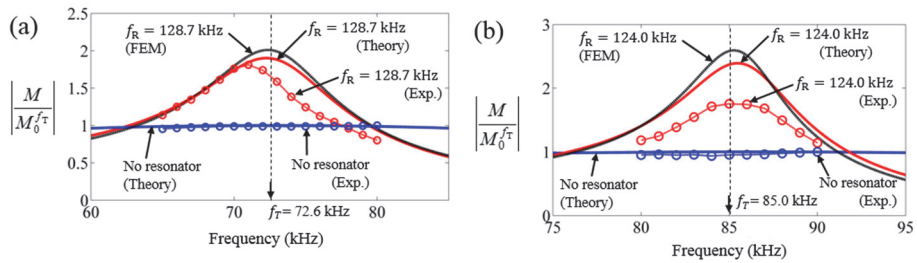


Figure 5.2 A comparison of the experimental and theoretical/numerical results for the measured (a) longitudinal strain of S0 wave and (b) shear strain of SH0 wave.

# **CHAPTER 6.**

## **ANALYSIS OF EMISSION IN BENDING WAVE SYSTEM**

The theory described in Chapter 3 is based on one-dimensional wave in a beam, and the realizations in Chapter 4 are based on the in-plane waves in a plate. The theory was applicable without modification since the in-plane waves in a plate are almost identical to the wave in a one-dimensional beam. However, the counterpart of shear-vertical wave in the beam, bending waves in the plate have more complicated physics than those of in-plane waves. Therefore, the resonator pairing in bending wave is needed to be analyzed with compatible beam theory, Timoshenko beam theory.

As guided waves are used more widely in recent years for nondestructive ultrasonic evaluation of plates and pipes (see, e.g., [19, 25, 62]), the performance improvement of transducers becomes more important. Among various transducers, this study is

concerned with MPT as studied earlier in [15, 22, 63-67] and focused on the increase of its transduction efficiency of A0 wave. The MPT consists of a thin magnetostrictive patch directly bonded onto a test waveguide or specimen, a set of magnets and electric coil. The specific MPT configuration to be considered in this study is illustrated in Fig. 6.1, which is used to generate the Lamb waves in a test plate along the  $x$  direction. It operates on the magnetostrictive principle dictating the coupling between magnetic and mechanical fields (see, e.g., [17, 68]. As in most transducers such as piezoelectric transducers and MPTs, the underlying design principle to maximize transducer output is to make a use of internal resonance or wavelength matching. In case of MPTs, the principle requires that the size of the magnetostrictive patch that is coupled with a test specimen should match with the wavelength of the wave excited in a test specimen at an excitation frequency [22-24]. As MPTs operate on the magnetostrictive principle, one may also consider optimizing the magnetic circuit to increase the transducer output [64, 69].

The above-mentioned methods are related to the optimal design of the transducer itself and if the power of the transducer is to be further increased, an unprecedented method may need to be considered. Especially when an MPT is to be used to generate anti-symmetric Lamb waves such as the A0 mode wave, an additional power-boosting method is certainly needed. The reason is that the magnetostrictive patch of an MPT induces in-plane deformation of the test plate surface bonded to it (as

sketched in Fig. 6.2), anti-symmetric Lamb waves such as the A0 mode wave are more difficult to generate than symmetric Lamb waves or shear-horizontal waves such as the S0 and SH0 mode wave [23, 51, 70, 71]. If an MPT can efficiently excite the vertical force (in the  $y$  direction in Fig. 6.3(b)) or the bending moment (about the  $z$  direction), anti-symmetric Lamb waves would be more efficiently excited. However, there is no such mechanism currently available in MPTs.

Our proposition to boost the transduction efficiency of an MPT for the generation of anti-symmetric modes, specifically, the lowest A0 mode, is to introduce an auxiliary add-on component, the U-shaped resonator as sketched in Fig. 6.3(a). As sketched in Fig. 6.3(b), the boosting resonator induces bending vibration, which results in the transfer of the vertical force and bending moment to the plate. Thereby, the antisymmetric A0 mode is excited more efficiently. The inspiration behind considering the additional resonator is that a dynamic absorber based on a mechanical resonator absorbs vibration energy at a tuned frequency [58, 72-74], but it actually amplifies it near the tuned frequency [54]. Accordingly, we consider a non-stereotype approach to use the energy-absorbing resonator as a power-boosting resonator operating at a detuned frequency.

Note that the auxiliary U-shaped resonator is an add-on type passive element. However, it can be integrated into an existing MPT because it will be placed on the

magnetostrictive patch. In the subsequent sections, we will reveal the transduction efficiency enhancing mechanism of the U-shaped resonator theoretically. For the analysis, the coupled MPT-resonator system is analytically modeled by the Timoshenko beam theory [34]. The predicted result by the present theoretical analysis is confirmed by the finite element simulation and the experimental result.

## 6.1 Analytic model

As this work is mainly concerned with the transduction efficiency for the generation of the A0 wave mode, we introduce a simplified model for the MPT's mechanism (in Fig. 6.4) to generate the mode. As illustrated in Fig. 6.2, input strain is induced in the magnetostrictive patch, and the magnetostrictive patch of the MPT can be regarded to exert two concentrated in-plane forces [52] on the top surface of the plate. Therefore, it can be replaced by two concentrated forces applied on the middle plane of the plate and two concentrated moments about the  $z$  axis. The directions of the concentrated moments are also indicated in Fig. 6.4(a). As this study is focused on the anti-symmetric A0 wave mode, the two concentrated moments will be considered as the driving agents since the concentrated in-plane forces applied on the middle plane are mostly related with the symmetric mode. As our subsequent analysis utilizes this model, the validity of this simplified model for A0 mode generation should be checked first. To this end, we compared the frequency characteristics for

the A0 mode obtained by the simplified excitation model in Fig. 6.4(a) and a detailed model.

For the detailed transduction model, a strain field induced by an applied magnetic field in the magnetostrictive patch is calculated by the piezomagnetic constitutive relation [75] and prescribed as an excitation source to the patch. Then, we find the strain field on the top surface of the plate at a selected measurement point, located at some distance away from the MPT installation location as shown in Fig. 6.4(a). The normalized ratio of the measured strain to the prescribed strain at the patch is used as the transducer output of original model. In case of the simplified transduction model, the two concentrated moments depicted in Fig. 6.4(a) are assumed to excite the A0 mode in the plate. Since the distance between the centers of the supporting beams in U-resonator is 9 mm, we chose the distance between the input moments,  $2L = 9$  mm so that the input moments to be well coupled with the resonator. The transducer output in the simplified model is defined as the normalized ratio of the measured strain to the input moment. Fig. 6.4 (b) shows the frequency characteristics of the transducer outputs (for the A0 wave mode) obtained by the detailed and simplified transduction models. The peak frequency  $f_T = 64.0$  kHz of the detailed model corresponds to the wavelength of the A0 mode in the plate, 16.75 mm. The slight difference between the wavelength and double of the distance between the input moments,  $4L = 18$  mm may cause some disagreement in the frequency

characteristics. However, Fig. 6.4(b) shows that the simplified transduction model predicts the frequency behavior of the transducer over a wide range of frequencies although there is slight frequency shift in the peak response. As the MPT typically operates near the peak frequency, we aim to increase the transducer output at  $f_T$  using the add-on type U-shaped resonator (dimensions shown in Fig. 6.5(a)). The thickness of the center beam,  $t_1$ , is 1.8, 2.4 and 3 mm for case 1, 2 and 3, respectively. The U-shaped resonator added on the actuation mechanism which is modeled with two concentrated moments is considered as shown in Fig. 6.5(b) to conduct further analyses.

To reveal the working mechanism of the add-on type U-shaped resonator, a theoretical model will be developed. To facilitate the analysis, a plane A0 wave extending infinitely (or sufficiently long) along the  $z$  direction is assumed. More importantly, the plane A0 wave propagating in the plate with the attached resonator will be modeled by a flexural wave in a beam to which the resonator is attached to. The resonator will be modeled by two generalized spring elements supporting a lumped mass of  $2m$ , as sketched in Fig. 6.6(a). As shown in Fig. 6.6(b), the generalized spring is considered as a relation between the relative displacements (including the rotation) of points P and R, and the forces (including the moment about  $z$ -axis) exerted on P, as expressed in equation (6.1).

$$\begin{pmatrix} S_{11} & S_{12} & S_{13} \\ S_{21} & S_{22} & S_{23} \\ S_{31} & S_{32} & S_{33} \end{pmatrix} \begin{pmatrix} u_P \\ v_P - v_R \\ \theta \end{pmatrix} = \begin{pmatrix} f_x \\ f_y \\ m_z \end{pmatrix}. \quad (6.1)$$

In equation (6.1),  $u_P$ ,  $v_P$ ,  $v_R$  and  $\theta$  are the horizontal and vertical displacement of point P, and the vertical displacement of point R and the rotation angle of point P shown in Fig. 6.6(b), respectively.  $f_x$ ,  $f_y$  and  $m_z$  are the exerted horizontal and vertical forces and moment about z-axis per unit length in z direction on point P, respectively. To determine the exact parameters of the generalized spring matrix, a numerical simulation (using COMSOL [61]) is conducted with following the procedure described in reference [2]. With an assumption of symmetry, only the half part of the resonator is considered, and the center line including point R is in roller supported condition. Then horizontal, vertical forces and moment are exerted independently on point P, and the resultant displacements and rotation of point P are measured to determine the spring matrix.

Before finding out the mass coefficient of the resonator, an eigenfrequency analysis (using COMSOL [61]) is conducted to determine the dominant motion of the U-shaped resonator. The results are shown in Fig. 6.7. For the resonator case 1 which the thickness of the center beam is 1.8 mm as shown in Fig. 6.7(a), the first three eigenmodes and corresponding eigenfrequencies are depicted in Fig. 6.7(b). Since the transducer driving condition is symmetrical to the center of the resonator, the

dominant motion of the resonator should be symmetric. Moreover, because that the frequency domain of our interest is near the frequency where the maximum output occurred in Fig. 6.4(b) ( $f_T = 64$  kHz), the vertical motion of the resonator as shown in the second mode,  $f_{\text{eig}2} = 63.2$  kHz, in Fig. 6.7(b) should be considered as the dominant motion of the U-shaped resonator in this study. The motion of the second eigenmode implies that the mass only moves vertically and the rotational and horizontal inertia can be neglected by the symmetric motion, and the vertical momentum is mainly responsible for the resonance. Symmetric geometry and motion behavior of the U-shaped resonator make possible to assume the rotational and horizontal inertia to be neglected. Therefore, as shown in Fig. 6.7(c), the relation between eigenfrequency ( $f_{\text{eig}2}$ ), and vertical stiffness ( $S_{22}$ ) is used to determine the inertia coefficient ( $m$ ) as expressed in equation (2):

$$m = \frac{S_{22}^2}{2\pi f_{\text{eig}2}}. \quad (6.2)$$

The measured spring and mass coefficients are listed in table 6.2 with the material properties listed in table 6.1 for the resonator cases 1, 2 and 3. The resonators are assumed to be made of glass to make sure the resonators do not disturb the surrounding electromagnetic fields, since metallic components may disturb the fields [64].

As shown in Fig. 6.8, the plate is divided into three sections based on the point where the forces between the resonators and plate interact. To conduct a theoretical analysis, the plate is assumed as a Timoshenko beam having the elastic properties of aluminum (listed in table 6.1) with thickness of 2 mm as sketched in Fig. 6.8. The leftmost and rightmost sections are identical by the symmetry, so they are named as section B while the center section is named as section A. In section A, there should be waves of both propagating and decaying mode, with the leftward and rightward waves being symmetrical. On the other hand, there are only outward waves of both propagating and decaying mode in section B. We used wave equations in Timoshenko beam theory to solve analytically, as expressed as equation (6.3) and (6.4):

$$GA \left( \frac{\partial^2 v}{\partial x^2} - \frac{\partial^2 \varphi}{\partial x^2} \right) = \rho A \frac{\partial^2 v}{\partial t^2}, \quad (6.3)$$

$$EI \frac{\partial^2 \varphi}{\partial x^2} + GA \left( \frac{\partial v}{\partial x} - \varphi \right) = \rho I \frac{\partial^2 \varphi}{\partial t^2}. \quad (6.4)$$

The variables  $v$  and  $\varphi$  denote the vertical displacement and the rotation of the normal plane of the beam, respectively.  $G$ ,  $A$ ,  $\rho$ ,  $E$  and  $I$  denote shear modulus, area of cross-section of the beam, density, Young's modulus and moment of inertia respectively. Solving the equation (6.3) and (6.4), the wave solutions in

sections A and B as illustrated in Fig. 6.8 are expressed as equation (6.5) and (6.6).

$$v = v_1 e^{-i(k_1 x - \omega t)} + v_2 e^{-i(k_2 x - \omega t)} + v_1 e^{i(k_1 x + \omega t)} + v_2 e^{i(k_2 x + \omega t)}, (|x| \leq L), \quad (6.5)$$

$$v = v_3 e^{-i(k_1 x - \omega t)} + v_4 e^{-i(k_2 x - \omega t)}, (|x| \geq L),$$

$$\varphi = \alpha_1 v_1 e^{-i(k_1 x - \omega t)} + \alpha_2 v_2 e^{-i(k_2 x - \omega t)} - \alpha_1 v_3 e^{i(k_1 x + \omega t)} - \alpha_2 v_4 e^{i(k_2 x + \omega t)}, \quad (|x| \leq L), \quad (6.6)$$

$$\varphi = \alpha_1 v_3 e^{-i(k_1 x - \omega t)} + \alpha_2 v_4 e^{-i(k_2 x - \omega t)}, (|x| \geq L),$$

$$\alpha_j = -i \frac{k_j^2 - \rho \omega^2 / G}{k_j}, \quad j = 1, 2. \quad (6.7)$$

$\omega$  and  $t$  denote angular frequency and time, respectively.  $k_1$  and  $k_2$  denote the wavenumbers of 1<sup>st</sup> and 2<sup>nd</sup> mode in the Timoshenko beam, expressed as following equation (6.8) and (6.9):

$$k_1 = \left\{ \frac{1}{2} \left[ \left( \frac{1}{c_s} \right)^2 + \left( \frac{1}{c_b} \right)^2 \right] \omega^2 + \sqrt{\left( \frac{\omega}{c_b q} \right)^2 + \frac{1}{4} \left[ \left( \frac{1}{c_s} \right)^2 - \left( \frac{1}{c_b} \right)^2 \right]^2 \omega^4} \right\}^{\frac{1}{2}} \quad (6.8)$$

$$k_2 = - \left\{ \frac{1}{2} \left[ \left( \frac{1}{c_s} \right)^2 + \left( \frac{1}{c_b} \right)^2 \right] \omega^2 - \sqrt{\left( \frac{\omega}{c_b q} \right)^2 + \frac{1}{4} \left[ \left( \frac{1}{c_s} \right)^2 - \left( \frac{1}{c_b} \right)^2 \right]^2} \omega^4 \right\}^{1/2} \quad (6.9)$$

In equation (6.8) and (6.9),  $c_b$  and  $c_s$  are the bar ( $\sqrt{E/\rho}$ ) and shear velocities ( $\sqrt{G/\rho}$ ) and  $q$  is the radius of gyration of the cross section of the beam. Assuming that the plate is very long in the  $z$  direction, the radius of gyration can be expressed as  $\sqrt{3}h/6$ , where  $h$  is the thickness of the plate, 2 mm. The wavenumber of 2<sup>nd</sup> mode,  $k_2$ , is purely imaginary under the cutoff frequency, 861 kHz. Therefore, the 2<sup>nd</sup> mode is assumed as the decaying mode in this study since the frequency range of interest is under 200 kHz.

At the boundary between the section A and B, the resonator and beam interacts mutually via forces and moments. In other words, point P and Q in Fig. 6.8 exchanges forces and moments, and the force equilibriums are expressed as equation (6.10) ~ (6.12):

$$F_x = -f_x \quad (6.10)$$

$$F_y = -f_y \quad (6.11)$$

$$M_z = -m_z \quad (6.12)$$

The vertical force,  $f_y$ , is delivered to the mass of the resonator through the generalized spring. The equation of motion of the resonator is expressed as equation (6.13):

$$f_y = m\ddot{v}_R = -\omega^2 m v_R \quad (6.13)$$

Considering the basic boundary conditions at the interface between the sections, equations (6.14) ~ (6.17) can be written as following:

$$v_{x=L^-} = v_{x=L^+} \quad (6.14)$$

$$\varphi_{x=L^-} = \varphi_{x=L^+} \quad (6.15)$$

$$V_{x=L^-} - F_y = V_{x=L^+} \quad (6.16)$$

$$M_{x=L^-} - M_{inp} - M_z + \frac{h}{2} F_x = M_{x=L^+} \quad (6.17)$$

The vertical force from the resonator ( $F_y$ ) affects the shear force equilibrium in equation (6.16). The input moment ( $M_{inp}$ ), moment from the resonator ( $M_z$ ) and moment from the surface horizontal force ( $-hF_x/2$ ) is considered in moment equilibrium in equation (6.17). The shear force ( $V$ ) and moment ( $M$ ) are described by the constitutive equations in equation (6.18) and (6.19).

$$V = GA \left( \frac{\partial v}{\partial x} - \varphi \right) \quad (6.18)$$

$$M = EI \left( \frac{\partial \varphi}{\partial x} \right) \quad (6.19)$$

For the detailed kinematics on point P and Q as shown in Fig. 6.9, the displacement fields of the point P can be described as equations (6.20) ~ (6.22). The vertical displacements of point P and Q are identical. Horizontal displacement in point P corresponds with the displacement by the normal plane rotation of the beam at point Q. For the rotation  $\theta$ , the average of the beam slope in section A and B is assumed.

$$u_P = -\frac{h}{2} \varphi_{x=L} \quad (6.20)$$

$$v_P = v_Q = v_{x=L} \quad (6.21)$$

$$\theta = \frac{1}{2} \left( \left. \frac{\partial v}{\partial x} \right|_{x=L^-} + \left. \frac{\partial v}{\partial x} \right|_{x=L^+} \right) \quad (6.22)$$

Therefore, all terms in equations (6.13) ~ (6.17) ( $v$ ,  $\varphi$ ,  $V$ ,  $M$ ,  $F_x$ ,  $F_y$ , and  $M_z$ ) can be rewritten with the wave solution variables ( $v_1, v_2, v_3$  and  $v_4$ ) and the displacement of the resonator ( $v_R$ ) respect to the unit input moment term ( $M_{\text{inp}}$ ).

Combining all relevant equations and omitting the time-harmonic term  $e^{i\omega t}$ , equation (6.23) ~ (6.27) are derived from equation (6.13) ~ (6.17).

$$\omega^2 m v_R - F_y = 0 \quad (6.23)$$

$$v_1(e^{-ik_1L} + e^{ik_1L}) + v_2(e^{-ik_2L} + e^{ik_2L}) = v_3e^{-ik_1L} + v_4e^{-ik_2L} \quad (6.24)$$

$$\alpha_1 v_1(e^{-ik_1L} - e^{ik_1L}) + \alpha_2 v_2(e^{-ik_2L} - e^{ik_2L}) = \alpha_1 v_3e^{-ik_1L} + \alpha_2 v_4e^{-ik_2L} \quad (6.25)$$

$$k_1 v_1(e^{-ik_1L} - e^{ik_1L}) + k_2 v_2(e^{-ik_2L} - e^{ik_2L}) + \frac{1}{iGA} F_y = k_1 v_3e^{-ik_1L} + k_2 v_4e^{-ik_2L} \quad (6.26)$$

$$\alpha_1 k_1 v_1(e^{-ik_1L} + e^{ik_1L}) + \alpha_2 k_2 v_2(e^{-ik_2L} + e^{ik_2L}) + \frac{1}{iEI} \left( M_{inp} + M_z - \frac{h}{2} F_x \right) = \alpha_1 k_1 v_3e^{-ik_1L} + \alpha_2 k_2 v_4e^{-ik_2L} \quad (6.27)$$

$$\begin{pmatrix} F_x \\ F_y \\ M_z \end{pmatrix} = - \begin{pmatrix} S_{11} & S_{12} & S_{13} \\ S_{21} & S_{22} & S_{23} \\ S_{31} & S_{32} & S_{33} \end{pmatrix} \begin{pmatrix} -h(\alpha_1 v_3 e^{-ik_1L} + \alpha_2 v_4 e^{-ik_2L}) / 2 \\ v_3 e^{-ik_1L} + v_4 e^{-ik_2L} - v_R \\ -k_1 v_1 \sin(k_1 L) - k_2 v_2 \sin(k_2 L) - i k_1 v_3 e^{-ik_1L} / 2 - i k_2 v_4 e^{-ik_2L} / 2 \end{pmatrix} \quad (6.28)$$

Equation (6.28) shows the forces and moment terms which are inserted in equation (6.23) ~ (6.27), expressed explicitly in terms of  $v_1, v_2, v_3, v_4$  and  $v_R$ . Equations (6.23) ~ (6.27) are 5 equations composed of 5 variables, so the wave magnitudes including the A0 wave output,  $v_3$ , in Fig. 6.8 are solved.

Since the physical meaning of  $v_3$  is the displacement of the output propagating wave field, the magnitude of the output surface strain field ( $|\varepsilon_x|$ ) are plotted as the frequency characteristics in Fig. 6.10 to be in consistency with previous section. The magnitude of the output surface strain field is derived as equation (6.29).

$$|\varepsilon_x| = \left| \frac{\partial u}{\partial x} \right|_{y=h/2} = \left| \frac{h}{2} \alpha_1 k_1 v_3 \right| \quad (6.29)$$

## 6.2 Experiments

Next, we compare the theoretically solved results with the results of numerical simulation. Harmonic analyses using COMSOL [61] with the same configurations considered in the theoretical analyses are conducted to simulate the wave field. With the assumption of 2D plane strain, configuration in Fig. 6.5(b) is considered and the following results are also plotted in Fig. 6.10. As shown in Fig. 6.10, theoretical and numerical analyses agree well with each other in all cases. In all cases, the transducer outputs are certainly increased in a frequency band. As the case number is increased the peak frequencies tends to shift higher, peak values tend to descend, and the bandwidth of the increased output tend to be broaden. As the center beam of the U-shaped resonator ( $t_1$ ) is thickened, both the spring and mass constants are increased as in table 6.2. However, the mass coefficient is proportional to the thickness of the center beam whereas the bending stiffness of the beam should be proportional to the

cube of the thickness, therefore the resonant frequency should be shifted higher, which can be also observed in eigenfrequencies in table 6.2. Thus, the overall resonant frequency of the system should be shifted higher. By tuning the thickness of the center beam of the resonator, the peak frequency is adjustable for the user's desire. Simultaneously, the peak of the increased output tends to slightly decrease as the case number is increased. This is because the resonance frequency tends to shift away from the original transducer peak frequency, the mismatch between the transducer internal resonance frequency ( $f_T$ ) and the resonance frequency ( $f_{\text{eig}2}$ ) decreases the maximum output peak. As shown in Fig. 6.10, the frequency bandwidth of the increased output tends to be broaden as the thickness of the center beam of the resonator is thickened.

Samples of the resonators are manufactured and experiments are conducted to verify the enhancements of transducer outputs, and the experimental setup is shown in Fig. 6.11. The magnetostrictive patch is 10 mm wide in x-direction, 0.15 mm thick in y-direction, and 100 mm long in z-direction. A pair of MPTs without a resonator is installed on an aluminum plate with distance of 600 mm from each other in x-direction. A sine pulse of 15 periods is input to one of the transducers, and the signal is measured from the other transducer. With varying frequencies of the input pulse, we measured the frequency characteristics of the MPT without a resonator. Right after measuring the signals from the MPT without a resonator, a U-shaped resonator

having length of 90 mm in  $z$ -direction is bonded onto the magnetostrictive patch of the transmitter with epoxy resin. Again, the signals from the transducer with the resonator are measured with the same sensor used in earlier measurements to directly compare the magnitude of the output signals. For the MPT with the resonator, frequency characteristics is measured with varying the frequency of input pulse. Same experimental procedure is repeated with other cases of resonators with a new set of MPTs.

The frequency sweep results from the transmitters with and without resonators are plotted in Figs. 6.12 ~ 6.14. The figures contain the frequency characteristics calculated by both numerical analyses and experiments. Frequency characteristics based on the magnitudes of the normal strain on the magnetostrictive patches are plotted for resonator cases 1, 2, and 3 in Figs. 6.12, 6.13 and 6.14, respectively. Since the physical meaning of the time signal measured by an MPT is strain rate, we divided the peak to peak values of the signals by the frequency to convert the information in the time signals into strain values. The strain values are normalized with the maximum strain value measured for the transducer without a resonator in each case. As shown in Figs 6.12 ~ 6.14, the simulation and experimental results agree well with each other in all cases. However, in Fig. 6.12, the output increase in the experiment is slightly weaker than the simulation result because of the narrow bandwidth that is difficult to show the tendency in the finite time domain and energy

loss due to damping in the system which was not considered in the analyses. The time signals at the peak frequencies ( $f_{p1}$ ,  $f_{p2}$  and  $f_{p3}$ ) of each case are also shown in Figs. 6.12 ~ 6.14, where the red and blue line indicates the results with and without resonators, respectively. The figure shows that the transmitted signals are well increased by simply attaching the U-shaped resonators. Experimentally, over 70 % increases in outputs are observed.

### **6.3 Realization of a resonator for axisymmetric A0 Lamb wave**

As already mentioned in section 4.3, resonators can be applicable with axisymmetric waves. Axisymmetric A0 Lamb wave is not exceptional as well. By revolving the cross-section of resonator respect to the axis, a new resonator for axisymmetric A0 wave is proposed, as shown in Fig. 6.15.

Simulations to demonstrate enhancement of the wave emission were performed, as shown in Fig. 6.16. The emitted A0 wave with and without resonator is plotted in Fig. 6.17. As shown in Fig. 6.17, the A0 wave emission is enhanced more than 3 times than the maximum output of transducer without the resonator.

### **6.4 Summary**

A method to improve the transduction efficiency of A0 wave by implementing a U-

shaped resonator on a MPT was proposed. The U-shaped resonator had a significant influence on the generation mechanism of A0 wave. Once the U-shaped resonator is triggered by the driving force of the actuator, the resonance of the resonator delivers additional driving forces to the plate to enhance the output A0 wave.

Observing the motion of the resonator, it was modeled as a generalized spring-mass system, and the output A0 wave of the transducer with the resonator system was coupled with Timoshenko beam theory. Among many motions of the resonator, the vertical spring-mass resonance was revealed to be the main factor of the wave enhancing phenomena. It was because of the assumption that the motion of the resonator is symmetric, guaranteed by the U-shaped geometry of the resonator. The theoretical analyses were solved rigorously with reasonable assumptions in kinematics and dynamics of the resonator and the beam. The theoretical analysis using the generalized spring-mass system well coincided with the numerical result, thus the analytical solution was validated. Also, both the analytical and numerical analyses were verified by experiments conducted with resonators made of glass. The magnitudes of the output A0 waves from the transducers with U-shaped resonators were improved over 70 % compared to those without resonators. With analytic, numerical and experimental results, the output enhancing mechanism in a transducer using a U-shaped resonator is well confirmed in this chapter.

## TABLES

**Table 6.1** Material properties of an aluminum plate and a resonator.

	Aluminum plate	Resonator
Young's modulus (GPa)	70.0	58.0
Poisson's ratio	0.3318	0.3300
Mass density (kg/m <sup>3</sup> )	2700	2500

**Table 6.2** Stiffness matrix, mass coefficients and eigenfrequencies of the U-shaped resonators.

	$S_{11}$	$S_{12}$	$S_{13}$	$S_{21}$	$S_{22}$	$S_{23}$
Case 1	1.36 N/m	-0.75 N/m	-1.66 N/rad	-0.75 N/m	1.42 N/m	0.44 N/rad
Case 2	2.39 N/m	-1.20 N/m	-2.11 N/rad	-1.20 N/m	2.55 N/m	0.52 N/rad
Case 3	4.39 N/m	-1.96 N/m	-2.54 N/rad	-1.96 N/m	4.03 N/m	0.47 N/rad
	$S_{31}$	$S_{32}$	$S_{33}$	$f_{eig2}$	$m$	
Case 1	-1.66 N	0.44 N	3.59 N·m/rad	63.2 kHz	0.0090 kg	
Case 2	-2.11 N	0.52 N	3.82 N·m/rad	73.4 kHz	0.0120 kg	
Case 3	-2.54 N	0.47 N	4.02 N·m/rad	84.1 kHz	0.0144 kg	

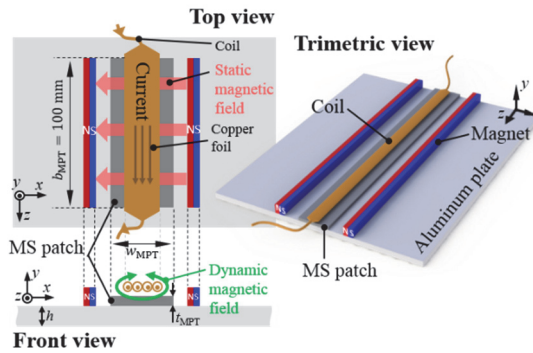


Figure 6.1 The nominal MPT with  $w_{\text{MPT}} = 10 \text{ mm}$ ,  $b_{\text{MPT}} = 100 \text{ mm}$ ,  $t_{\text{MPT}} = 0.15 \text{ mm}$ .

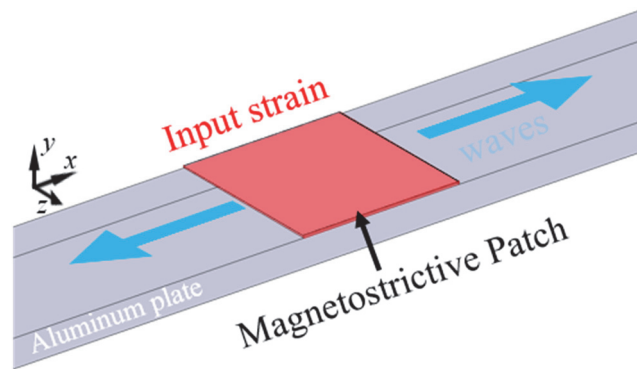


Figure 6.2 Actuation mechanism of the nominal MPT. The considered actuation wave mode in the plate is the A0 Lamb wave mode.

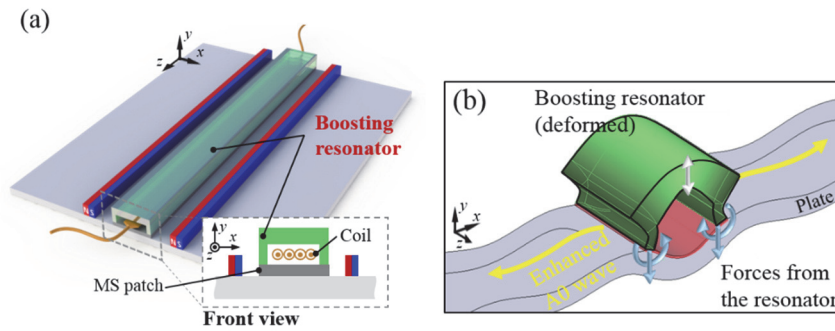


Figure 6.3 (a) The proposed MPT with an add-on type U-shaped resonator, a nickel patch was used as the magnetostrictive patch and (b) actuation mechanism of the proposed MPT.

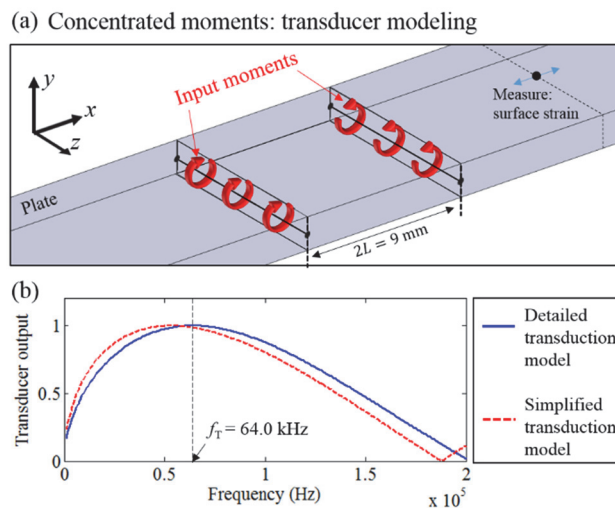


Figure 6.4 (a) A simplified transduction model of a magnetostrictive patch transducer. (b) The frequency characteristics of transducer efficiency of both detailed transduction model and the simplified transduction models.

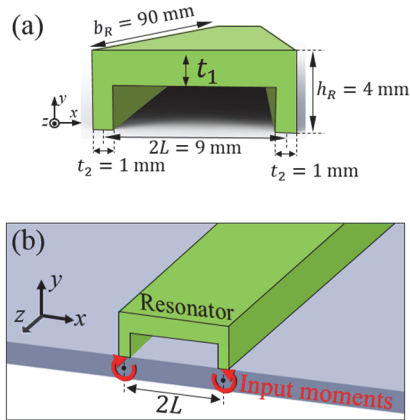


Figure 6.5 (a) A drawing of the proposed U-shaped resonator, (b) resonator on a plate with simplified transduction model.

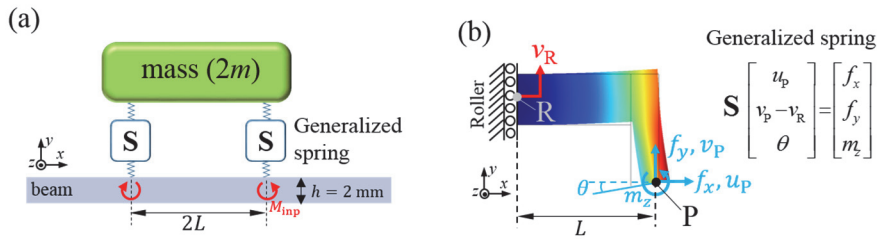


Figure 6.6 (c) Generalized spring-mass modeling of the U-shaped transducer on a beam and (d) relations between the generalized spring of a resonator, forces and displacements.

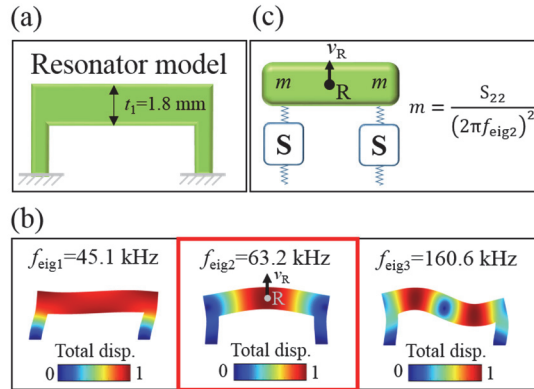


Figure 6.7 (a) The cross-section of the U-shaped resonator case 1 and (b) the first 3 eigenmodes of the U-shaped resonator case 1. (c) A description of the motion of the inertia part in the resonator.

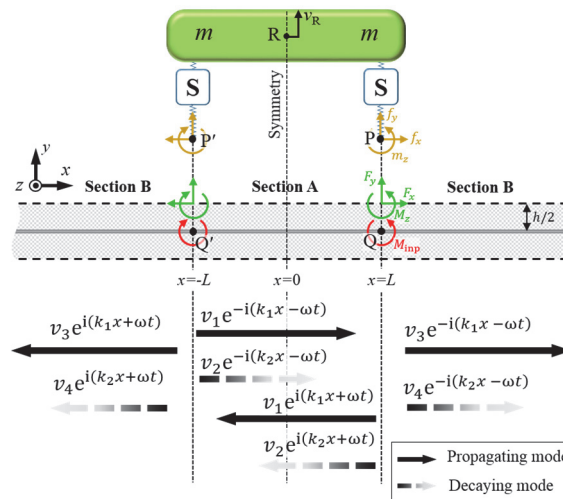


Figure 6.8 A description of force and moment interactions between a U-shaped resonator and a Timoshenko beam, and overall wave solutions in the beam.

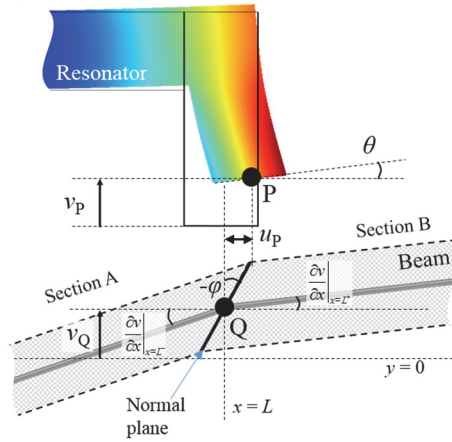


Figure 6.9 A detailed description of the kinematics between the U-shaped resonator and the underlying beam.

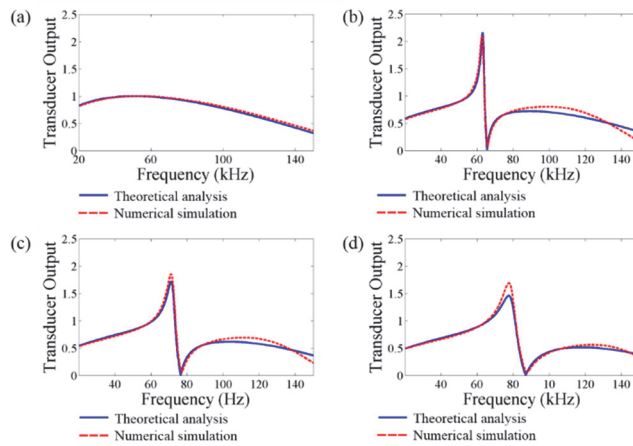


Figure 6.10 Transducer outputs ( $|\varepsilon_x|$  on the plate surface of section B) (a) without resonators, (b) with resonator case 1, (c) with resonator case 2, and (d) with resonator case 3 solved by Timoshenko beam analysis and FEM analysis.

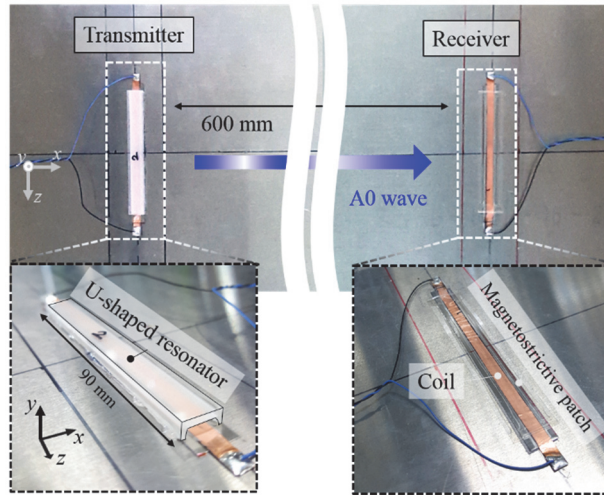


Figure 6.11 Experimental setup to measure the elastic waves generated from the transmitters with and without resonators.

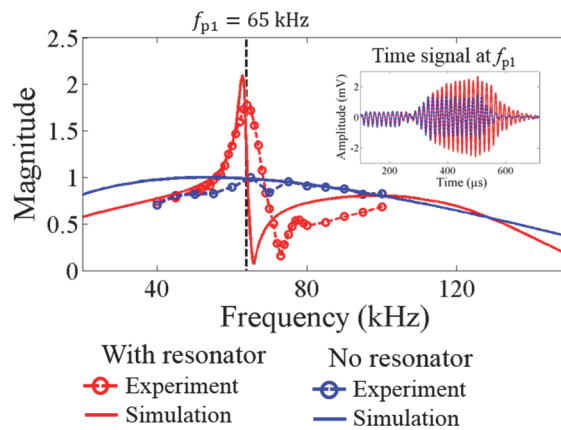


Figure 6.12 The frequency characteristics of the transducers and time signals in peak frequencies with resonator case 1 from the experiments and simulation results.

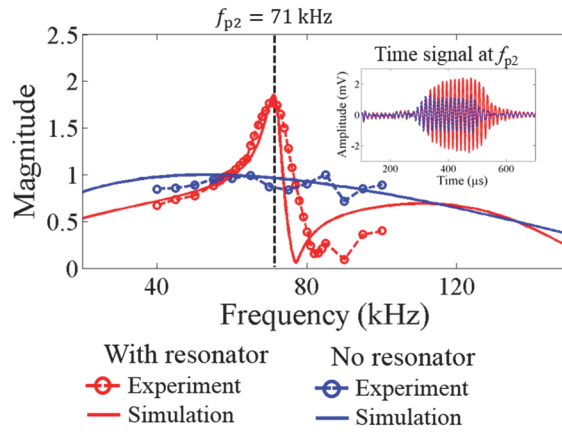


Figure 6.13 The frequency characteristics of the transducers and time signals in peak frequencies with resonator case 2 from the experiments and simulation results.

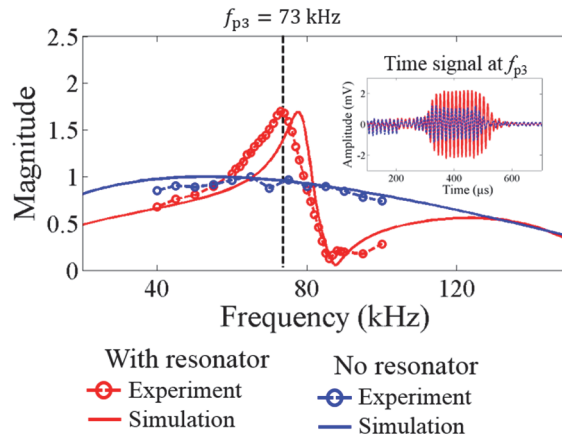


Figure 6.14 The frequency characteristics of the transducers and time signals in peak frequencies with resonator case 3 from the experiments and simulation results.

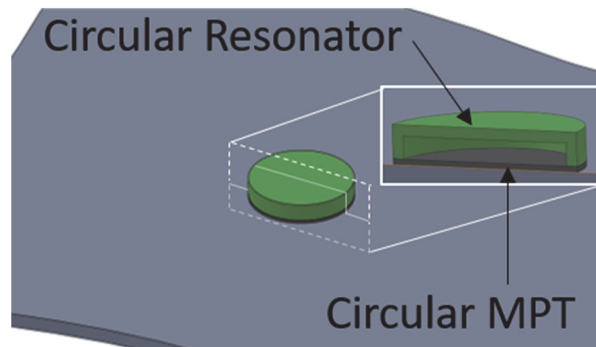


Figure 6.15 Illustration of application of resonators for axisymmetric A0 wave.

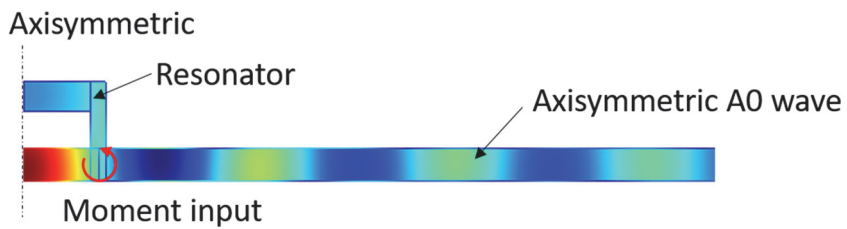


Figure 6.16 Illustration of numerical simulations of wave transduction with resonator for axisymmetric A0 wave.

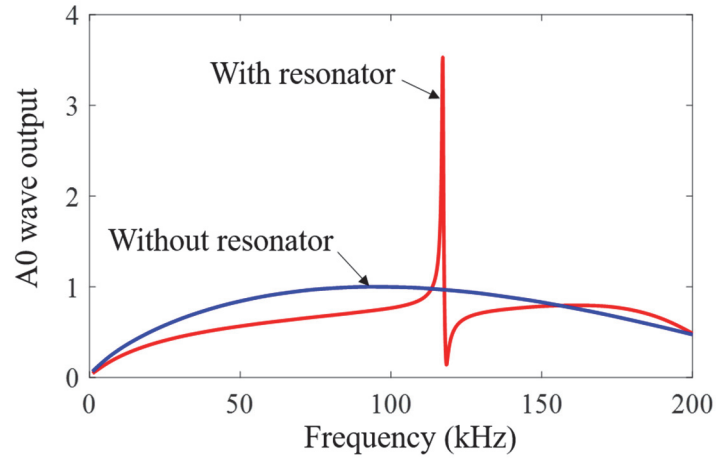


Figure 6.17 Plots of emitted axisymmetric A0 wave with and without resonators.

# CHAPTER 7.

## CONCLUSIONS

This thesis proposed a passive and nondestructive idea, resonator pairing, to improve the wave emission from transducers including piezoceramic transducer and magnetostrictive patch transducer. The idea is realized to enhance the emission of various guided waves in a plate. Furthermore, by establishing an equivalent system of the proposed system, the effective impedance analysis is performed to explain the reason of the wave enhancing phenomena. The detailed contributions of this work can be summarized as follows:

First, the proposed resonator pairing idea can be used to amplify the wave output from any wave source. From the fact that the output displacement (or strain field) is increased with same input force, the effective impedance should have been reduced. However, conventional characterization methods of material parameters for

metamaterials are not suitable for the paired resonator system. Therefore, this thesis introduces a new method to characterize the impedance of paired resonator system, which is neither in subwavelength structure nor periodic arrangement. Setting up an equivalent system including an effective medium of the original system, the effective impedance is characterized. The effective impedance can be reduced by the resonator pair, even to nearly zero depending on the resonance frequency of the resonators. The wave amplifying performance directly depends on the effective impedance. To successfully transmit the amplified wave to outside of the resonators, a Fabry-Pérot resonance condition is found to be the key phenomenon. With low impedance medium, the displacement field inside the resonators is amplified and Fabry-Pérot resonance enables the full transmission through the highly mismatched impedances.

Secondly, a way to realize the point resonator pairing idea is proposed to be used for guided waves in a plate. Using the similarity between the in-plane waves in a plate and the one-dimensional beam wave, the wave output enhancement is observed in  $S_0$  and  $SH_0$  wave in a plate. For each wave, a compatible design of the realized resonator is proposed so that the resonator is consistent with the point resonator in the theory. Using numerical simulations, the method to characterize the spring and mass constant of the resonator is derived. Also, experiments are performed to verify the simulation and the theory, using PZT for  $S_0$  wave and MPPT for  $SH_0$  wave. Using various transducers, the thesis implies that the wave output enhancement can be used

with any transducers, including EMATs, laser transducers and air-coupled transducers. The proposed system is expected to be useful for transducer industries, medical ultrasound industries and nondestructive evaluation industries.

Thirdly, the proposed resonator paired system is proved to have the same sensing enhancement in receiving mode as the enhancement in the transmitting mode. It is easily predicted that the sensing performance should be reciprocal. However, in this thesis, an analytical analysis is performed and the sensing enhancement is rigorously proven. Also, the same equivalent system is applied and showed that the equivalent system has same size of effective medium with same effective impedance. Because of the low impedance, the waves inside the effective medium are amplified. Experiments using PZT and MPT for S0 and SH0 wave are performed to verify the analyses. The sensing enhancement phenomenon in the proposed system is expected to be useful in energy harvesting industries.

Finally, the resonator pairing method is applied for bending wave in a plate. The discrepancy between the bending wave in a plate and one-dimensional beam wave disables the effective medium theory to be directly apply on the bending wave. However, using Timoshenko beam theory and elaborately designed resonator, the bending wave can be enhanced. Analysis and experiments are performed.

# **Appendix A.**

## **Output enhancing of omnidirectional Lamb wave-MPT by slits in a patch**

### **A.1 Introduction**

Nondestructive evaluation that exploits guided elastic waves is effective for use in pipes and plate-like structures, and as a result, related research has been extensively conducted (see, e.g., [62, 76, 77]). Among the different type of transducers that generate guided elastic waves, this work focuses on transducers that generate omnidirectional waves [23, 78-80]. A phased array system that uses omnidirectional transducers can conduct inspections along all directions around the system by adequately tuning the time-delays and amplitudes in the transducers [81-85]. The performance of the phased array system during an inspection is seriously affected not only by the uniformity of the waves propagating in all directions but also by the output power. This study aims to find a method to increase the output of an

omnidirectional Lamb wave magnetostrictive patch transducer (OL-MPT) [6]. (Here, the transducer output represents the axisymmetric elastic deformation of the circular patch of an OL-MPT.) Specifically, we investigate the effects that the configuration of a magnetostrictive patch has on the output power of OL-MPTs.

Before discussing a method to improve the transducer output, we will briefly explain how omnidirectional Lamb waves are generated in a plate by an OL-MPT. As shown in Fig. A1(a), an OL-MPT is composed of a thin magnetostrictive patch (the material used in the figure is nickel), a coil and a permanent magnet. The magnetostrictive patch is bonded onto the test plate with adhesives or is mechanically coupled to the test plate using couplants. The magnetostrictive patch is deformed by the coupling effect between the magnetic field and the elastic deformation, and the deformation in the patch generates guided waves in the test specimen. Magnetostrictive patch transducers (MPTs) and electromagnetic acoustic transducers (EMATs) are related in the sense that they both operate using magnetic fields. However, the detailed mechanisms for each are quite different since EMATs use the Lorentz force and MPTs use magnetostriction to generate elastic waves. Generally, the magnetostriction force has been reported to be two orders of magnitudes larger than the relevant Lorentz force [86-88]. Since MPTs can generate a larger power output than EMATs can by utilizing magnetostrictive patches, MPTs are more suitable for long-range guided wave inspection. Further details on the mechanism and

applications for MPTs has been well described in another work [17].

In order to improve the power output of an OL-MPT, it is necessary to know the detailed mechanism of the OL-MPT. An omnidirectional Lamb wave can be generated when all components, including the nickel patch, coil and permanent magnet, are in an axisymmetric configuration, such as with a circular, annular or cylindrical shape, as depicted in Fig. A1. Figure A1(b) shows the top view and side views of an OL-MPT, and the directions of the magnetic fields from the coil and the permanent magnet are schematically sketched. Both the static magnetic field from the magnet and the dynamic magnetic field from the coil have a radial direction to generate Lamb waves. As a result of the Joule effect [68], an axisymmetric radial strain is induced. The strain in the magnetostrictive patch is transmitted to the hosting plate via the couplant layer, and Lamb waves eventually propagate omnidirectionally in the plate.

We will now focus on the distribution of the magnetic field, particularly the dynamic magnetic field in the magnetostrictive patch because the distribution and magnitude of the dynamic magnetic field determines the strength of the elastic deformation in the magnetostrictive material [17]. When an alternating current is applied in the coil to produce a dynamic magnetic field, an eddy current has to be induced on the magnetostrictive patch [87, 88]. In an OL-MPT, as illustrated in Fig. A2(a), the eddy

current ( $\mathbf{J}_1$ ) is induced in the circumferential direction on the top surface of the circular patch. As in the results of the numerical analysis that are shown in Fig. A2(b), the eddy current  $\mathbf{J}_1$  sharply decreases in the thickness direction. As a result of the skin effect, the radial dynamic magnetic field,  $\mathbf{H}_1$ , is applied locally on the top surface of the patch (Fig. A2(c)). An actual magnetization curve of nickel [18] used for the numerical analysis. For numerical simulations, the input current in the coil was simplified as a uniform surface current rotating on an annular surface above the magnetostrictive patch with the surface current density of  $1.0 \times 10^4 \text{ A/m}^2$  and the frequency of 270 kHz. A schematic geometry of the numerical simulation is depicted in Fig. A3. Following [19], an electromagnetic simulation of the OL-MPT (using [20]) was performed (including the air domain). Since the eddy current and magnetic field are induced locally on the patch surface, the deformation occurs only at the surface. In other MPTs, such as MPTs using a figure-of-eight coil [70], the eddy current induced by the input current of the coil circulates not only on the top surface but also on the bottom surface of the magnetostrictive patch, so the magnetic field can be applied on both surfaces. In this case, the deformation occurs throughout the patch, and a considerably larger output is generated. However, its nature to generate an axisymmetric radial magnetic field in an OL-MPT limits the eddy current and the magnetic field to be locally applied on the top surface. Negative signs in  $J_\theta$  and  $H_r$  around the middle of the nickel patch are due to the exponential field behavior with a complex exponent because of the skin effect [87]. The increase in the magnitude

of the input current just to increase the output has some hazards on the electric equipment, and it would not affect any of the sensitivities if the transducer is used as a sensor. Hence, the dynamic magnetic field needs to be applied throughout the magnetostrictive patch as much as possible to increase the power output of an OL-MPT with a given amount of input current. In other words, the eddy current circuit should be accordingly modified.

Many similar studies have reported on the reduced eddy current losses in giant magnetostrictive actuators as examples where eddy current circuits are controlled in actuators and transducers by using magnetostrictive materials [89-91]. However, no studies have been carried out to control eddy current circuits in transducers using a thin magnetostrictive patch, such as OL-MPTs (Fig. A1).

Meanwhile, a method that improves the power output of an OL-MPT has been recently reported [92]. Since the reported method does not improve the performance of an OL-MPT from the perspective of an eddy current circuit, this work focuses on the systematic performance improvement by modifying the eddy current circuit. A method is proposed to control the eddy current circuit, and the corresponding changes in the magnitudes and radial patterns of the output fields are both numerically and experimentally investigated. We will investigate the electromagnetic changes when a radial slit is introduced in the magnetostrictive

patch and the effects of the electric conductivity of the test plate through numerical analyses. Then, the magnitudes and radial patterns of the output fields of the patches with multiple radial slits will be investigated and verified using both simulations and experiments in order to improve the effect and to guarantee the omnidirectional property of the transducer.

## **A.2 Patch slitting effect on eddy current circuit**

This section proposes a method to control the eddy current circuit in the magnetostrictive patch in order to broaden the domain where the dynamic magnetic field can be applied. As has already been investigated in Fig. A2, the eddy current in a circular magnetostrictive patch induced from an annular coil is able to form a complete circuit, even if it flows only on the top surface of the patch. Therefore, to make the eddy current circulate on the bottom surface of the patch, a patch shape other than an axisymmetric shape, as suggested in Fig. A4(a), should be proposed.

In this appendix, a radial slit is made in a patch to interrupt the axial symmetry, and as a result, we propose a method to produce a certain amount of eddy current on the bottom surface of the patch. So, the distributions of the eddy current and the dynamic magnetic field in the patch with a slit should be analyzed. As expected, the patch with a slit would not generate a uniform omnidirectional Lamb-wave. Therefore, the radiation patterns of the OL-MPTs using patches with symmetrically arranged

multiple slits versus the number of slits will be investigated in the next chapter.

Fig. A4(a) shows the shape proposed for the magnetostrictive patch with a radial slit. An annular coil is placed over the patch, and the patch is bonded to an aluminum plate with a couplant layer. The eddy currents on the top and bottom surface of the patch,  $\mathbf{J}_1$  and  $\mathbf{J}_2$ , and the magnetic fields applied on both surfaces,  $\mathbf{H}_1$  and  $\mathbf{H}_2$ , are indicated in Fig. A4(a). On the other hand, the eddy current induced on the aluminum plate is denoted by  $\mathbf{J}_3$ . Note that unlike in the slit-less circular patch, the eddy current generated on the top surface cannot pass the air gap in the slit patch, so the current should flow along the slit surface. After flowing down along the slit surface, the eddy current flows on the bottom surface until the current meets the slit, and it then flows up along another slit surface. Eventually, the eddy current flows on the top surface again to complete the circuit. In this case, the eddy current on the top surface  $\mathbf{J}_1$  and that on the bottom surface  $\mathbf{J}_2$  are in opposite directions, as shown in Fig. A4(a).

Fig. A4(b) shows the distributions of the circumferential component of the induced current density along the  $z$ -direction in the magnetostrictive patch, the couplant layer, and the hosting aluminum plate at some locations of  $30^\circ$ ,  $60^\circ$  and  $90^\circ$  aside from the slit. The result in Fig. A4(b) is obtained from a numerical analysis [93], and the material properties in table A1 are used for the analysis. The static and dynamic magnetic fields are solved using the magnetization curve of nickel [94], and the

magnetostrictive nickel patch has a radius of 15 mm and a thickness of 0.15 mm. The harmonic analysis is conducted at 270 kHz, which is the frequency at which the OL-MPT has the largest output. An alternating current is inputted circumferentially along the shape of the coil, which is 0.1 mm above the patch, to obtain the distributions of the eddy current and the dynamic magnetic field. The current distribution induced along the direction of the thickness is solved through a numerical analysis, as shown in Fig. A4(b). This result shows that the eddy current on the top and bottom surfaces has opposite signs, and it is evidence of the theory that the eddy current circulates along all of the top, bottom and slit surfaces, as was explained earlier.

In the slit-less circular patch in Fig. A2, the directions of the input current in the coil and the eddy current on the patch are opposite, so the magnetic fields were perfectly canceled under the region where the eddy current was induced. In the slit patch in Fig. A4, the eddy current that is induced on the top surface  $\mathbf{J}_1$  is still in the opposite direction to the input current of the coil. However, the current induced on the bottom surface  $\mathbf{J}_2$  is in the same direction as the input current. The eddy current on the bottom surface  $\mathbf{J}_2$ , as well as  $\mathbf{J}_1$ , is also formed to cancel the magnetic field inside the patch. However, in the region just under the bottom surface, the magnetic field from  $\mathbf{J}_2$  is in the same direction as the magnetic field generated from the input current. Therefore, the eddy current on the bottom surface  $\mathbf{J}_2$  allows the magnetic field to be

transmitted under the patch, and the transmitted magnetic field induces another eddy current on the metallic test specimen. As indicated in Fig. A4(b), a new eddy current  $\mathbf{J}_3$  is induced on the aluminum plate. Although the eddy current on the aluminum plate was originally induced to cancel the magnetic field in the metallic plate region, this increases the magnetic field in the region above the plate. As a consequence, the eddy current on the hosting plate generates an additional magnetic field. As shown in Fig. A4(c), which is the distribution of the radial magnetic field obtained from the numerical analysis, the additional magnetic field  $\mathbf{H}_2$  generated from the eddy current on the plate  $\mathbf{J}_3$  is applied on the bottom side of the patch.

Fig. A5 shows the distribution of the magnetic flux densities on both the top and bottom surfaces of a slit-less circular patch and a slit patch. There are few differences in the magnetic field distributions between the top surfaces of the patches. However, a clear difference appears on the bottom surfaces of the patches. While no magnetic field is applied on the bottom surface of the slit-less patch, a magnetic field of considerable magnitude is applied near the slit on the bottom surface of the slit patch. As a result, the total amount of magnetic field applied near the slit increases when compared to that for the slit-less patch because the magnetic field from the eddy current on the hosting plate as well as the magnetic field from the input current has been applied.

We verify the effects that are described above by making a comparison for the case where the transducer made with a slit patch is used on a nonmetallic glass plate. Theoretically, the eddy current has to circulate on both the top and bottom surfaces regardless of the material type of the hosting plate, as shown in Fig. A6(a). A numerical analysis was conducted using the same configurations as earlier, but with a different type of material for the plate. The distributions of the induced circumferential current density and the radial magnetic field along the  $z$ -direction at some locations of  $30^\circ$ ,  $60^\circ$  and  $90^\circ$  aside from the slit are plotted in Figs. A6(b) and (c), respectively. The eddy current distribution in Fig. A6(b) shows that eddy currents on the top and bottom surfaces of the magnetostrictive patch have different signs, so the eddy current circuit can be seen to have also changed in the case where the slit patch is installed on a glass plate. In addition, a nonzero magnetic field is applied on the bottom surface of the patch, as shown in Fig. A6(c). The biggest difference from the case of the slit patch that is installed on an aluminum plate is that no eddy current has been induced on the glass plate. Thus, the magnetic field has a certain value and does not decrease to zero in the region of the glass plate.

Figure A7 compares the induced current density and the magnetic field distributions in the cases of i) a slit-less patch installed on an aluminum or glass plate and ii, iii) single-slit patches installed on aluminum and glass plates. When a slit patch is installed on an aluminum plate, there is a slight loss in the magnetic field on the top

surface when compared to the case with the slit-less patch, but a large magnetic field that can overcome the loss on the top surface is applied on the bottom surface. In the magnetic field distributions of Fig. A7(b), the total amount magnetic field applied in the slit patch is 28.9% larger than that in the slit-less patch. The magnitudes of the eddy current and the magnetic field on the bottom surface of the slit patch on the glass plate remarkably decreased when compared to the case of the slit patch on an aluminum plate. As a consequence, the total amount of magnetic field applied in the slit patch on a glass plate is only 0.5 % larger than that in the slit-less patch, which means that the net magnetic field did not increase at all on the glass plate. These results indicate that the electric conductivity of the hosting plate is the main cause of the different outcomes because it is the only difference between the two plates. Thus, an additional magnetic field has in fact been applied to the slit patch due to the presence of the eddy current on the hosting plate. Since aluminum is a good conductor, a sufficient amount of eddy current is induced on the aluminum plate because the skin depth in the plate is smaller than the thickness of the plate. If the electrical conductivity of a plate is so low that the skin depth is larger than its thickness, the total amount of induced current on the plate would be decreased compared with that on an aluminum plate. Therefore, the amount of additional magnetic field generated by the eddy current on the plate will be decreased, little enhancing the transducer output. On the other hand, if the electrical conductivity of a hosting plate is large enough to make the skin depth smaller than its thickness, the

electrical conductivity would have little influence on the transducer output.

Since a larger total applied magnetic field generates a greater deformation in the magnetostrictive patch, the differences in the net applied magnetic field should have a direct effect on the output power of the magnetostrictive transducers that generate elastic waves. The output elastic wave in the case with a slit patch on an aluminum plate will increase as a result of the increase in the net applied magnetic field in the patch. However, the output would not increase on the glass plate. Fig. A8 shows contour plots of the radial displacement components on the mid-plane of the plates that are generated by the transducers using slit and slit-less patches. Figure A8 clearly shows that the elastic wave output of the slit patch installed on an aluminum plate is larger than any of the other cases, and the radiation patterns of the lowest symmetric Lamb waves ( $S_0$  waves) are plotted in Fig. A9 to quantitatively investigate the magnitudes of the outputs. In the radiation patterns, the slit direction was set as the reference direction for  $0^\circ$  and the radial displacement components were plotted up to  $180^\circ$ . Figure A9 shows that the slit patch generates a substantially larger output in all directions for the aluminum plate. In particular, the magnitude of the elastic wave that propagated in the direction of the slit direction increased by approximately 28.1 % relative to that of the elastic waves generated from the slit-less patch. The increase in the elastic wave is similar to that for the total magnetic field applied in the patch, which was of approximately 28.9 %. In the radiation pattern, the

propagated wave along the opposite direction ( $180^\circ$ ) to the slit direction is also increased. This is because the increased deformation near the slit generates waves in both directions. It is also related to the radiation characteristics of MPTs as observed in [26]. On the other hand, the changes in the magnitudes of the elastic waves generated from the slit patch on a glass plate are very small when compared to those of the previous case. Overall, the transducer output increases when metallic plates are used but does not increase with nonmetallic plates. The transducer output increases because the additional magnetic field induced from the metallic plate generates an additional magnetostriction in the magnetostrictive patch. In this section, most of the electromagnetic effects were held near the slit, and as a consequence, only the magnitudes of the elastic waves radiated near the slit direction increased.

Until now, the power output has been investigated by numerical analyses. We will now present experimental results to verify the findings from numerical calculations such that the signal output of the transmitting transducer with a slit patch is increased compared with that of the slit-less patch transducer. Figure A10 shows the samples of the manufactured patches that were used for the experiments. The experimental setup for the MPTs installed on the aluminum and glass plates is shown in Fig. A11. For the receiver, an original OL-MPT made of a slit-less patch was used. The distance between the transmitter and the receiver is 200 mm. Since the experiment aims to compare the performance of a slit-less patch and the patch with a single slit,

the receiver on the slit direction, i.e., R1 (indicated in Fig. A11), was used to measure the transmitted signals.

A modulated Gaussian pulse [95], also known as a Gabor pulse with a center frequency of 270 kHz, is plotted in Fig. A12(a). This pulse is input into the transmitter, and the signals from receiver R1 are measured. Figures A12(b) and A12(c) show the signals measured in aluminum and glass plates, respectively. The peak-to-peak value of the output signal of the MPT made with a 1-slit patch,  $V_{R1}^1$ , is 25.1 % larger than that of the slit-less patch,  $V_{R1}^0$ , on an aluminum plate. The experimental results indicate that the transducer output increases for the aluminum plate, and this is consistent with the increase in the output obtained from the numerical results, 28.1 %. However, the experimental results obtained with the glass plate, which are plotted in Fig. A12(c), show that there is almost no difference between the outputs of the transducers when using slit-less and 1-slit patches, which is also in good agreement with the numerical results. Both the numerical and experimental results suggest that a slit on the magnetostrictive patch produces an eddy current that is induced on the bottom side of the patch, and this increases the transducer output if a magnetic field of a considerable magnitude can be applied to the bottom surface of the patch by a current induced on the metallic test specimen.

### **A.3 Effects of the numbers of slits on the transducer performance**

When a single slit was made in a circular magnetostrictive patch, the electromagnetic phenomenon was asymmetrically held since the slit was asymmetrically located. Most of the effects occur on the region near the slit, so the radiation pattern of the transducer using the 1-slit patch was not uniform in all directions. If we increase the number of slits symmetrically in the patch so that the electromagnetic effect is held symmetrically in several directions, it will be possible to generate a quasi-omnidirectional elastic wave. In this section, we investigate the changes in the distribution of the magnetic field and the output elastic wave with an increase in the number of slits to 2, 4, 8 and 12, as shown in Fig. A10.

The distributions of magnetic flux densities for both the top and bottom surfaces of the magnetostrictive patches installed on an aluminum plate with various patch shapes obtained from the numerical analyses are shown in Fig. A13. The field distributions on the top surfaces of the patches are virtually unaffected by the number of slits. However, the uniformity of the field varies significantly on the bottom surfaces. As the number of slits becomes larger, the magnetic field is more uniformly distributed throughout the patch, and the distribution in the patches with over 8 slits are almost uniform. Therefore, the patches with at least 8 slits are predicted to create uniform outputs throughout all directions. Omnidirectivity is important to facilitate phased array based signal processing because nonuniformity in individual

transducers would cause difficulties in postprocessing measured data.

Figure A14 plots the radial magnetic field ( $H_r$ ) integrated along the  $z$ -direction inside the magnetostrictive patch as a function of the circumferential angle. As the number of the slit ( $n$ ) is increased, the magnetic field is also increased. However, the increase rate is not significant if the number of slits is more than or equal to 8. Also, the field distribution over the circumferential angle becomes sufficiently uniform in such cases.

The radiation patterns of the output elastic waves obtained from both numerical analyses and experiments are plotted in Figs. A15 and A16. For the experiments, the configuration shown in Fig. A11 was used, and the signals are measured from  $0^\circ$ , which is the slit direction, to  $90^\circ$  with each interval of  $15^\circ$ . The radiation patterns are measured for the transmitters made of patches with 4, 8 and 12 slits and are normalized by the signals measured from the transmitter made of a slit-less patch. If the amplitude in the radiation pattern is indicated as 1.5, the magnitude of the output signal of a transducer is 50 % larger than the output of an OL-MPT made with a slit-less patch. The OL-MPTs made of slit-less patches are used for the receivers while the patches used for the transmitters were replaced every time.

Right to the radiation patterns, the signals measured from the experiments are plotted

in Figs. A15 and A16. For the patches with  $n$  slits, the peak-to-peak value of the S0 signal measured from the  $m$ -th receiver,  $R_m$ , is expressed as  $V_{R_m}^n$ . This value is normalized by the peak-to-peak value of the output signal from a slit-less patch,  $V_{R_m}^0$ , that is plotted in the radiation patterns.

The results in Figs. A15 and A16 show that the radiation patterns extracted from the analyses are consistent with the results obtained from the experiments. The radiation pattern is not quite circular for the patch with 4 slits, as shown in Fig. A15(a), and the same patterns periodically appear since the slits are located every  $90^\circ$ . In the cases of the patches with over 8 slits, the effects from all slits are superposed and the outputs are averaged in all directions. To quantitatively show the omnidirectivity of the output elastic waves versus the number of slits, the ratios of the minimum to maximum peak-to-peak values obtained from the radiation pattern signals are plotted in Fig. A17. This value cannot exceed 1 but the transducer output becomes more omnidirectional when the value is closer to 1. For the case with the aluminum plate, the value of the patches with 4 slits is respectively low, but with over 8 slits, the value almost approaches the omnidirectional limit obtained in the numerical analyses. The radiation patterns of the patches with over 8 slits are nearly omnidirectional as the ratio of the minimum to maximum values of the radiation patterns was estimated to be of over 0.95 in the results of the experiment. In the cases where patches are installed on a glass plate (Fig. A17(b)), the radiation patterns are more

omnidirectional than those installed on an aluminum plate because the net magnetic field applied for a patch does not change on the nonmetallic plates. Hence, the magnitude of the output elastic wave did not change even in the slit direction.

It will be interesting to compare the radiation pattern by the 4-slit patch transducer with that by the 8-slit or 12-slit patch transducer in Fig. A15. In case of the 4-slit patch transducer, the radiation pattern is not uniform with the maximum magnitude appearing along the  $45^\circ$  direction. This phenomenon is found to be due to the non-axisymmetric distribution of the eddy current induced on the bottom surface of the magnetostrictive patch. (See section A.4 for more details.)

The change in the radiation patterns of the transducers versus the number of slits in the magnetostrictive patches has been investigated above. The changes in the magnitudes of the output elastic waves versus the number of slits in the patch will be now investigated. The magnitudes of the elastic waves propagating in the slit direction and the signals measured from the receiver R1 in the experiments are compared. Figure A18 compares the increase in the peak-to-peak values  $V_{R1}^n$  of the S0 signals to the output signals  $V_{R1}^0$  of the slit-less patch according to the number of slits and material types of the test plate (aluminum or glass). For the aluminum plate, the magnitude of the output elastic wave increases as the number of slits is increased. For the patch with 12 slits, the output increases by approximately 50%

when compared to that for the original slit-less patch. As already seen in Fig. A13, an additional magnetic field is induced on the region near the slits. If the distance between the nearest slits is close enough, the magnetic field induced from a slit overlaps the magnetic field from another slit, and thus the magnetic field becomes stronger. Note that in case of  $n = 4$ ,  $V_{R1}^4$  are local minima in Fig. A18. This is due to the destructive interference between the wave generated by the patch area near a horizontal slit and those by the patch areas near the neighboring vertical slits ( $\pm 90^\circ$  from the horizontal slit) in case of the 4-slit patch transducer. (This phenomenon only occurs in the 4-slit patch.)

The analysis above suggests that a stronger radiated elastic wave is generated with more slits. However, when the patch has over 8 slits, a weaker increase rate is seen compared to the case of the patches with fewer slits because in the patches with over 8 slits, the distances between the nearest slits are sufficiently close, so the magnetic fields are already induced strongly in the region between the slits, as in the region just near the slits. Hence a drastic increase in the magnetic field would not occur even if new slits are made between the slits. On the other hand, the output of the elastic waves did not increase when compared to the slit-less patch installed on a glass plate, regardless of any slits in the patches. Comprehensively, including the cases on both aluminum and glass plates, the additional magnetic field generated from the eddy current on a metallic plate still plays a key role in increase of the

transducer outputs.

#### **A.4 Detailed eddy current circuit and strain states**

The eddy current circuits in Fig. A4 is simplified as circular shape. It is true on the top surface of the magnetostrictive patch, since the input current on the coil forces to form an eddy current to cancel out the magnetic field inside the patch. However, the eddy current on the bottom surface of the patch does not have to follow the circular shape, as long as its primary goal is to connect the circuit broken by the slit. As shown in Fig. 19(a), the eddy current circuit on the bottom surface ( $\mathbf{J}_2$ ) of 1-slit patch is roughly circular shaped, but the circuit takes a shorter route just to circumvent the slit. As shown in Fig. A19(b), the circuit became more symmetric, with some anomalies in the circuit shape existing in 4-slit patch. It is because as the number of slit becomes larger, it is shorter to flow circumferentially toward the next slit than to circumvent the slit.

The shape of the eddy current circuit inevitably produces some amount of radial component ( $J_{2r}$ ) of the eddy current ( $\mathbf{J}_2$ ). The noncircular shape of the eddy current flow also generates the undesirable circumferential magnetic field component ( $H_{2\theta}$ ), which in turn generates the  $r$ - $\theta$  shear strain as shown in the left-slide plot of Fig. A20(b). Figure A20(b) also shows magnitude of the equivalent normal strain state in the  $45^\circ$ -rotated directions. Because of the large normal strain along the  $+45^\circ$

direction, the wave field in that direction is stronger than that in the slit direction. This wave field component can be observed in the radiation patterns in Fig. A9 and Fig. A15(a) that the radiation on  $45^\circ$  direction is enhanced by the phenomenon.

## **A.5 Summary**

A method was proposed to make a radial slit in a circular magnetostrictive patch as a means to improve the power output of an omnidirectional Lamb-wave magnetostrictive patch transducer. The presence of the slits in the patches had different effects on the transducer outputs depending on the material type of the test plates where the transducers are installed. In an OL-MPT installed on a metallic plate, cutting a radial slit in the circular magnetostrictive patch produced a change in the eddy current flow in the patch as well as in the eddy current on the metallic plate. The eddy current and the magnetic field were induced only on the top surface of the slit-less magnetostrictive patch. However, the eddy current flowed on both the top and bottom surfaces in a slit patch. This change in the eddy current circuit allowed the dynamic magnetic field to be applied on the bottom surface of the magnetostrictive patch. In particular, the conductive nature of a metallic plate allowed for a new eddy current to be induced on the plate, and the overall magnetic field applied in the patch increased as a result of the additional magnetic field generated from the eddy current on the plate. This mechanism caused an increase in

the transducer output on a metallic plate, and this finding was verified using both numerical simulations and experiments. In contrast, when an OL-MPT with or without slits in a magnetostrictive patch was installed on a nonmetallic plate (a glass plate for an example), the transducer output did not increase because the net magnetic field in the patch did not increase due to the absence of the eddy current on the nonmetallic plate. As a consequence, the patch slitting method was ineffective for nonmetallic plates.

Since the electromagnetic changes occur locally near the slit, the transducer output may not be omnidirectional, even though the output was enhanced by the slit. If the number of slits in the patch was increased, the radiation pattern of the slit patch became omnidirectional, especially with over 8 slits. The corresponding output elastic waves were sufficiently omnidirectional as the ratios of the minimum to maximum values in the radiation patterns were of over 0.95. The reason for this result was that the magnetic field distributions were relatively uniform in all directions for patches with over 8 slits. The omnidirectivity as well as the magnitude of the output elastic wave improved as the number of slits increased. On a metallic plate, the magnitudes of the output elastic waves increased with an increase in the number of slits in a circular patch. In this paper, the output of the patches with 8 symmetrically-arranged slits improved by almost 50 % of the output of a slit-less patch because the additional magnetic fields from each slit were superposed, strengthening the overall

magnetic field.

**Table A 1** Material properties of a nickel patch and test plates.

	Nickel Patch	Aluminum plate	Glass plate
Young's modulus (GPa)	204.8	70.3	70.0
Poisson's ratio	0.2866	0.3318	0.2200
Mass density (kg/m <sup>3</sup> )	8900	2700	2500
Electric Conductivity (10 <sup>6</sup> S/m)	14.35	37.82	0
Relative Permittivity	1	1	1
Relative Permeability	Magnetization curve [75]	1	1
Thickness (mm)	0.15	1	1

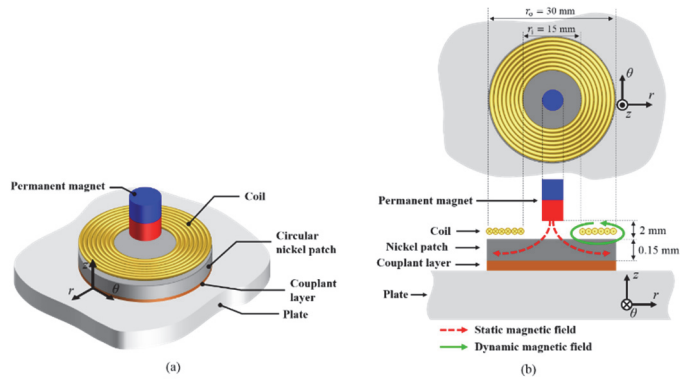


Figure A 1 (a) A configuration, (b) top view and side view of the OLMPT (omnidirectional magnetostrictive patch transducer) considered in this study.

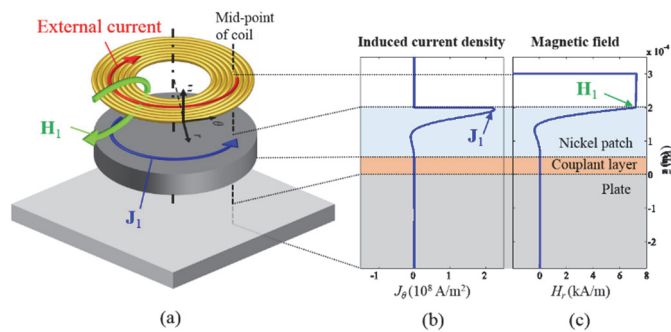


Figure A 2 (a) Field direction ( $H_i$ : magnetic field,  $J_i$ : induced current), (b) induced current density and (c) magnetic field distributions of an OL-MPT with a slit-less nickel patch installed on an aluminum plate. The induced circumferential current and radial magnetic field are measured along the  $z$ -direction on the mid-point of the coil (i.e., at  $r = (r_o + r_i)/2$ ).

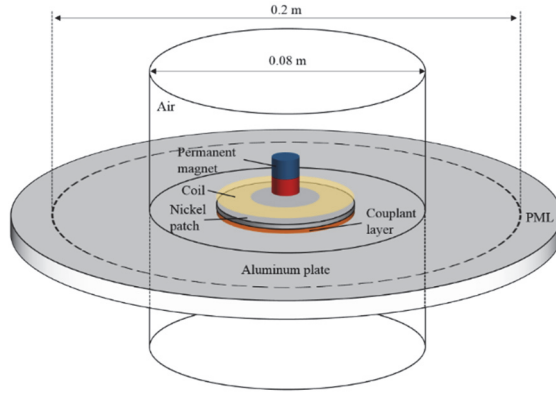


Figure A 3 Schematic description of the finite element model of the MPT, an aluminum plate and surrounding air for wave transduction simulation.

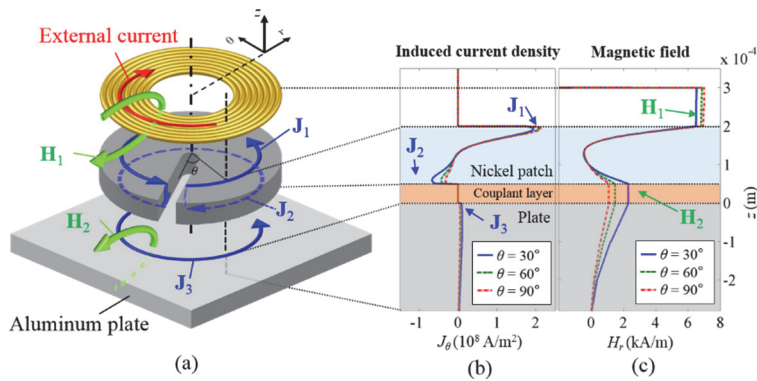


Figure A 4 (a) Field direction ( $H_i$ : magnetic field,  $J_i$ : induced current), (b) induced current density and (c) magnetic field distributions of a Lamb wave MPT with a slit nickel patch installed on an aluminum plate. The induced circumferential current and radial magnetic field are measured along the  $z$ -direction on the mid-point of the coil (i.e., at  $r = (r_o + r_i)/2$ ).

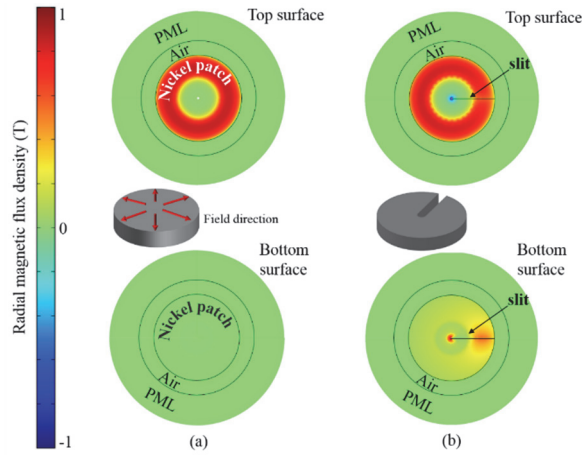


Figure A 5 Radial magnetic flux density plot in (a) a circular slit-less nickel patch and (b) a single-slit patch on their top and bottom surfaces.

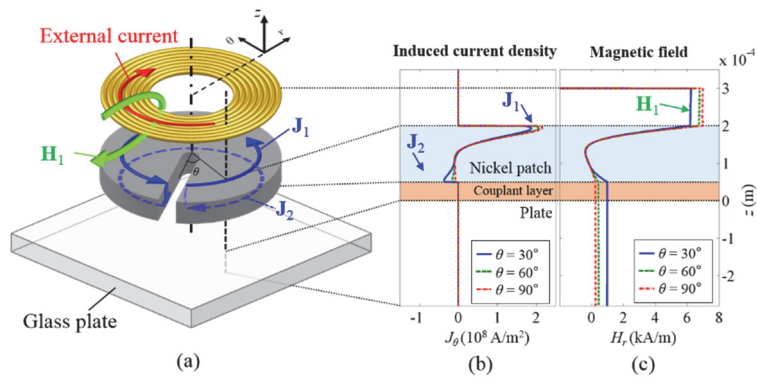


Figure A 6 (a) Field direction ( $\mathbf{H}_r$ : magnetic field,  $\mathbf{J}_\theta$ : induced current), (b) induced current density and (c) magnetic field distributions of a Lamb wave MPT with a slit nickel patch installed on a glass plate. The induced circumferential current and radial magnetic field are measured along the  $z$ -direction on the mid-point of the coil (i.e., at  $r = (r_o + r_i)/2$ ).

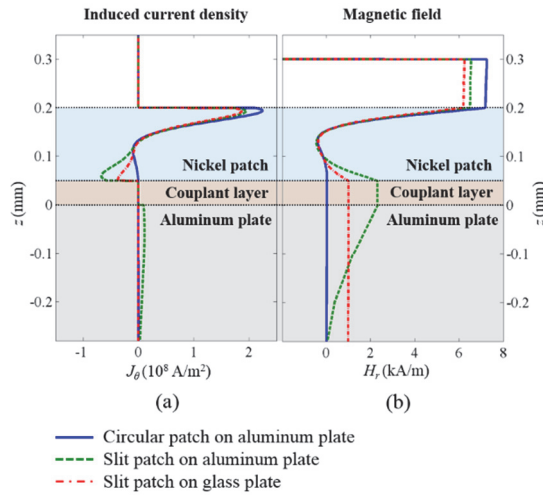


Figure A 7 (a) Induced current density and (b) magnetic field distributions of MPTs with slit-less and single-slit patches installed on aluminum and glass plates.

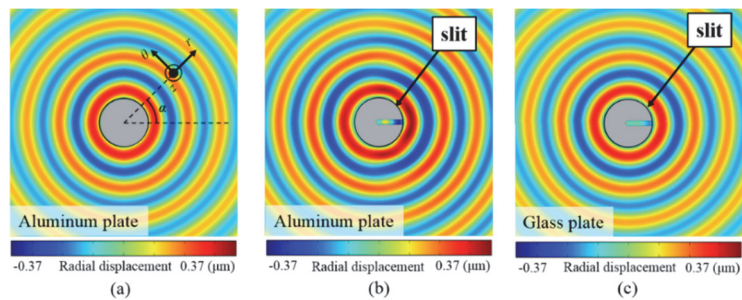


Figure A 8 Contour plots of the radial displacement (for a selected time) in the mid plane of the plates. The plots are obtained for MPT transmitters with (a) a slit-less patch, (b) and a single-slit patch on an aluminum plate and (c) single-slit patch on a glass plate.

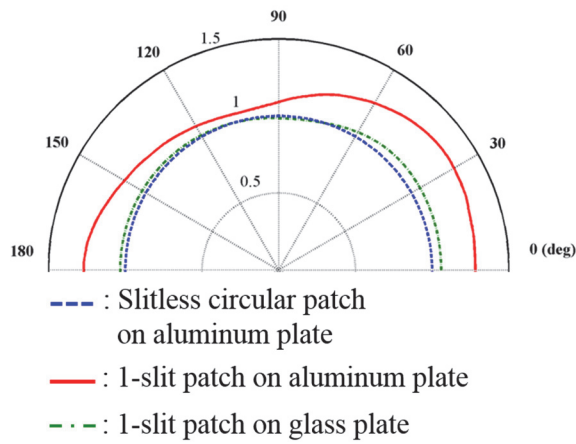


Figure A 9 Radiation patterns of the S0 modes in plates for MPTs equipped with different patch configurations installed on aluminum and glass plates.

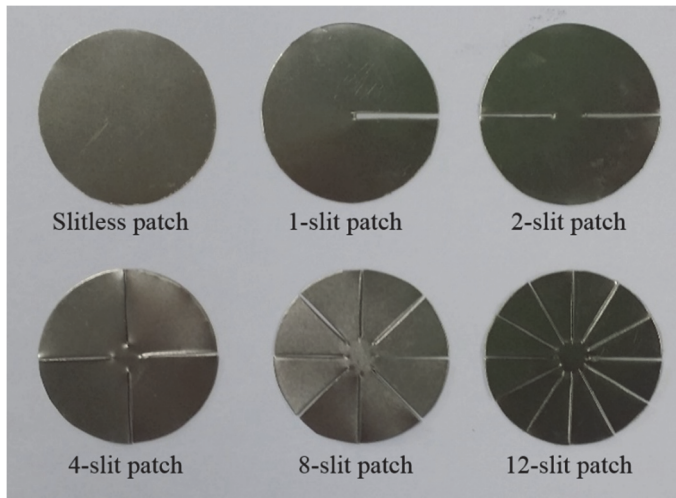


Figure A 10 Photos of the various patches considered for the experiments.

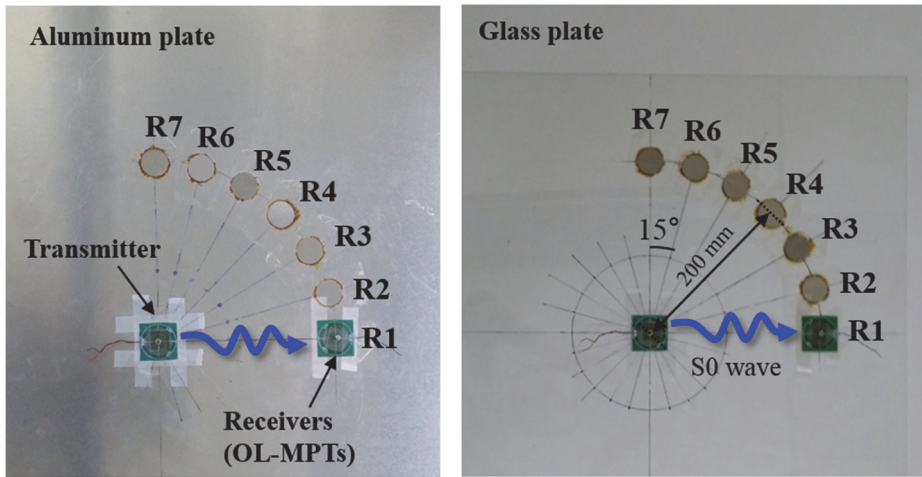
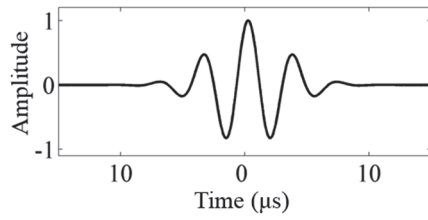
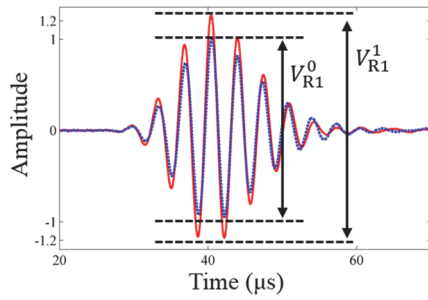


Figure A 11 Experimental setup to measure the elastic waves radiated on the aluminum and glass plates.

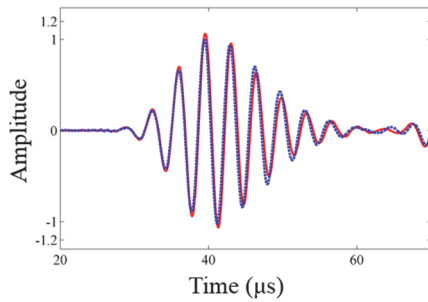


(a)



— : 1-slit patch  
 - - - : slitless patch

(b)



— : 1-slit patch  
 - - - : slitless patch

(c)

Figure A 12 (a) Input Gabor pulse signal centered at 270 kHz, (b) measured signals on an aluminum plate, and (c) measured signals on a glass plate.

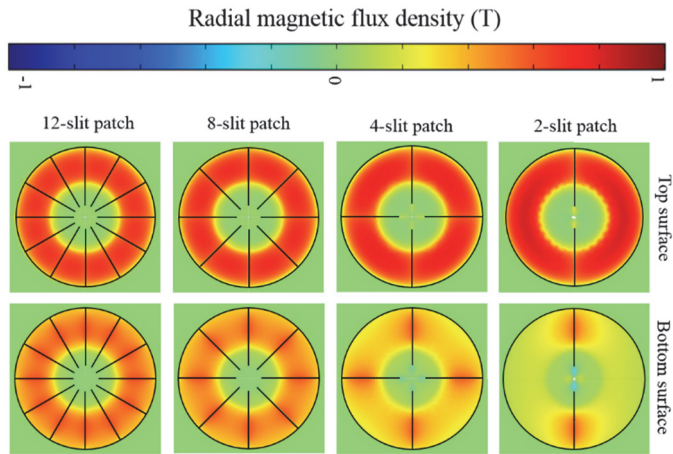


Figure A 13 Radial magnetic flux density plots of multiply slit patches.

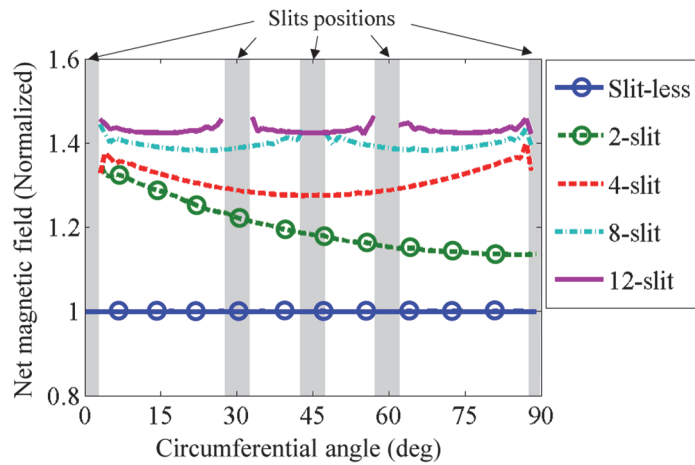


Figure A 14 The radial magnetic fields ( $H_r$ ) integrated along the  $z$ -direction on the mid-point of the coil (i.e., at  $r = (r_o + r_i)/2$ ) inside the magnetostrictive patch along the circumferential angle. The fields are normalized with respect to the field in the slit-less patch.

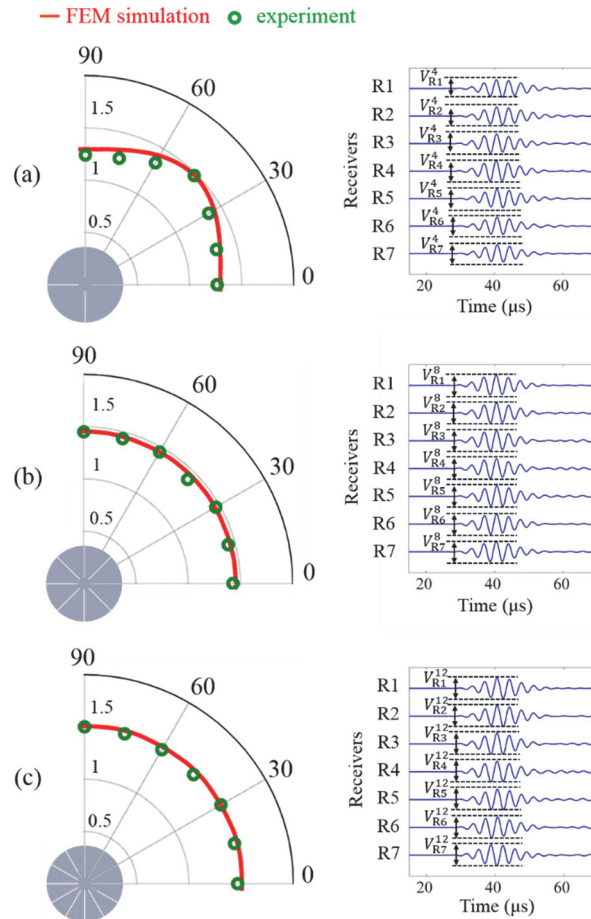


Figure A 15 Radiation patterns of the S0 mode and experimentally measured signals by the receivers (R1–R7). The results are for (a) 4-slit, (b) 8-slit and (c) 12-slit patches installed on an aluminum plate.

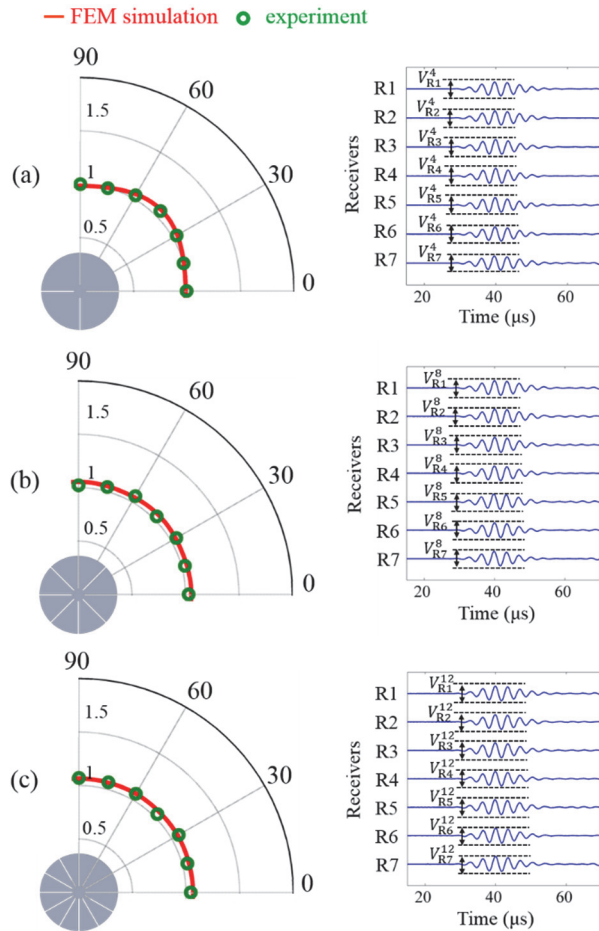


Figure A 16 Radiation patterns of the S0 mode and signals that were experimentally measured by the receivers (R1–R7). The results are for (a) 4-slit, (b) 8-slit and (c) 12-slit patches installed on a glass plate.

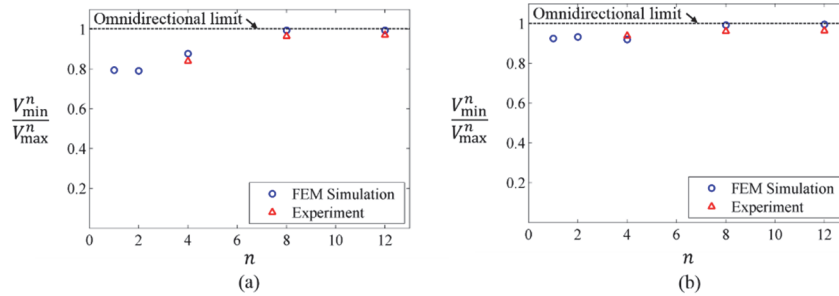


Figure A 17 Ratio of the minimum to maximum peak-to-peak values obtained from the radiation pattern signals (a) for on an aluminum plate and (b) for on a glass plate.

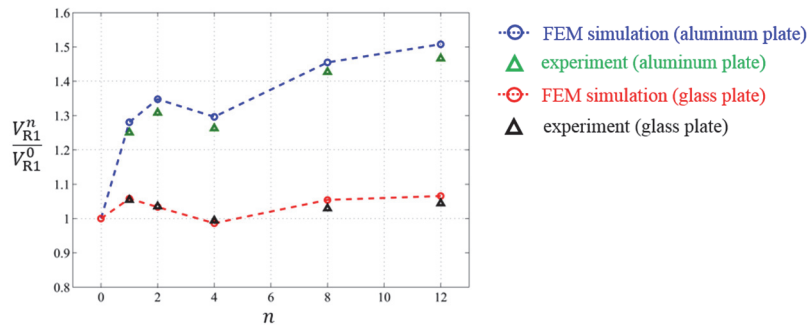


Figure A 18 Signal output increase ratio for a varying number of slits in the circular magnetostrictive patch of OL-MPT. ( $V_{R1}^n$  : peak-to-peak values of the signal measured by R1 for the  $n$ -slit patch-equipped MPT transmitter,  $V_{R1}^0$  : peak-to-peak value of the signal measured by R1 for the slit-less patch-equipped MPT transmitter.)

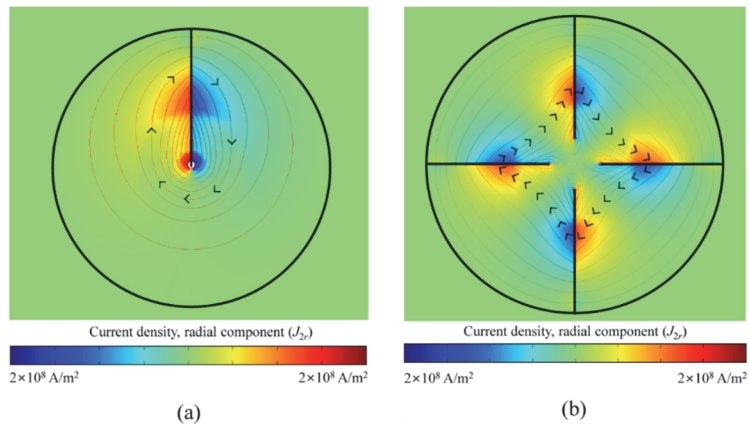


Figure A19 Contour plots of the radial component ( $J_{2r}$ ) of the current density on the bottom surface of (a) 1-slit patch and (b) 4-slit patch. The red line indicates the actual current circuit developed on the bottom surface.

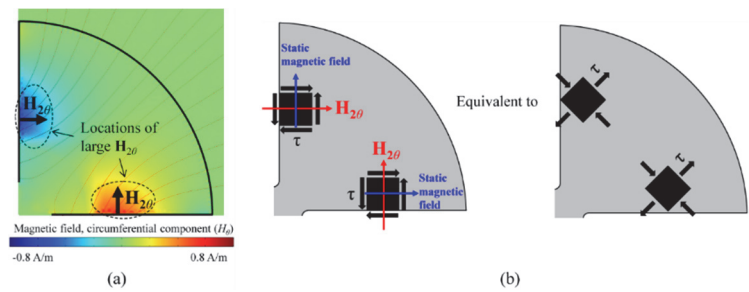


Figure A20 (a) Circumferential component of the magnetic field plot of the bottom surface of 4-slit patch ( $H_{2\theta}$ ), and (b) the shear strain due to the circumferential component of magnetic field ( $H_{2\theta}$ ). The equivalent normal stress state with respect to 45°-rotated directions is also shown.

## REFERENCES

- [1] Li J and Chan C 2004 Double-negative acoustic metamaterial *Physical Review E* **70** 055602
- [2] Oh J H, Kwon Y E, Lee H J and Kim Y Y 2016 Elastic metamaterials for independent realization of negativity in density and stiffness *Scientific reports* **6** 23630
- [3] Pendry J B 2000 Negative refraction makes a perfect lens *Physical review letters* **85** 3966
- [4] Shelby R, Smith D, Nemat-Nasser S and Schultz S 2001 Microwave transmission through a two-dimensional, isotropic, left-handed metamaterial *Applied Physics Letters* **78** 489-91
- [5] Smith D R, Pendry J B and Wiltshire M C 2004 Metamaterials and negative refractive index *Science* **305** 788-92
- [6] Smith D R, Schultz S, Markoš P and Soukoulis C 2002 Determination of effective permittivity and permeability of metamaterials from reflection and transmission coefficients *Physical Review B* **65** 195104
- [7] Bok E, Park J J, Choi H, Han C K, Wright O B and Lee S H 2018 Metasurface for Water-to-Air Sound Transmission *Physical review letters* **120** 044302
- [8] Xie Y, Konneker A, Popa B-I and Cummer S A 2013 Tapered labyrinthine

- acoustic metamaterials for broadband impedance matching *Applied Physics Letters* **103** 201906
- [9] Li Z, Yang D-Q, Liu S-L, Yu S-Y, Lu M-H, Zhu J, Zhang S-T, Zhu M-W, Guo X-S and Wu H-D 2017 Broadband gradient impedance matching using an acoustic metamaterial for ultrasonic transducers *Scientific reports* **7** 42863
- [10] Kildishev A V and Narimanov E E 2007 Impedance-matched hyperlens *Optics letters* **32** 3432-4
- [11] Choi M, Lee S H, Kim Y, Kang S B, Shin J, Kwak M H, Kang K-Y, Lee Y-H, Park N and Min B 2011 A terahertz metamaterial with unnaturally high refractive index *Nature* **470** 369
- [12] Bongard F, Lissek H and Mosig J R 2010 Acoustic transmission line metamaterial with negative/zero/positive refractive index *physical Review B* **82** 094306
- [13] Fleury R and Alù A 2013 Extraordinary sound transmission through density-near-zero ultranarrow channels *Physical review letters* **111** 055501
- [14] Moitra P, Yang Y, Anderson Z, Kravchenko I I, Briggs D P and Valentine J 2013 Realization of an all-dielectric zero-index optical metamaterial *Nature Photonics* **7** 791
- [15] Zhu R, Liu X, Hu G, Sun C and Huang G 2014 Negative refraction of elastic waves at the deep-subwavelength scale in a single-phase metamaterial

*Nature communications* **5** 5510

- [16] Lee H, Lee J K, Seung H M and Kim Y Y 2017 Mass-Stiffness substructuring of an elastic metasurface for full transmission beam steering *Journal of the Mechanics and Physics of Solids*
- [17] Kim Y Y and Kwon Y E 2015 Review of magnetostrictive patch transducers and applications in ultrasonic nondestructive testing of waveguides *Ultrasonics* **62** 3-19
- [18] Raghavan A 2007 Guided-wave structural health monitoring
- [19] Hirao M and Ogi H 1999 An SH-wave EMAT technique for gas pipeline inspection *NDT & E Int.* **32** 127-32
- [20] Pierce S, Culshaw B and Shan Q 1998 Laser generation of ultrasound using a modulated continuous wave laser diode *Applied physics letters* **72** 1030-2
- [21] Ham S, Song H, Oelze M L and Popovics J S 2017 A contactless ultrasonic surface wave approach to characterize distributed cracking damage in concrete *Ultrasonics* **75** 46-57
- [22] Lee J K, Kim H W and Kim Y Y 2013 Omnidirectional Lamb waves by axisymmetrically-configured magnetostrictive patch transducer *IEEE transactions on ultrasonics, ferroelectrics, and frequency control* **60** 1928-34
- [23] Seung H M, Kim H W and Kim Y Y 2013 Development of an omnidirectional shear-horizontal wave magnetostrictive patch transducer for

- plates *Ultrasonics* **53** 1304-8
- [24] Kim I K and Kim Y Y 2007 Shear horizontal wave transduction in plates by magnetostrictive gratings *Journal of mechanical science and technology* **21** 693-8
- [25] Lowe M J, Alleyne D N and Cawley P 1998 Defect detection in pipes using guided waves *Ultrasonics* **36** 147-54
- [26] Wang X, Peter W T, Mechefske C K and Hua M 2010 Experimental investigation of reflection in guided wave-based inspection for the characterization of pipeline defects *NDT & e International* **43** 365-74
- [27] Chaki S and Bourse G 2009 Guided ultrasonic waves for non-destructive monitoring of the stress levels in prestressed steel strands *Ultrasonics* **49** 162-71
- [28] Fokin V, Ambati M, Sun C and Zhang X 2007 Method for retrieving effective properties of locally resonant acoustic metamaterials *Physical review B* **76** 144302
- [29] Wu Y and Zhang Z-Q 2009 Dispersion relations and their symmetry properties of electromagnetic and elastic metamaterials in two dimensions *Physical Review B* **79** 195111
- [30] Torrent D and Sánchez-Dehesa J 2011 Multiple scattering formulation of two-dimensional acoustic and electromagnetic metamaterials *New Journal of Physics* **13** 093018

- [31] Chen X, Grzegorzczak T M, Wu B-I, Pacheco Jr J and Kong J A 2004 Robust method to retrieve the constitutive effective parameters of metamaterials *Physical Review E* **70** 016608
- [32] Park J H, Lee H J and Kim Y Y 2016 Characterization of anisotropic acoustic metamaterial slabs *Journal of Applied Physics* **119** 034901
- [33] Yeum C M, Sohn H and Ihn J B 2011 Lamb wave mode decomposition using concentric ring and circular piezoelectric transducers *Wave motion* **48** 358-70
- [34] Timoshenko S P and Woinowsky-Krieger S 1959 *Theory of plates and shells*: McGraw-hill)
- [35] Rayleigh J W S B 1896 *The theory of sound* vol 2: Macmillan)
- [36] Lamb H 1917 On waves in an elastic plate *Proceedings of the Royal Society of London. Series A* **93** 114-28
- [37] Achenbach J 2012 *Wave propagation in elastic solids* vol 16: Elsevier)
- [38] Graff K F 2012 *Wave motion in elastic solids*: Courier Corporation)
- [39] Pavlakovic B and Lowe M 2003 Disperse user manual: a system for generating dispersion curves *Copyright B Pavlakovic, M Lowe*
- [40] Bauchau O and Craig J 2009 *Structural analysis*: Springer) pp 173-221
- [41] Curie J and Curie P 1882 Phénomènes électriques des cristaux hémihédres à faces inclinées *Journal de Physique theorique et appliquee* **1** 245-51
- [42] Desilets C S, Fraser J D and Kino G S 1978 The design of efficient broad-

- band piezoelectric transducers *IEEE Transactions on sonics and ultrasonics* **25** 115-25
- [43] Safari A and Akdogan E K 2008 *Piezoelectric and acoustic materials for transducer applications*: Springer Science & Business Media)
- [44] Raghavan A and Cesnik C E 2005 Finite-dimensional piezoelectric transducer modeling for guided wave based structural health monitoring *Smart materials and structures* **14** 1448
- [45] Joule J P 1847 XVII. On the effects of magnetism upon the dimensions of iron and steel bars *Philosophical Magazine Series 3* **30** 76-87
- [46] Skórski R 1964 Matteucci effect: its interpretation and its use for the study of ferromagnetic matter *Journal of Applied Physics* **35** 1213-6
- [47] Broadwin A and Emery L M 1991 Magnetostrictive transducer. Google Patents)
- [48] Claeysen F, Lhermet N, Le Letty R and Bouchilloux P 1997 Actuators, transducers and motors based on giant magnetostrictive materials *Journal of alloys and compounds* **258** 61-73
- [49] Dhilsha K, Markandeyulu G, Rao B S and Rao K R 1997 Design and fabrication of a low frequency giant magnetostrictive transducer *Journal of Alloys and Compounds* **258** 53-5
- [50] Mayergoyz I D 1999 *Handbook of giant magnetostrictive materials*: Elsevier)

- [51] Lee J S, Kim Y Y and Cho S H 2008 Beam-focused shear-horizontal wave generation in a plate by a circular magnetostrictive patch transducer employing a planar solenoid array *Smart Materials and Structures* **18** 015009
- [52] Kim H J, Lee J S, Kim H W, Lee H S and Kim Y Y 2014 Numerical simulation of guided waves using equivalent source model of magnetostrictive patch transducers *Smart Materials and Structures* **24** 015006
- [53] Rose J L 2000 Ultrasonic waves in solid media. (ASA)
- [54] Tse F S, Morse I E and Hinkle R T 1963 *Mechanical vibrations* (Boston, MA: Allyn and Bacon)
- [55] Liu X-N, Hu G-K, Huang G-L and Sun C-T 2011 An elastic metamaterial with simultaneously negative mass density and bulk modulus *Appl. Phys. Lett.* **98** 251907
- [56] Oudich M, Djafari-Rouhani B, Pennec Y, Assouar M B and Bonello B 2014 Negative effective mass density of acoustic metamaterial plate decorated with low frequency resonant pillars *J. Appl. Phys.* **116** 184504
- [57] Liu Z, Zhang X, Mao Y, Zhu Y, Yang Z, Chan C T and Sheng P 2000 Locally resonant sonic materials *Science* **289** 1734-6
- [58] Yan X, Zhu R, Huang G and Yuan F-G 2013 Focusing guided waves using surface bonded elastic metamaterials *Appl. Phys. Lett.* **103** 121901

- [59] Vives A A 2008 *Piezoelectric transducers and applications*: Springer Science & Business Media)
- [60] Lee H, Oh J H, Seung H M, Cho S H and Kim Y Y 2016 Extreme stiffness hyperbolic elastic metamaterial for total transmission subwavelength imaging *Sci. Rep.* **6** 24026
- [61] Multiphysics C 2008 COMSOL Multiphysics Modeling Guide: Version 3.5. (Stockholm, Sweden: COMSOL AB)
- [62] Velichko A and Wilcox P D 2008 Guided wave arrays for high resolution inspection *J. Acoust. Soc. Am.* **123** 186-96
- [63] Kim H W, Cho S H and Kim Y Y 2011 Analysis of internal wave reflection within a magnetostrictive patch transducer for high-frequency guided torsional waves *Ultrasonics* **51** 647-52
- [64] Kim K, Lee H J, Lee J K and Kim Y Y 2016 Effects of slits in a patch of omnidirectional Lamb-wave MPT on the transducer output *Smart Mater. Struct.* **25** 035019
- [65] Seung H M and Kim Y Y 2016 Generation of omni-directional shear-horizontal waves in a ferromagnetic plate by a magnetostrictive patch transducer *NDT & E Int.* **80** 6-14
- [66] Sun K H, Cho S H and Kim Y Y 2008 Topology design optimization of a magnetostrictive patch for maximizing elastic wave transduction in waveguides *IEEE Trans. Magn.* **44** 2373-80

- [67] Yoo B, Na S-M, Flatau A B and Pines D J 2015 Magnetic shape anisotropy effect on sensing performance and directional sensitivity in magnetostrictive nickel patch transducer *J. Intell. Mater. Syst. Struct.* **27** 1075-91
- [68] Jiles D 1995 Theory of the magnetomechanical effect *Journal of physics D: applied physics* **28** 1537
- [69] Park C I, Cho S H and Kim Y Y 2006 Z-shaped magnetostrictive patch for efficient transduction of a torsional wave mode in a cylindrical waveguide *Appl. Phys. Lett.* **89** 174103
- [70] Cho S H, Lee J S and Kim Y Y 2006 Guided wave transduction experiment using a circular magnetostrictive patch and a figure-of-eight coil in nonferromagnetic plates *Applied physics letters* **88** 224101
- [71] Kim H W, Kwon Y E, Cho S H and Kim Y Y 2011 Shear-horizontal wave-based pipe damage inspection by arrays of segmented magnetostrictive patches *IEEE Trans. Ultrason., Ferroelect., Freq. Control* **58** 2689-98
- [72] The Journal of the Acoustical Society of America Assouar M B and Oudich M 2012 Enlargement of a locally resonant sonic band gap by using double-sides stubbed phononic plates *Appl. Phys. Lett.* **100** 123506
- [73] Oudich M, Li Y, Assouar B M and Hou Z 2010 A sonic band gap based on the locally resonant phononic plates with stubs *New J. Phys.* **12** 083049
- [74] Wu T-C, Wu T-T and Hsu J-C 2009 Waveguiding and frequency selection of Lamb waves in a plate with a periodic stubbed surface *Phys. Rev. B* **79**

104306

- [75] Oh J H, Sun K H and Kim Y Y 2013 Time-harmonic finite element analysis of guided waves generated by magnetostrictive patch transducers *Smart Materials and Structures* **22** 085007
- [76] Lowe M J S, Alleyne D N and Cawley P 1998 Defect detection in pipes using guided waves *Ultrasonics* **36** 147-54
- [77] Kim H W, Lee J K and Kim Y Y 2013 Circumferential phased array of shear-horizontal wave magnetostrictive patch transducers for pipe inspection *Ultrasonics* **53** 423-31
- [78] Wilcox P D 2003 Omni-directional guided wave transducer arrays for the rapid inspection of large areas of plate structures *Ultrasonics, Ferroelectrics, and Frequency Control, IEEE Transactions on* **50** 699-709
- [79] Wilcox P D, Lowe M J S and Cawley P 2005 The excitation and detection of Lamb waves with planar coil electromagnetic acoustic transducers *Ultrasonics, Ferroelectrics, and Frequency Control, IEEE Transactions on* **52** 2370-83
- [80] Lee J K, Kim H W and Kim Y Y 2013 Omnidirectional lamb waves by axisymmetrically-configured magnetostrictive patch transducer *Ultrasonics, Ferroelectrics, and Frequency Control, IEEE Transactions on* **60** 1928-34
- [81] Giurgiutiu V and Bao J 2004 Embedded-ultrasonics structural radar for in situ structural health monitoring of thin-wall structures *Structural Health*

*Monitoring* **3** 121-40

- [82] Wilcox P, Lowe M and Cawley P 2005 Omnidirectional guided wave inspection of large metallic plate structures using an EMAT array *Ultrasonics, Ferroelectrics, and Frequency Control, IEEE Transactions on* **52** 653-65
- [83] Yu L and Giurgiutiu V 2008 In situ 2-D piezoelectric wafer active sensors arrays for guided wave damage detection *Ultrasonics* **48** 117-34
- [84] Vishnuvardhan J, Muralidharan A, Krishnamurthy C V and Balasubramaniam K 2009 Structural health monitoring of anisotropic plates using ultrasonic guided wave STMR array patches *NDT & E International* **42** 193-8
- [85] Lee J K, Kwon Y E, Lee H S, Seung H M, Kim K, Lee J K, Kim H W, Lee H C and Kim Y Y 2014 Development and Application of Phased Array System for Defect Imaging in Plate-like Structures *Transactions of the Korean Society for Noise and Vibration Engineering* **24** 123-30
- [86] Kwun H and Bartels K 1998 Magnetostrictive sensor technology and its applications *Ultrasonics* **36** 171-8
- [87] Ogi H 1997 Field dependence of coupling efficiency between electromagnetic field and ultrasonic bulk waves *Journal of Applied Physics* **82** 3940-9
- [88] Hirao M and Ogi H 2013 *EMATs for science and industry: noncontacting*

- ultrasonic measurements*: Springer Science & Business Media)
- [89] Duenas T and Carman G 2000 Large magnetostrictive response of Terfenol-D resin composites *Journal of Applied Physics* **87** 4696-701
- [90] Mayergoyz I D and Engdahl G 1999 *Handbook of giant magnetostrictive materials*: Elsevier)
- [91] Benatar J G 2005 FEM implementations of magnetostrictive-based applications. University of Maryland)
- [92] Yoo B, Na S-M, Flatau A B and Pines D J 2015 Magnetic shape anisotropy effect on sensing performance and directional sensitivity in magnetostrictive nickel patch transducer *Journal of Intelligent Material Systems and Structures*
- [93] Multiphysics C 2008 COMSOL Multiphysics Modeling Guide: Version 3.5 *COMSOL AB, Stockholm, Sweden*
- [94] Suzuki T, Baba H and Matsumoto E 2003 Stress effect on hysteretic magnetization curve of nickel. In: *Proceedings of the Tenth International Symposium on Applied Electromagnetic and Mechanics*: IOS Press) pp 307-10
- [95] Mallat S 1999 *A wavelet tour of signal processing*: Academic press)

## ABSTRACT (KOREAN)

# 공진기 쌍을 이용한 극저 임피던스 유효 매질 구현 및 탄성과 출력 향상

김 기 연

서울대학교 대학원

기계항공공학부

본 연구는 수동적이고 비파괴적으로 탄성과 출력을 향상시키는 방법을 개발하고, 새로운 유효 매질 모델을 세움으로써 출력 향상의 물리적 근거를 밝혀내는 데 공헌한다. 기존에도 탄성과 트랜스듀서의 출력을 높이기 위해 많은 개선이 이루어져 왔으나, 탄성파가 전달 되는 매질에 대한 학술적 접근은 고려된 바 없다. 파괴적이지 않은 방법으로 해당 매질에 대한 조절을 하기 위해서는 특정 구조물을 부착하여야 하며, 이 경우 매질의 임피던스를 높이게 되고 트랜스듀서 출력 향상에 도움이 되지 못한다. 그러므로, 비파괴적인 동시에 임피던스를 낮출 수 있는 기술이 필요하다.

이와 같은 목적을 이루기 위하여 본 연구에서는 해당 매질 위에 한 쌍의 공진기를 부착한다. 이러한 공진기 쌍은 주기적으로 배열되어 있지 않기 때문에, 기존의 유효 매질 모델로는 해석하지 못하며 시스템의 유효 물성치를 계산할 수 있는 새로운 해석 방법이 필요하다. 뿐만 아니라, 트랜스듀서의 작동 주파수에서, 공진기 간의 거리는 파장에 비해서 짧지 않으므로 기존의 유효 매질 이론을 직접적으로 적용하기 어렵다. 본 연구에서는 이러한 특수한 공진기의 배열에 대해 유효 물성치를 해석할 수 있는 새로운 방법을 구상한다.

새롭게 구상된 해석 방법을 통하여 유효 물성치를 가지는 동등한 시스템을 구성하여 기존 시스템을 해석한다. 공진기 쌍으로 둘러싸인 부분의 유효 임피던스는 이전보다 매우 낮음을 확인한다. 극저 임피던스 구역에 탄성과 트랜스듀서를 설치함으로써 기존 트랜스듀서의 출력을 향상시킬 수 있다. 한편, 임피던스의 대비가 매우 높은 경우 트랜스듀서로부터 생성된 탄성파가 외부로 쉽게 투과되지 못하는 문제가 생긴다. 본 연구에서는 극저 임피던스 구역으로부터의 향상된 탄성파 출력을 외부로 완벽히 투과시킬 수 있는 조건을 설명한다. 이론에 대한

예시으로써, 평판에서  $S_0$ ,  $SH_0$  그리고  $A_0$  모드에 대한 출력 향상을 제시한다.

본 연구에서는 이론적 모델, 유한요소해석을 이용한 수치적 해석과 실험을 통하여 극저 임피던스와 탄성과 출력 향상에 대해 조사한다.

**주요어:** 탄성 메타물질, 저감 임피던스, 출력 향상, 트랜스듀서, 유효 매질 모델

**학 번:** 2012-20647